# Improving the Three Dimensional, Structural Velocity Field Reconstruction Process with Computer Vision

by

**David H. Coe,**

Dissertation submitted to the Faculty of the
Virginia Polytechnic Institute and State University
in partial fulfillment of the requirements for the degree of

**Doctor of Philosophy**

in

**Mechanical Engineering**

Dr. L. Abbott
Dr. D. Farkas
Dr. L.D. Mitchell
Dr. C.R. Reinholtz
Dr. R.L.West, Chair

September 1998

Blacksburg, Virginia

Dedicated to my parents:

Frank and Wilma

# Acknowledgments

I would like to express my heartfelt thanks and gratitude to Dr. Robert L. West for being my advisor during my doctoral studies. I would also like to thank my committee members, Dr. Charles Reinholtz, Dr. Dan Farkas, Dr. Lynn Abbott, and Dr. Larry Mitchell, for their inspiration, insights, and help over the years.

I would also like to thank Charles Coe, President, Maxwell Bailer Corp., Zonic Corp., Sandia National Laboratory, and the mechanical engineering department for financial support.

Thanks to the graduate students whom I have known: Jon Blotter, Chris Doktor, Jose' Dominguez, Barry Fallon, William Li, Wenhsyong Lin, Brian Lindholm, David Montgomery, Francisco Rivera, Mike Stafne, and Xiandi Zeng.

Thanks to my wife, Dawn, and my daughters, Heather, Autumn, Rosemary, Sarah, and Freyja.

David H. Coe

*Virginia Polytechnic Institute and State University*
*September 1998*

# Improving the Three Dimensional, Structural Velocity Field Reconstruction Process with Computer Vision

David H. Coe, Ph.D.
Virginia Polytechnic Institute and State University, 1998
Supervisor: Robert L. West

## Abstract

This research presents improvements to the velocity field reconstruction process achieved through computer vision. The first improvement of the velocity reconstruction process is the *automation* of the scanning laser Doppler vibrometer (SLDV) pose procedure. This automated process results in superior estimates of the position and orientation of the SLDV. The second improvement is the refinement of the formulation for reconstruction of the velocity field. The refined formulation permits faster computation, evaluation, and interpretation of the reconstructed structural velocity field. Taken together, these new procedures significantly improve the overall velocity reconstruction process which results in better, unbiased out-of-plane velocity estimates in the presence of noise.

The automation of the SLDV pose procedure is achieved through a computer vision model of the SLDV. The SLDV is modeled as a projective camera, i.e. an imager which preserves projectivities. This projective camera model permits the precise association of object features with image features. Specifically, circular features in the object space are seen by the SLDV as ellipses in the image space. In order to extract object points, the bitangents among the circular features are constructed and the bitangent points selected. The accuracy and precision of the object points are improved through the use of a calibrated object whose circular features are measured with a coordinate measuring machine. The corresponding image points are determined by constructing the bitangents among the ellipses and selecting the tangent points. Taken together, these object/image bitangent point sets are a significantly improved data set for previously developed SLDV pose algorithms. Experimental verification of this automated pose procedure includes demonstrated repeatability, independent validation of the estimated pose parameters, and comparison of the estimated poses with previous methods.

The refinement of the velocity reconstruction formulation is a direct result of the computer vision viewpoint adapted for this research. By viewing the velocity data as *images* of the harmonically excited structure's velocity field, analytical techniques developed for holographic interferometry are extended and applied to SLDV velocity images. Specifically, the ”absolute” and ”relative” fringe-order methods are used to reconstruct the velocity field with the ”best” set of bases. Full and partial least squares solutions with experimental velocity data are calculated. Statistical confidence bounds of the regressed velocity coefficients are analyzed and interpreted to reveal accurate out-of-plane, but poor in-plane velocity estimates. Additionally, the reconstruction process is extended to recover the velocity field of a family of surfaces in the neighborhood of the ”real” surface. This refinement relaxes the need for the exact experimental geometry. Finally, the velocity reconstruction procedure is reformulated so that independent least squares solutions are obtained for the two in-plane directions and the out-of plane direction. This formulation divides the original least squares problem into three smaller problems which can be analyzed and interpreted separately. These refinements to the velocity reconstruction process significantly improve the out-of-plane velocity solution and interpretation of the regressed velocity parameters.

# Contents

# Chapter 1

# Introduction

The development of new instruments to observe material phenomena requires the user of the instrument to reflect upon the instrument's observations: to think about the data acquired and determine the extent to which this data represents reality. This research employs a scanning laser Doppler vibrometer (SLDV) to observe harmonically excited structures and to acquire velocity images of that vibrating structure. These velocity images are fused together to recover the velocity response field of the structure. This dissertation reflects the research which improves this velocity reconstruction process with computer vision.

Mechanical engineers design, analyze, fabricate, and test machines that transform energy. This intention of transforming energy guides the mechanical engineer in his efforts to fashion idealized, geometric forms which embody these ideas; engineering analysis predicts how this ideal form will perform under specific conditions; fabrication realizes the form in a given medium; and testing measures the response of the actual form to specified conditions. If the experimental testing fails to reject the design and analysis, then the product design cycle is complete. The experimental testing does not prove that the analytic model is correct, only that no evidence is present to reject the model's hypothesis. If the experimental testing rejects the hypothesis that the design and analysis are correct, then at least one modeling assumption is incorrect and must be revised. This successful experimental validation process is crucial to the development of practical machines.

Mechanical behavior theories, e.g., thin-shell theories, are hypothetical statements which permit the formulation of analytic models and validating experiments. For structural dynamics, the structural velocity field is one of the fundamental quantities to verify through experiment. Typical experiments employ simple geometries like beams and plates so that the proposed theory is validated. Still, there is a need to experimentally determine the true velocity response field of structures undergoing dynamic testing independent of the analytical model. This research addresses this need and improves the velocity field reconstructon process by an innovative use of structural velocity images and computer vision techniques, without reference to a particular constitutive or kinematic model of the structure.

## 1.1 Background and Motivation

This research is motivated by the continuing need to experimentally validate the dynamic mechanical behavior of structures. The basic viewpoint adapted in this research is expressed by Jaunzemis [29, p.131]

> In the spatial description of particle velocities, $V = f(X, t)$, is considered as a primitive field and not as obtained by differentiating with respect to time some position vector.

This viewpoint emphasizes the *fundamental* nature of accurately recovering the structural velocity field. Experimental validation techniques of dynamic behavior range from point, mass loaded measurements, e.g. strain gages and accelerometers, to full field, non-contacting procedures, e.g., holographic interferometry. This research refines a non-contacting technique developed for SLDV velocity images[40].

The dynamic response field of structures is an important quantity to measure because the dynamic strains and stresses can cause fatigue failures [52], especially if the excitation frequency is at or near one of the structure's resonant frequencies. Experimental measurements of dynamic strains are also invaluable to the validation of finite element predictions. These measurements also help define a performance envelope for the structure. These dynamic strains are straightforward calculations [50, 51] once the strucure's velocity field is known. Thus this dissertation focuses upon the refinement of the velocity reconstruction process to achieve the best structural velocity field for post-processing.

The goal of this research is to improve the velocity field reconstruction methodology for structures undergoing dynamic testing. Koenderink [31, p.14] notes, "objects can be said to induce a 'geometric field' around them, a field that can be probed operationally.

The structure of the field is the shape of the object.” Similarly, a vibrating structure induces a velocity field on this geometric domain which can be probed by a SLDV. Recent developments in laser vibration measurement technology have provided instruments like the SLDV which can measure the line-of-sight surface velocities with high spatial density. These instruments can be used to acquire velocity images of a vibrating structure. Each ”pixel” in the velocity images may be interpreted as an independent, line-of-sight measurement of the velocity field. Yet interpreted as an image the dataset contains magnitude, direction and gradient information of the velocity field from a unique domain - the structure’s surface. This reseach investigates the advantages of applying computer vision techniques to velocity images to improve the overall velocity reconstruction procedure.

## 1.2 Problem Statement

The problem addressed in this research is the need for a velocity reconstruction methodology which reproduces experimental velocity fields which are ”sufficiently close” for engineering analysis but are determined independently of this analysis. The typical experimental set-up is shown in Figure 1.1. The current velocity reconstruction process has several drawbacks: the registration procedure requires the technician to align, ”eyeball”, the laser beam with specific fiducial marks on the structure; the structural geometry and fiducial marks are not known with great accuracy or precision; and the structure’s surface geometry must be known a priori. These issues are addressed by the research objective and hypothesis.

## 1.3 Research Objective and Hypothesis

The objective of the research is the enhancement of the current velocity field reconstruction process. This process consists of four steps: determine the pose of the SLDV; acquire velocity images of the harmonically excited structure; repeat steps one and two from multiple viewpoints; and, finally, fuse the velocity images and geometry information to reconstruct the structure’s velocity field. This research is limited to improving each step so that the overall velocity reconstruction process yields an improved estimate of the structure’s velocity field (or dynamic response field). This may be restated as a research hypothesis.

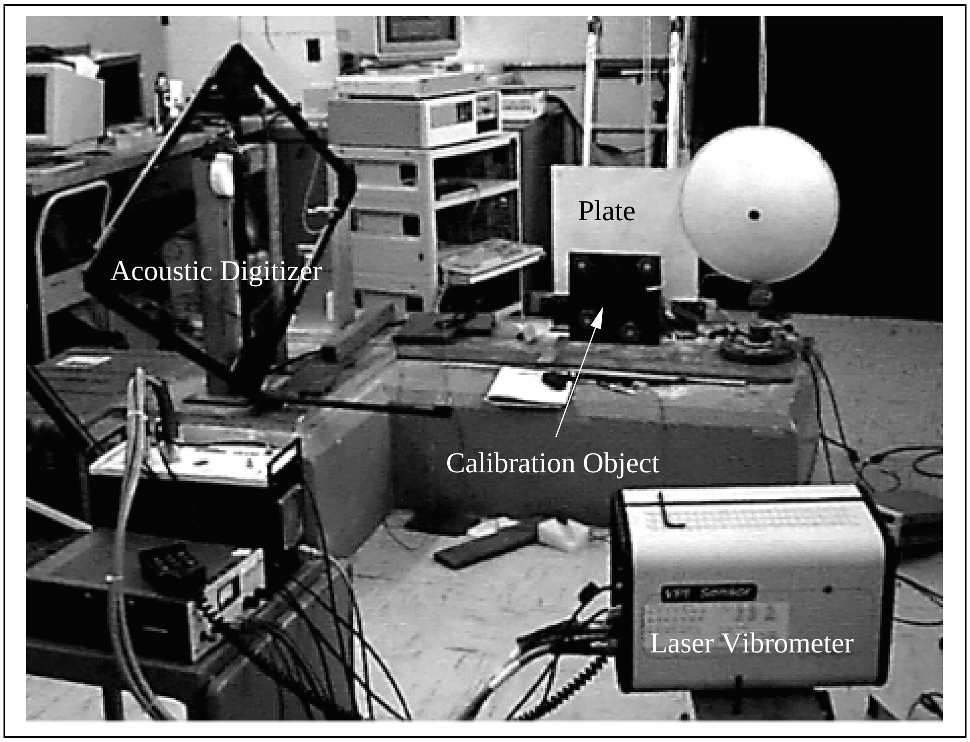

**Figure 1.1: The Experimental Set-Up**

**Hypothesis** The three dimensional structural velocity field reconstruction process may be significantly improved by applying computer vision techniques to velocity images acquired with a scanning laser Doppler vibrometer (SLDV).

## 1.4 Research Contributions

Improving the velocity reconstruction process with computer vision guides each step of the conducted research. By viewing the velocity images as true computer vision *images*, the velocity reconstruction process may be modified and enhanced to achieve the following research contributions:

- A computer vision model for the SLDV
- A pose calibration object for the SLDV
- An automated SLDV pose algorithm
- A velocity reconstruction procedure without surface geometry
- An orthogonally decomposed velocity reconstruction procedure

## 1.5 Research Scope

The scope of this research is guided by the velocity reconstruction process and bounded by the impact of velocity *images* upon this process. Each step in the velocity reconstruction process is examined from a computer vision point of view to see if treating the SLDV velocity data as an image can improve that step. Two steps are candidates for this research - pose automation and fusion of multiple velocity images. The extent to which these steps can be improved through computer vision is the scope of this research.

## 1.6 Dissertation Overview

This dissertation describes the development and validation of each research contribution. The context for the research is prepared with a literature review of related work in Chapter 2. With this background, the basic acquisition of a velocity image with a SLDV is described. Next the SLDV pose automation procedure is presented and experimentally validated in Chapter 4; this chapter begins with a computer vision model for the SLDV, describes the pose calibration object, develops the related pose automation algorithm, and provides the experimental results. Once the best SLDV poses are available, the improved velocity reconstruction process is described in Chapter 5; this chapter outlines the current velocity reconstruction procedure, presents the modified procedure and evaluates the results of the modified procedure. The final chapter summarizes the research results and makes recommendations for future research.

# Chapter 2

# Literature Review

Fundamentally this research is based upon the ability to determine image points, which have associated velocity measurements, of specified object points. This capability requires knowledge of the SLDV's pose combined with multiple velocity *images*. The SLDV velocity data is interpreted as an image where there is a local one-to-one and onto map with the structure's surface. This computer vision viewpoint is essential to the reconstruction of the velocity field as specified object points may be uniquely associated with the velocity image points from velocity data acquired from multiple viewpoints. The following sections review research which investigates the general pose problem and reconstruction of vector fields from multiple viewpoint, registered sensor data.

## 2.1 Sensor Pose

The basic approach of calculating the pose of a sensor is to develop a model of the sensor which relates image points with tranformed object points (translated and rotated). The initial sensor model relates image points with object points whose coordinates are defined in the sensor's coordinate system. If the object points' coordinates are known in another coordinate system and the image coordinates are measured with the sensor, then some rigid body transformation of these object points exists which will be consistent with the sensor model and the transformed object points,

$$\mathbf{P}_{image} = F_{sensor}(\mathbf{P}_{wcs} T^{scs}_{wcs}). \tag{2.1}$$

Here the image point is $\mathbf{P}_{image}$, $T_{wcs}^{scs}$ is the rigid body transformation from a world coordinate system (wcs) to the sensor coordinate system (scs), $\mathbf{P}_{wcs}$ is the object point in the world coordinate system, and $F_{sensor}()$ is the sensor model. This is known as the pose or registration problem and has been extensively researched in photogrammetry, computer vision, robotics, and specifically, the SLDV.

Photogrammetry, computer vision, robotics, and the SLDV have data post-processing requirements which need the pose, extrinsic, parameters for their respective sensors. The six extrinsic parameters are three orientation angles and three translation distances. These parameters may be combined to form a 4x4 transformation matrix which relates the world coordinate system to the sensor coordinate system. Penna [45] presents an introductory view of basic pose and photogrammetric procedures. Salma [53] and Ghosh [19] provide excellent developments of in-depth analytic procedures for camera pose estimation. Faugeras [16] emphasizes the computer vision viewpoint of these procedures, including an excellent section on linear versus non-linear solutions to the sensor pose problem. An example of remote sensing registration with a multi-resolution approach is provided by Djamdji [9]. A registration procedure without explicit point correspondences was developed by Fua and Leclerc [18]. Pose estimation techniques from corresponding object/image points have been developed by Haralick [25, 26]. Pennec and Thirion's registration and validation procedure [46] emphasizes a composition noise model rather than an additive noise model, an important consideration since the six pose parameters are not independent. The field of robotics also employs sensors, e.g. CCD cameras, to assist in accurate positioning of the generic robot arms. Chou and Kamel [7] use quaternions to find the position and orientation of a camera mounted on a robot arm. Fallon [15] demonstrated the use of computer vision techniques to automatically determine the pose of a robot end-effector. If the SLDV is viewed within a robotic framework [12], then the scanning laser may be viewed as the sensor which provides information for the pose determination process. For the SLDV pose, this means developing an algorithm which determines the pose from known object points, $\mathbf{P}_{wcs}$, and image points, mirror angles (voltages). Zeng [61], Lindholm [33], and Montgomery [39] each developed and implemented pose algorithms for the SLDV. These references are a representative subset of the available literature on pose estimation, a problem crucial to accurate and meaningful post-processing of the acquired data. All these methods are dependent on accurate, precise coordinates for the *object* and *image* points.

The research in this dissertation does not develop a new pose alogrithm, but improves the accuracy and precision of the input data set of corresponding points which improves the SLDV pose estimates. This developed procedure is based upon projective invariants.

## 2.2 Projective Invariants

The use of projective invariants eliminates the need for the rigid body transformation matrix when relating object points in the world coordinate system to the sensor image points. In one mathematical form, the cross-ratios of the object points are equal to the cross-ratios of the image points,

$$cr(\mathbf{P}_{WCS}) = cr(\mathbf{P}_{image}). \tag{2.2}$$

Bypassing the transformation permits the researcher to develop features which are projectively invariant so that correspondences between the object points and the image points are direct. In other words, the object and image points are determined independently of the pose transformation matrix. Once found, these object and image points may be used with previously developed algorithms, above, to determine the pose transformation matrix. Developing "new" invariants is unnecessary. Mundy [42] notes,

> Numerous methods for constructing invariants have been developed, particularly in the nineteeth century. These methods apply to transformations which can be represented as a group. Two different approaches have emerged: one is concerned with algebraic invariants and called the symbolic method: the second method is derived from Lie group theory and based on the observation that invariants are constant on group orbits.
>
> Because of the extensive literature on group invariants it is not always necessary to discover new invariants for vision applications. A large number of useful invariants can be simply looked up. For example, Weyl [60] provides complete tables of invariants for systems of vectors under the action of the rotation group, the affine group, and the general linear (projective) group.

The use of conics as projectively invariant features to recover pose and relative motion was reported by Rothwell et.al [48]. Specifically the invariance of the bitangent points between two conics was exploited to recover the pose. Fallon[15] used the same projectively invariant features to recover the image points of the circle centers and determine the pose of the robot arm. Using point features to determine pose has been investigated by Boufama [6]. Gros [24] looks at using the cross-ratios to compute projective invariants from two images. In short, the research applying projective invariants is extensive in the computer vision domain where CCD imagers abound, but has not been extended to the SLDV. The research in this dissertation expands the projective invariant application domain to include the scanning laser Doppler vibrometer.

## 2.3 Field Reconstruction with Lasers

Field reconstruction with lasers may be divided into two research areas, holographic interferometry and laser based velocity measurements. The basic phenomenon exploited by laser holgraphy is the fringes which result from the phase interference between the reference hologram and the hologram of the deformed surface. The theoretical accuracy of this type of measurement is $\pm\frac{1}{2}\lambda$, where $\lambda$ is the wavelength of the laser. The hologram's fringes can be interpolated to improve the accuracy. In constrast the phenomena measured by the SLDV is the beat frequency which results from the mixing of the reference laser beam and the interrogating laser beam. The interrogating laser beam is shifted in frequency by the moving surface, i.e. the Doppler effect. The measurement accuracy is determined by the processing electronics. For the Ometron system used in this research, the overall accuracy is ±0.5% of full scale[43]. The following sections highlight the essential aspects of holographic interferometry and previous SLDV velocity reconstruction research to provide the groundwork for the research in this dissertation.

### 2.3.1 Displacements from Holographic Interferometry

Holographic interferometry is an experimental technique which infers displacements from interferometric fringes. The development of holographic interferometry closely followed the need to experimentally verify analytic models, e.g. finite element models. A doubly exposed holograph is obtained from an object before and after applying a test load. A holographic interferogram results whose fringes represent the change in path length between the laser source and image. This path length difference may be described by

$$\delta = (\vec{K} \bullet \vec{L}), \tag{2.3}$$

where $\delta$ is the path length difference;$\vec{K}$ is the sensitivity vector; and $\vec{L}$ is the displacement vector. By combining multiple holograms, the displacements can be reconstructed without knowledge of the actual surface. The displacement may be recovered at a point with straightforward linear algebra.

$$\begin{aligned} \begin{Bmatrix} \delta_1 \\ \delta_2 \\ \delta_3 \end{Bmatrix} &= \begin{bmatrix} k_{11} & k_{12} & k_{13} \\ k_{21} & k_{22} & k_{23} \\ k_{31} & k_{32} & k_{33} \end{bmatrix} \begin{Bmatrix} L_x \\ L_y \\ L_z \end{Bmatrix} && (2.4) \\ \delta &= \mathbf{KL} && (2.5) \\ \mathbf{L} &= \mathbf{K}^{-1}\delta && (2.6) \end{aligned}$$

This procedure is known as the absolute fringe method [50, 58, 32]. If at least four holograms are available, then the relative fringe method [50, 58, 32] may be used to determine the displacement vector. The path length difference is now

$$\delta_i - \delta_j = (\vec{k}_i - \vec{k}_j) \bullet \vec{L}. \qquad (2.7)$$

The process of solving for the displacement vector remains the same, but with different bases. The two methods are complementary as the basis vectors emphasize different displacement directions, out-of-plane (absolute) and in-plane (relative). These two fringe counting methods may be used to reconstruct the displacement field without the actual surface information since the interference pattern is the difference between the original surface and the displaced surface. Figure 2.1 depicts the differing observation directions which are the senesitivity vectors ($k_i$), the laser source ($\mathbf{h}$), and the differing base vectors ($\mathbf{g}_i$) for the absolute and relative fringe methods. The accuracy of three-dimensional displacements in holographic interferometry has been investigated by Matsumoto et.al. [36], Vest[58], and Kreis[32]. Each reseacher noted the importance of the condition number of $\mathbf{K}$ in accurately determining the displacements. Kreis[32, p.185] suggests that a Hadamard condition number >0.1 is desirable for accurate displacement reconstruction. (The Hadamard condition number is similar to Matlab's rcond command, the condition number of the matrix inverse. Here a condition number of 1 is ideal, while condition numbers near zero are ill-conditioned.)

The current SLDV velocity reconstruction procedure cannot utilize the relative fringe method because two velocity samples "never" originate from the same surface point. The research conducted in this dissertation overcomes this limitation by adopting a computer

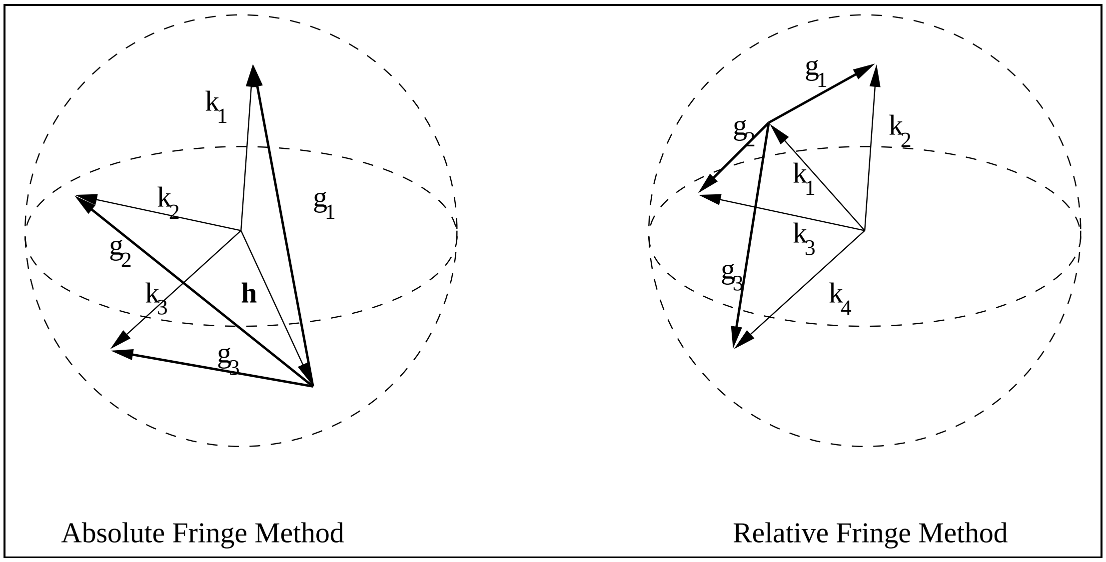

**Figure 2.1: Sensitivity Vectors**

vision model for the SLDV. The field reconstruction technique has been extended to reconstruction of velocity fields.

### 2.3.2 Velocity Fields

The reconstruction of a structure's velocity field has been accomplished with both time-averaged holograms and SLDV velocity images. Tonin and Bies [57, 56] developed the general theory and procedure for determining the velocity field from time-averaged holograms. First the structure is excited with a harmonic force; consequently, the structure's response is also harmonic with the same frequency [37]. For linear structures with this type of motion, a structure's surface point may be described by

$$\mathbf{V}(\xi,t) = c(\xi,t)(e)_1 + b(\xi,t)(e)_2 + a(\xi,t)(e)_3, \tag{2.8}$$

where $\xi$ is the arc length parameter along a surface contour, and

$$\begin{aligned} c(\xi,t) &= c(\xi)\cos(\omega t+\gamma), & (2.9)\\ b(\xi,t) &= b(\xi)\cos(\omega t+\beta), & (2.10)\\ a(\xi,t) &= a(\xi)\cos(\omega t+\alpha), & (2.11) \end{aligned}$$

are the orthogonal, harmonic motions of the point at a single frequency. The corresponding amplitudes are approximated by a finite sequence of spatial, trigonometric functions. By combining these assumed motions with the characteristic function for time-averaged holography, a least squares solution is possible to recover the structure's three dimensional vibration. The surface geometry must be known or assumed to employ this technique. Similarly, Montgomery [40] and Dominquez[12] developed velocity field reconstruction procedures for SLDV velocity images. Like time-averaged holography, a surface geometry is assumed. In Montgomery's process, finite element basis functions on the discretized surface are used to approximate the velocity field. By projecting the SLDV velocity data onto the discretized surface, a least square's solution[11] for the velocity field is obtained for that surface. In contrast to this process Dominquez fitted the SLDV velocity data and reconstructed the 3-D velocity point by point in a manner similar to the displacement reconstruction above. The research in this dissertation extends and synthesizes these approaches by solving the velocity field for a family of surfaces using least squares and a combined relative and absolute fringe method.

# Chapter 3

# Velocity Images

This research investigates the processing and manipulation of velocity images in the reconstruction of the experimental velocity field of harmonically excited structures. This chapter presents the general procedure for acquiring a single velocity image using Ometron's scanning laser Doppler vibrometer. The acquisition of a velocity image with Ometron's SLDV is a process consisting of structure excitation, region of interest (ROI) definition, time series data acquisition, and velocity image formation. The following sections describe each step of this process.

## 3.1 Operation of Ometron's SLDV

The Ometron SLDV is the instrument used in this research to acquire velocity images. The Ometron SLDV [43] is a Michelson interferometer which measures the line-of-sight velocity component of a moving surface. Drain [13] investigates this laser Doppler phenomenon in detail, but the essential relationship is $v_{meas} = \vec{V} \bullet \vec{D}$; $\vec{V}$ is the velocity where the laser beam illuminates the structure; the vector $\vec{D}$ is the direction cosines of the laser beam from the structure to the SLDV; and $v_{meas}$ is the measured velocity. Scanning is accomplished by two mirrors with offset, orthogonal axes, see Figure 3.1. Ometrons's SLDV images a vibrating surface by deflecting the mirrors and sampling the structure's velocity field point by point. The SLDV produces a voltage linearly proportional to the velocity which may be sampled with an analog to digital converter and processed. The conversion from voltage to velocity is simply $100\frac{mV}{mms^{-1}}$[43] for Ometron's SLDV medium range setting (all data in this research was acquired in this mode). Figure 3.2 shows a typical data acquisition hardware

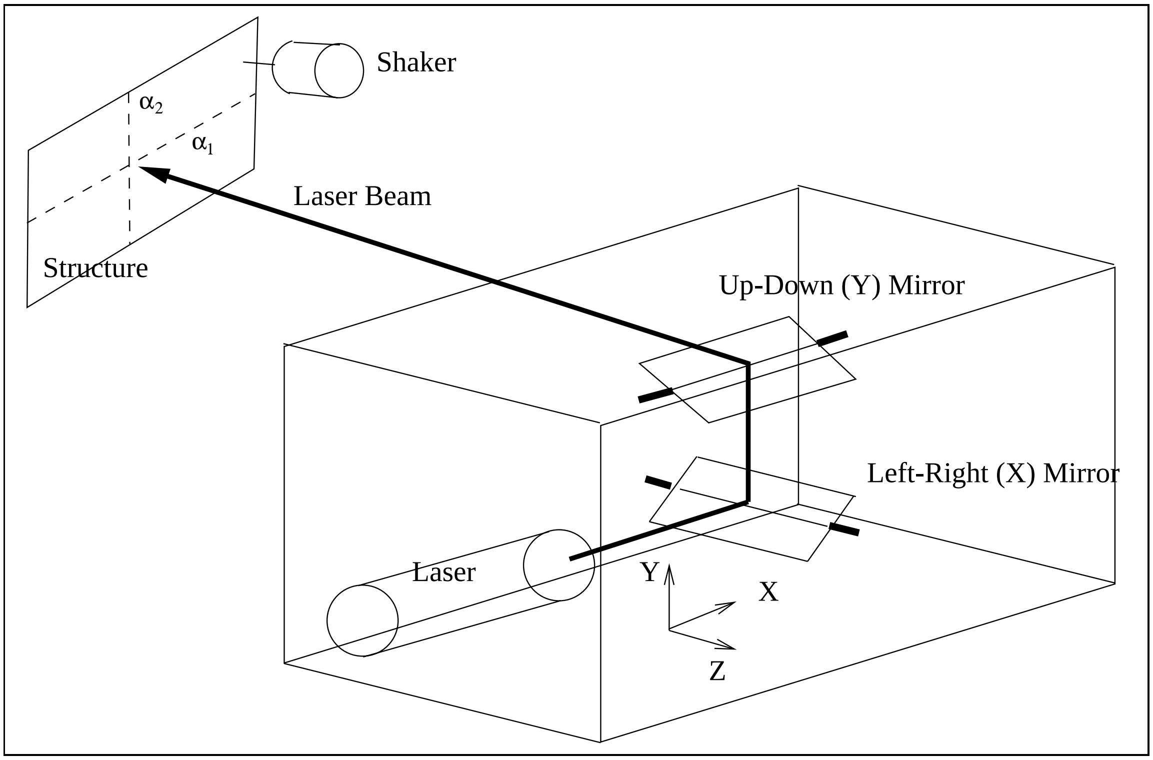

**Figure 3.1: Ometron's SLDV**

schematic. The first step is structure excitation.

## 3.2 Structure Excitation

The structural velocity field is achieved through harmonic excitation of the structure. The structure is set into motion with a shaker which is driven by an amplified sinusoidal signal from a function generator. Figure 3.2 depicts the arrangement of the experimental test equipment. Assuming the structure is linear, the structure is excited with a harmonic force and responds with a harmonic velocity field [38]

$$\vec{V}(\alpha_1, \alpha_2) = A\cos(\omega t + \phi_1)\hat{\imath} + B\cos(\omega t + \phi_2)\hat{\jmath} + C\cos(\omega t + \phi_3)\hat{k}, \tag{3.1}$$

where $\vec{V}(\alpha_1, \alpha_2)$ is the velocity at surface coordinates $\alpha_1, \alpha_2$; $\omega$ is the excitation circular frequency; A,B and C are the magnitudes of the velocity field; and $\phi$'s are the phase components relative to the forcing signal. Once vibrating, the structure is ready for the next step in the velocity imaging process, region of interest definition.

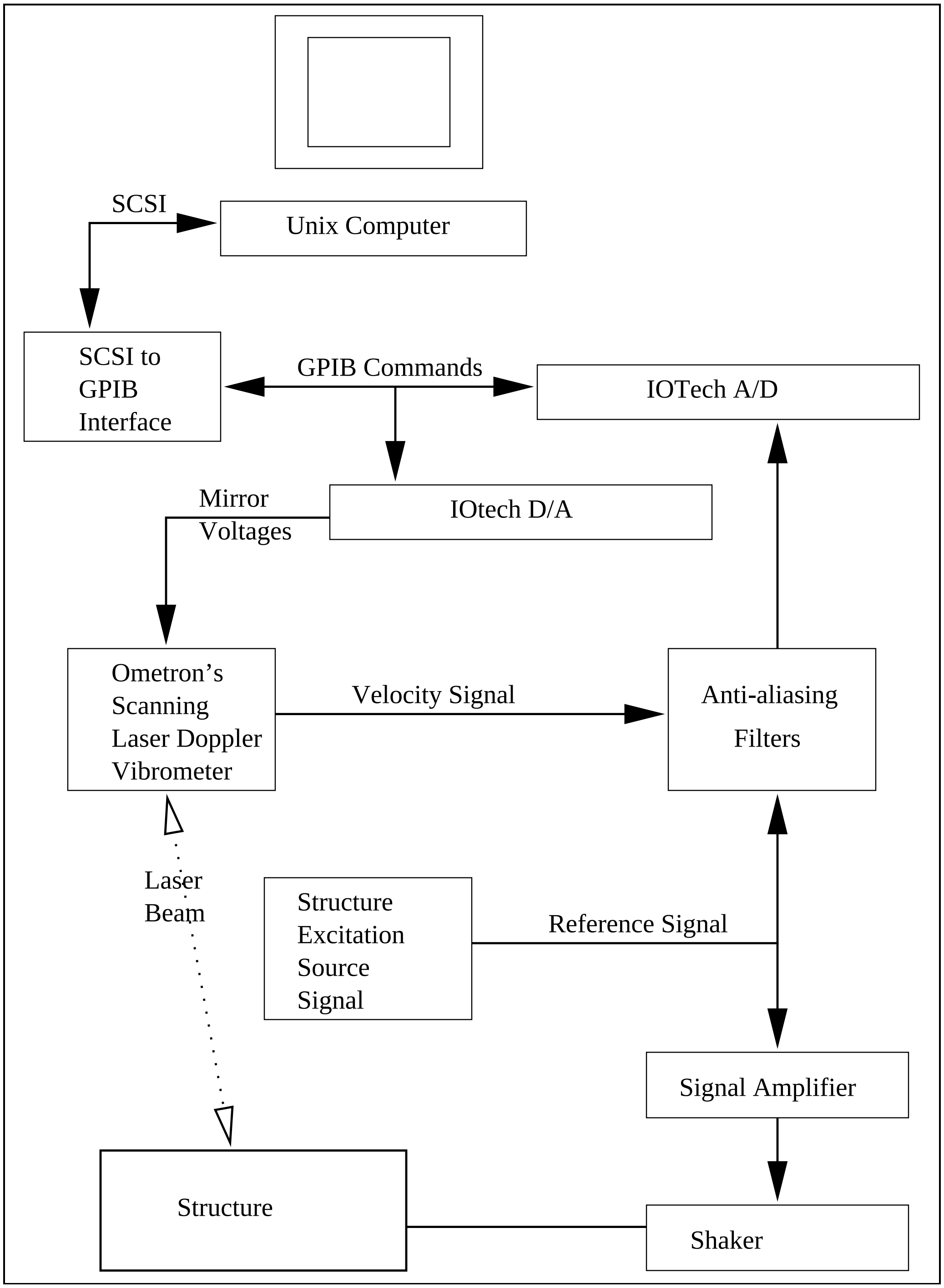

Figure 3.2: Data Acquisition Hardware

### 3.2.1 Velocity Region of Interest Definition

The user must define the area of the structure to be scanned by the SLDV. The velocity scan area is defined by directing the laser beam to four corners of the selected area. Direction of the laser beam is accomplished with a graphical user interface(GUI). Integer data generated with this GUI are used as digital to analog conversion(DAC) step values. Next these DACs values are inserted into general purpose instrument bus (GPIB) commands and sent to the IOtech D/A board to generate mirror control voltages, see Figure 3.2. The IOtech board is a 12 bit D/A (plus a sign bit) [27] board so that DAC values range from -4096 to 4096. The five volt range is selected for the IOtech D/A board to match the SLDV mirror galvanometer input range. At the end of this procedure the user has four integer pairs representing the laser beam's DAC coordinates for the four corners of the scan area. These coordinates are used to determine a min/max box (in DAC coordinates) which is divided into N rows and M columns, e.g. 11x12. These row-column DAC coordinate pairs are the individual pixels which will be scanned by the SLDV and are placed in a scanlist file, Figure 3.3. The simple reason for defining a region of interest is the time necessary to acquire each pixel of data. At present, the software can acquire six pixels per second. Thus a full 8192x8192 image would require approximately 3107 hours for one image. The practical compromise is the definition of a ROI which may be acquired in a timely fashion. Once the scanlist for the ROI is finished, actual data acquisition begins.

### 3.2.2 Pixel Data Acquisition

The velocity image of the region of interest results from postprocessing time series data taken at pixel coordinates determined in the scanlist. As noted in the previous section, a region of interest is defined so that a NxM velocity image will result once each pixel is traversed. This is a serial process as the SLDV has a single detector, not an array of detector sites as found on charge couple detectors (although the CCD image may be clocked out serially). As the velocity signal is acquired, the shaker's excitation signal is also acquired as the reference signal. This procedure differs from previous research [40, 12] where the force signal was the reference signal. The advantage of this procedure is a clear, reliable reference signal at all times, even when the structure is near a resonant frequency. Note that the relative phase of the resultant velocity field is not defined in the conventional way, i.e. dynamics models, but

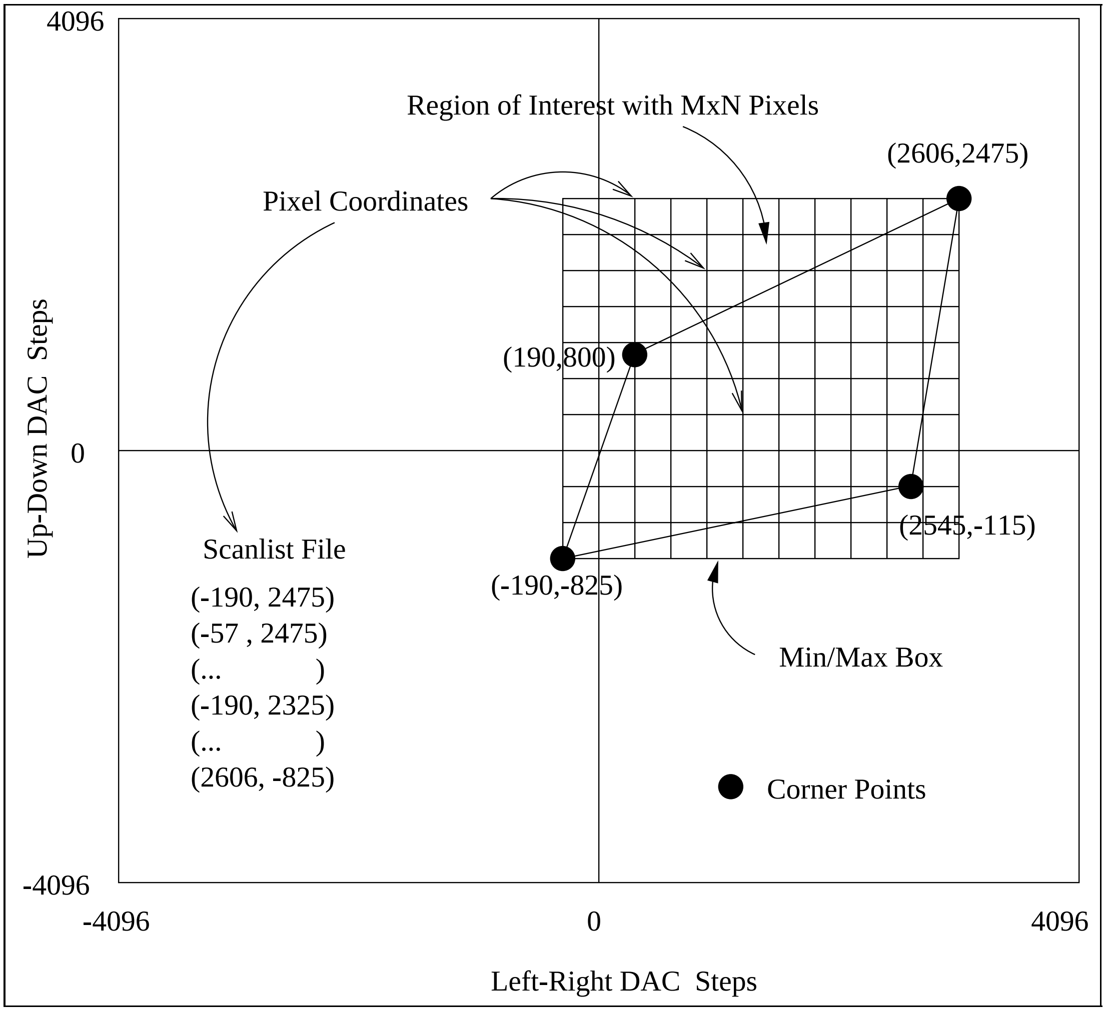

Figure 3.3: Region of Interest Definition

could be if desired. Thus for each pixel location, two streams of simultaneous, sinusoidal data are taken with an IOtech analog to digital (A/D) converter which has 16 bit precision [28], see Figure 3.2. The next section decribes processing of this data.

### 3.2.3 Pixel Data Processing

The two data streams, the velocity and reference signals, are fitted with a least square's regression procedure [44] and processed so that the magnitude and phase of the velocity with respect to the reference signal are obtained for each pixel location. If the excitation frequency is $\omega_{ex}$, then the voltage (velocity) measured at time t is

$$V_{meas}(t) = A\cos(\omega_{ex}t) + B\sin(\omega_{ex}t) + C. \tag{3.2}$$

The time series data begins at time $t_1$ and ends at $t_n$,

$$\begin{array}{llll} v_{meas}(t_1) & = A\cos(\omega_{ex}t_1) & +B\sin(\omega_{ex}t_1) & +C \\ v_{meas}(t_2) & = A\cos(\omega_{ex}t_2) & +B\sin(\omega_{ex}t_2) & +C \\ \vdots & \vdots & \vdots & \vdots \\ v_{meas}(t_n) & = A\cos(\omega_{ex}t_n) & +B\sin(\omega_{ex}t_n) & +C \end{array}. \tag{3.3}$$

Fitting the time series data using the least squares technique results in the following matrix equations,

$$\left\{ \begin{array}{c} v_{meas}(t_1) \\ v_{meas}(t_2) \\ \vdots \\ v_{meas}(t_n) \end{array} \right\} = \left[ \begin{array}{ccc} \cos(\omega_{ex}t_1) & \sin(\omega_{ex}t_1) & 1 \\ \cos(\omega_{ex}t_2) & \sin(\omega_{ex}t_2) & 1 \\ \vdots & \vdots & \vdots \\ \cos(\omega_{ex}t_n) & \sin(\omega_{ex}t_n) & 1 \end{array} \right] \left\{ \begin{array}{c} A \\ B \\ C \end{array} \right\}, \tag{3.4}$$

$$\{v_{meas}\} = [S]\{A\}, \tag{3.5}$$

$$[S]^T\{v_{meas}\} = [S]^T[S]\{A\}, \tag{3.6}$$

$$\left[[S]^T[S]\right]^{-1}[S]^T\{v_{meas}\} = \left[[S]^T[S]\right]^{-1}[S]^T[S]\{A\}, \tag{3.7}$$

$$\left[[S]^T[S]\right]^{-1}[S]^T\{v_{meas}\} = \{A\}. \tag{3.8}$$

The coefficients of $\{A\}$ are the regressed values for the velocity and reference signals. The offset term is discarded and the regressed values may be placed in complex form by

$$V_{vel}(t) = A_{vel}\cos(\omega_{ex}t) + iB_{vel}\sin(\omega_{ex}t), \tag{3.9}$$

$$V_{ref}(t) = A_{ref}\cos(\omega_{ex}t) + iB_{ref}\sin(\omega_{ex}t). \tag{3.10}$$

The phase angles of the equations above, equations 3.9 and 3.10, are dependent on the initiation time of the data sampling process, which is arbitrary. Fortunately, the phase angle between the velocity and reference signals at a point is constant. Letting $\overline{V}$ be the complex conjugate, this relative phase can be found by

$$T(t) = \overline{V_{ref}(t)} \circ V_{vel}(t), \tag{3.11}$$

$$\psi_{relative} = \arctan(\frac{Im(T(t))}{Re(T(t))}). \tag{3.12}$$

The magnitude of the velocity signal is easily determined so that the velocity signals may be rewritten as

$$V_{magn} = (\overline{V_{vel}} \circ V_{vel})^{\frac{1}{2}}, \tag{3.13}$$

$$V'_{vel}(t) = V_{magn}e^{i(\omega_{ex}t+\psi_{relative})}, \text{ or} \tag{3.14}$$

$$V'_{vel}(t) = V_{magn}(\cos(\omega_{ex}t + \psi_{relative}) + i\sin(\omega_{ex}t + \psi_{relative})). \tag{3.15}$$

At time $t = 0$ this form may be reduced to a complex number which is the saved pixel value at pixel location (i,j). At time $t = 0$, the velocity at pixel (i,j) is

$$V'_{vel}(0) = V_{magn}(\cos(\psi_{relative}) + i\sin(\psi_{relative})), \tag{3.16}$$

which is simply

$$V_{vel}(i,j)' = A' + iB'. \tag{3.17}$$

$V'_{vel}$ is the velocity of the "pixel" relative to the reference signal.

### 3.2.4 Sample Velocity Image

The final result of processing all the pixels is a velocity image. Each pixel contains a complex number which represents the measured line-of-sight velocity with respect to the reference signal. This velocity image is one of the basic data types used in this research. The following images depict typical data sets. Figure 3.4 is the real and imaginary velocity data before correction for the phase angle relative to the reference signal, Equation 3.9; adjacent pixels have widely varying real and imaginary values. Figure 3.5 is the real and imaginary velocity data after phase correction; the real and imaginary values vary smoothly from pixel to pixel, Equation 3.17. Figure 3.6 is the magnitude and phase before phase correction; the magnitude values vary smoothly, but the phase varies wildly from pixel to pixel. Figure 3.7 is the corrected and smoothly varying magnitude and phase data. To perform data fusion on multiple velocity images, the pose of the SLDV must be determined at each imaging viewpoint. The next chapter presents an automated procedure for the SLDV's pose.

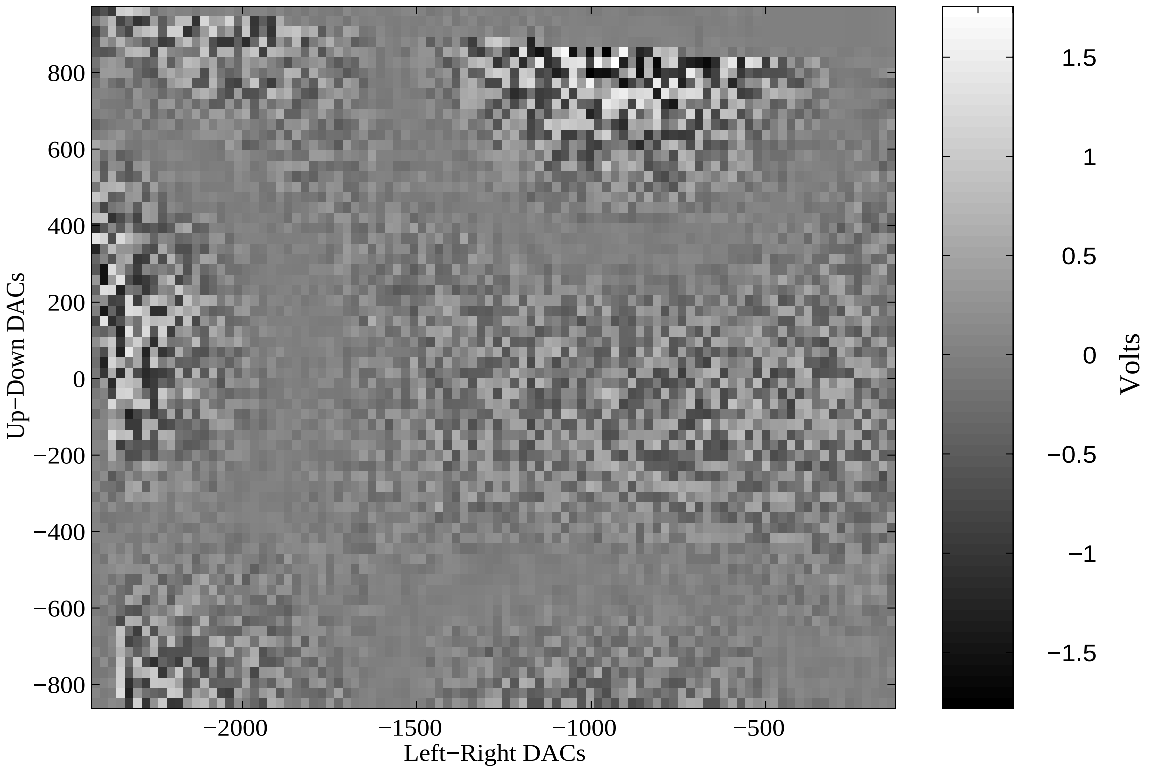

Real

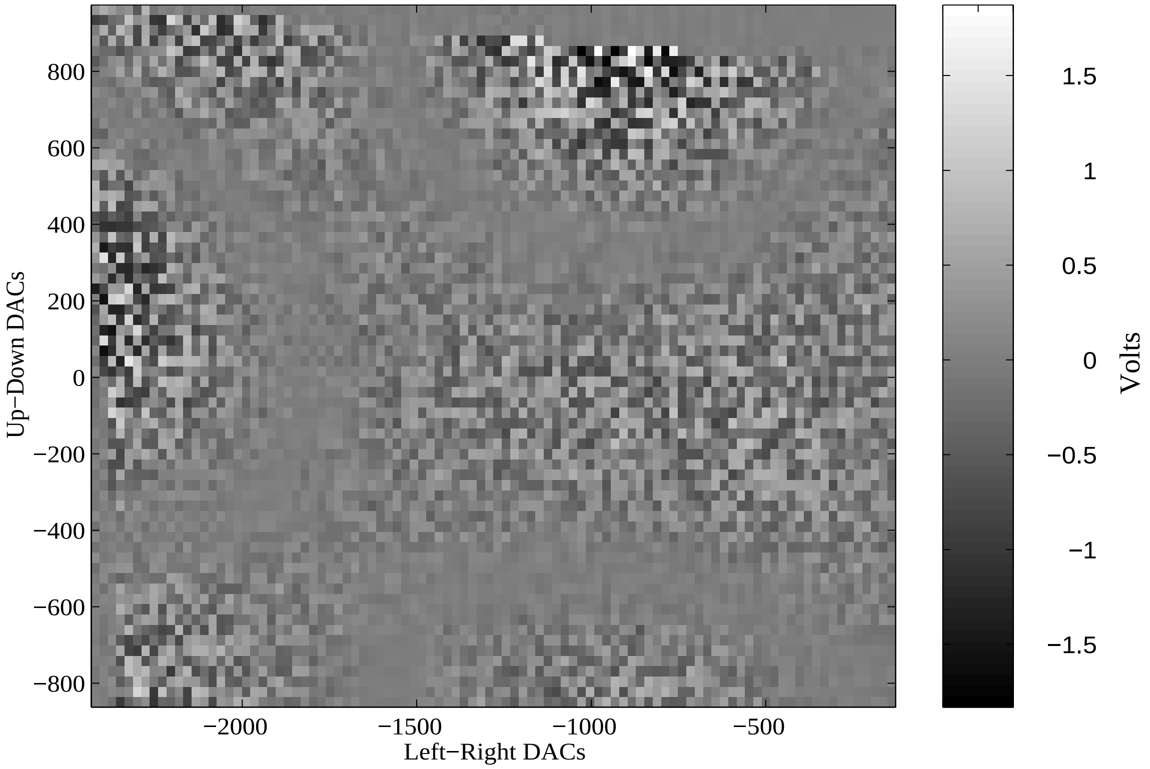

Imaginary

**Figure 3.4: Real and Imaginary Data Before Phase Correction**

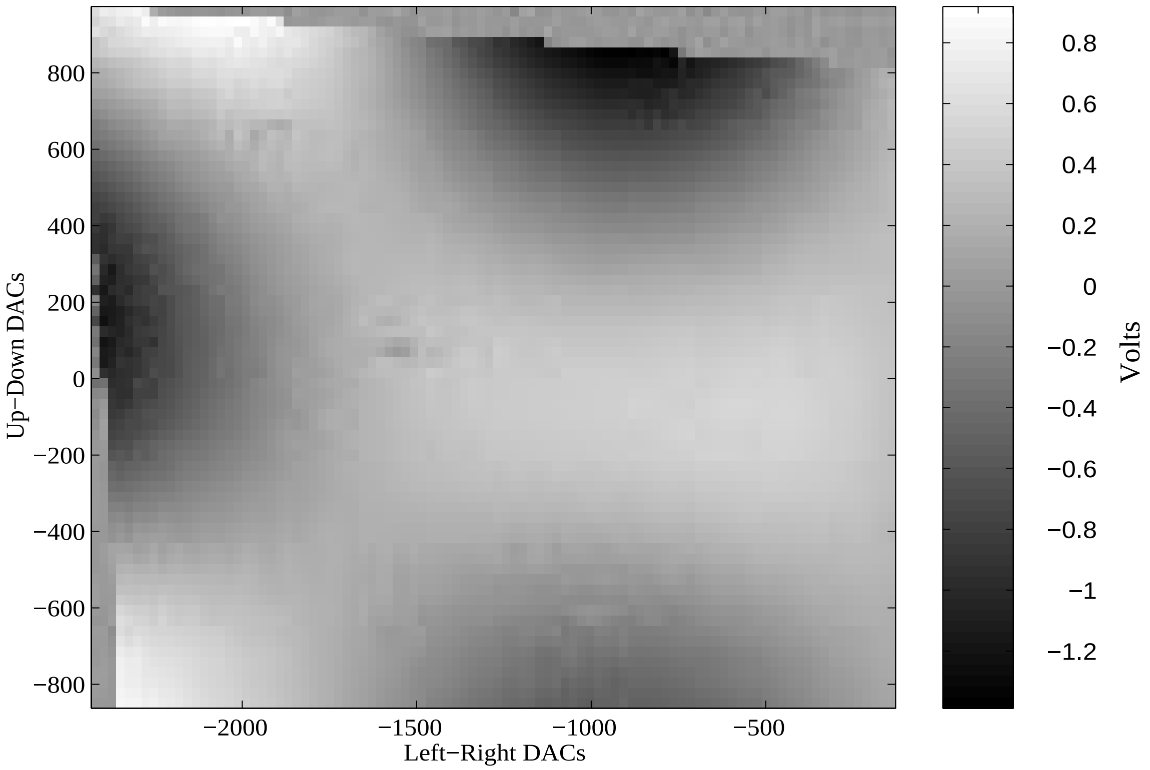

Real

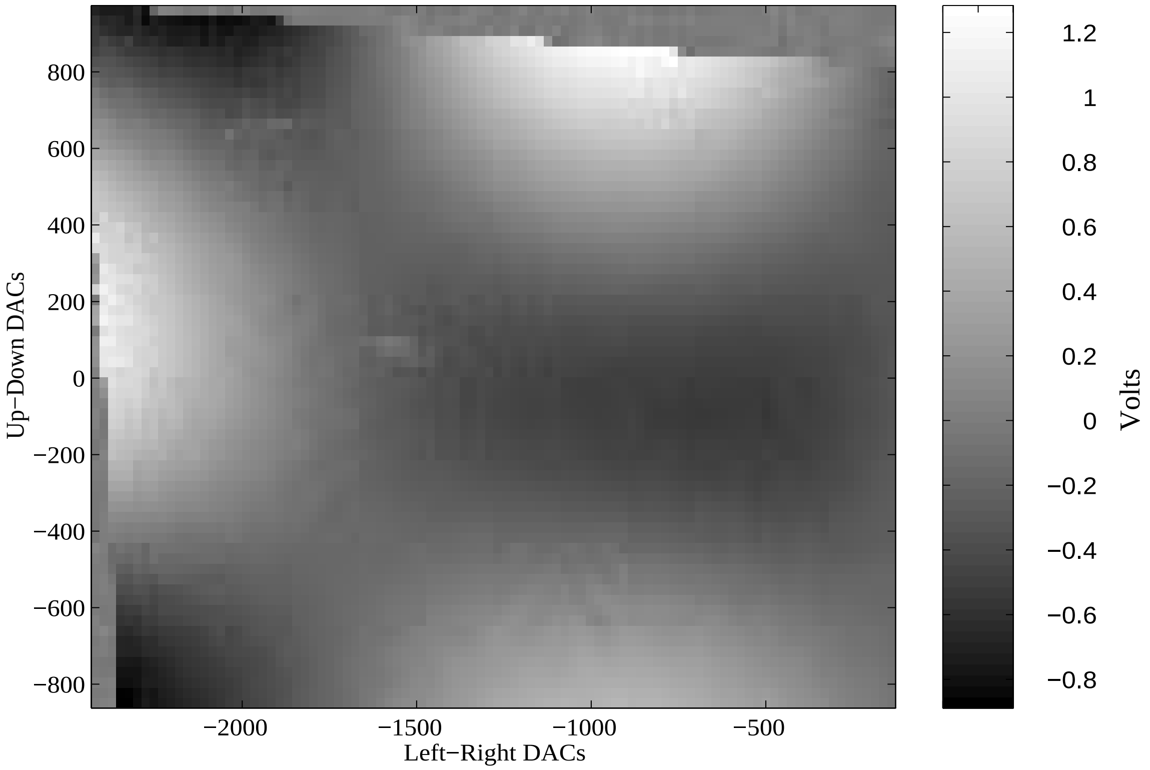

Imaginary

**Figure 3.5: Real and Imaginary Data After Phase Correction**

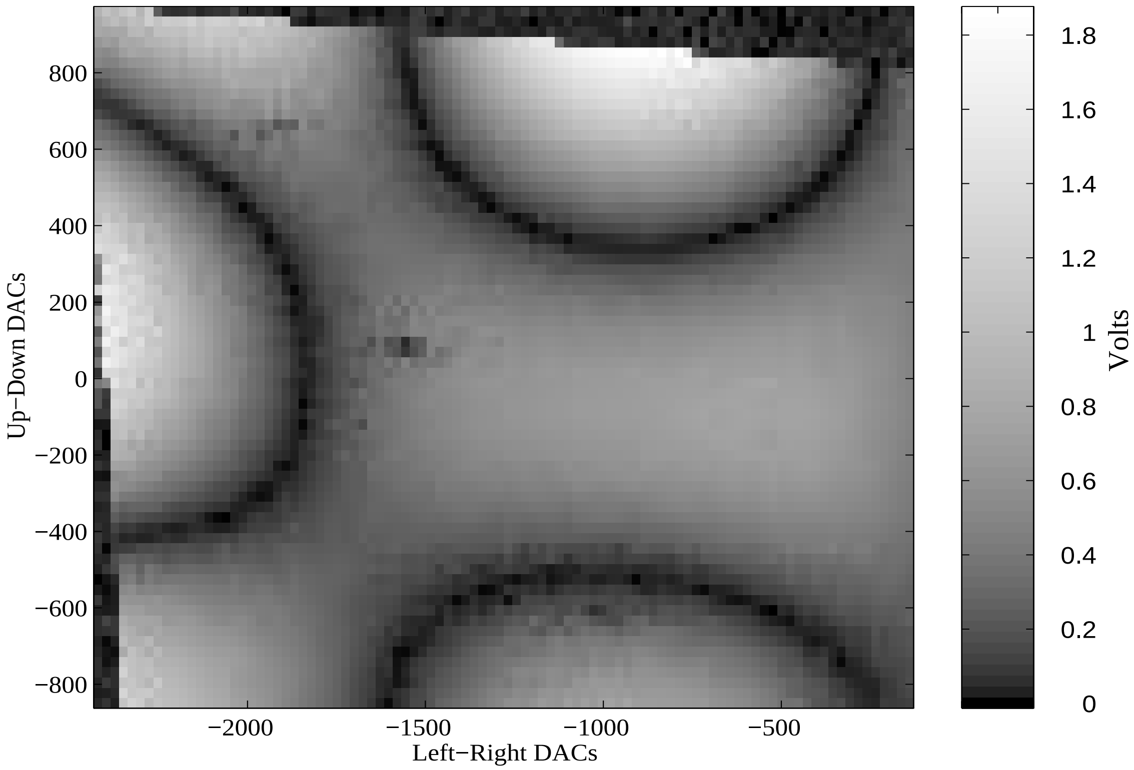

Magnitude

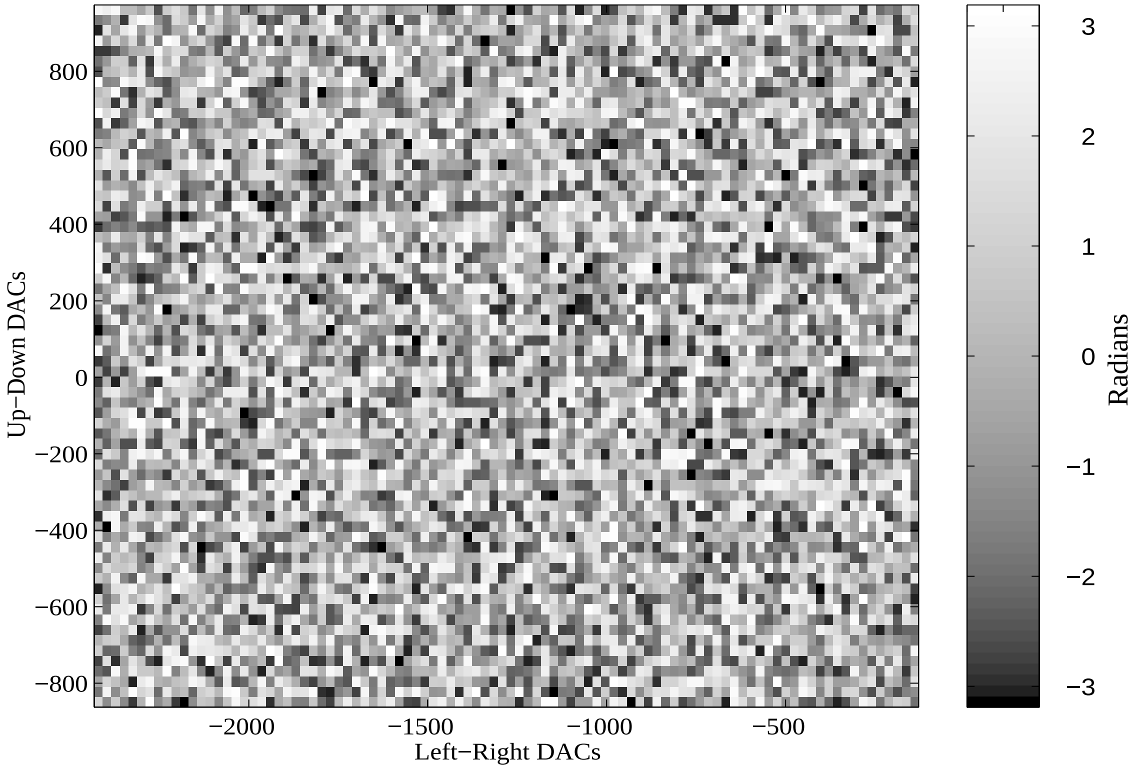

Phase

**Figure 3.6: Magnitude and Phase Before Phase Correction**

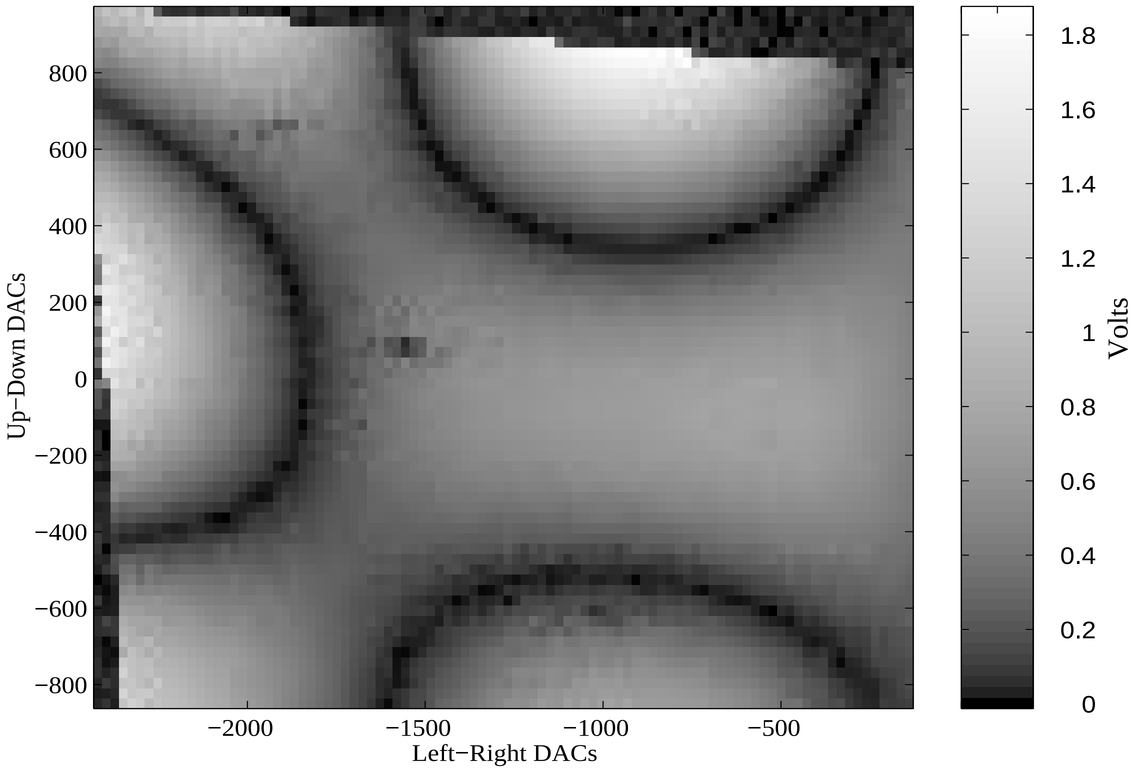

Magnitude

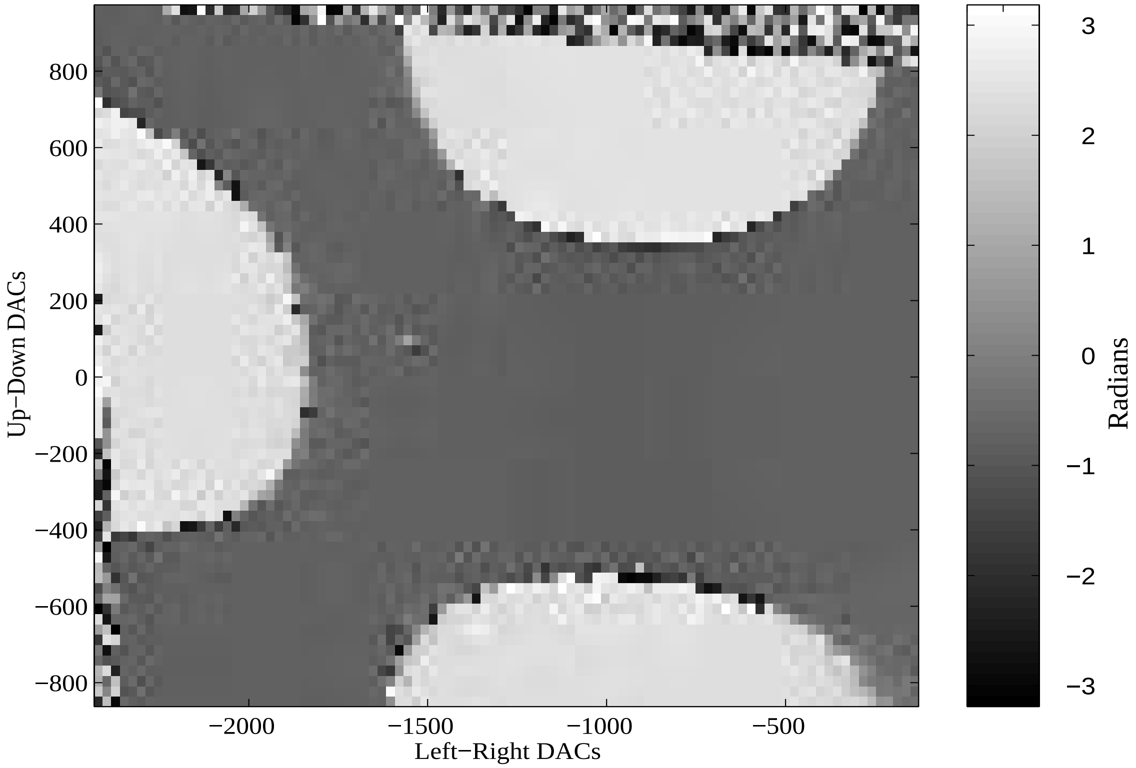

Phase

**Figure 3.7: Magnitude and Phase After Phase Correction**

# Chapter 4

# SLDV Pose Automation

The SLDV pose process may be automated if the SLDV is viewed as a projective camera. As a projective camera, an appropriate computer vision model and associated algorithms may be developed to automate the SLDV's pose process. The SLDV's pose is important since the three-dimensional velocity field reconstruction requires an accurate and precise determination of the SLDV's pose. The current pose algorithm employs a registration procedure which requires the laser operator to point the laser at registration points and visually confirm when the laser is at the object "point". This visual confirmation procedure introduces human errors which degrade the accuracy of the pose estimation and precludes statistical procedures which would improve the estimate of the pose. By introducing a SLDV computer vision model and a coordinate calibration object into the pose determination process, the pose process can be automated and the pose problem decoupled from the test structure. Thus systematic and human errors can be significantly reduced with an automated registration procedure. The automated procedure premits more registration points and independent "shots" of the registration points for better statistical estimates. The following sections describe the current procedure, the coordinate calibration object, the SLDV computer vision model, the automated process, and the experimental tests which verify the performance of the automated procedure.

## 4.1 Pose Automation

Velocity reconstruction requires velocity images from multiple SLDV viewpoints where the SLDV's positions and orientations are known. Previous researchers have developed registration (pose) algorithms which determine this transformation from matched object and image points. This research extends this work by automating this procedure to improve the accuracy and precision of the estimated transformation. The following sections present the development of the automated algorithm and the implementation.

## 4.2 Current Registration Procedure

The current registration procedure consists of four steps. First the structure, with a set of known object points, is placed within the viewing volume of the SLDV. Next the laser operator points the laser at the fiducial marks located on the test structure and records the mirror angles (or voltages). When this step is completed, an associated set of mirror angles and object (structural) points are available for an input file for the various pose algorithms developed by Lindholm [34], Montgomery [40], and Zeng [61]. (Stafne[55] developed a mirror voltage (or DACs) to mirror angle calibration procedure; his results are used in this research.) These pose algorithms return a 4x4 matrix which represents the translation and rotation of the SLDV with respect to the structure. This completes the registration process. This process may be improved with an automated pose procedure.

## 4.3 Requirements for Pose Algorithm

The current pose algorithms require an input file which provides matched object and image points. Object points have been typically marked on the structure itself. Image points, mirror angles or voltages, are derived from the SLDV user directing the laser beam to the object points. This procedure presents two significant sources of error: accuracy and precision of the object point coordinates and the human error from pointing the laser to the object points. These errors may be reduced by using a calibrated object with known features which may be sensed by the SLDV. These features may be sensed, reconstructed, and processed to provide superior input data, the object and image points, for the pose alogrithms.

## 4.4 Automated Pose Procedure

The automated registration is a five step procedure. First the coordinate calibration object, with a set of known, geometric features (machined washers masking speakers), is placed within the viewing volume of the SLDV. Next, the SLDV scans the structure and records a velocity image of the calibration object. Since the SLDV senses only the masked, vibrating speakers, this velocity image may be processed to obtain the geometric images of the circular washers - ellipses. These ellipses are further processed to obtain a set of invariant points with the associated mirror angles. This final object-point/image-point set of data is used as an input file for the pose algorithms and the automated process is complete.

### 4.4.1 Object Points

To improve the pose algorithm, the object points must be known as accurately and precisely as possible. The coordinate calibration object is a plane with four circular features detectable by the SLDV. The calibration object is shown in Figure 4.1. The four circular features are machined washers mounted on a flat plane. These washers mask ordinary speakers so that when these speakers are driven with an excitation signal, the SLDV can detect the edge between the moving speaker and the stationary washers. The washsers' circular features are measured with a coordinate measurement machine (±0.00005") to achieve the best object coordinates. To determine specific object points, selected bitangents among the circles are used to calculate bitangent points. For the calibration object depicted in Figure 4.1, the coordinates for the bitangent points are listed in Table 4.1. These coordinate values are more accurate and precise than previous fiducial marks on the structure where the fiducial coordinates were known within $\pm\frac{1}{64}$inch. Once the object points are known, the corresponding image points must be determined.

### 4.4.2 Image Points

Placing the SLDV in a computer vision context permits the development of a procedure to automatically determine the image points which match the bitangent points of the calibration object. First the SLDV computer vision model is developed. The SLDV computer vision model is evaluated to determine if this model is a true projectivity. Once the projective relationships are established, the implemented algorithm is described and validated.

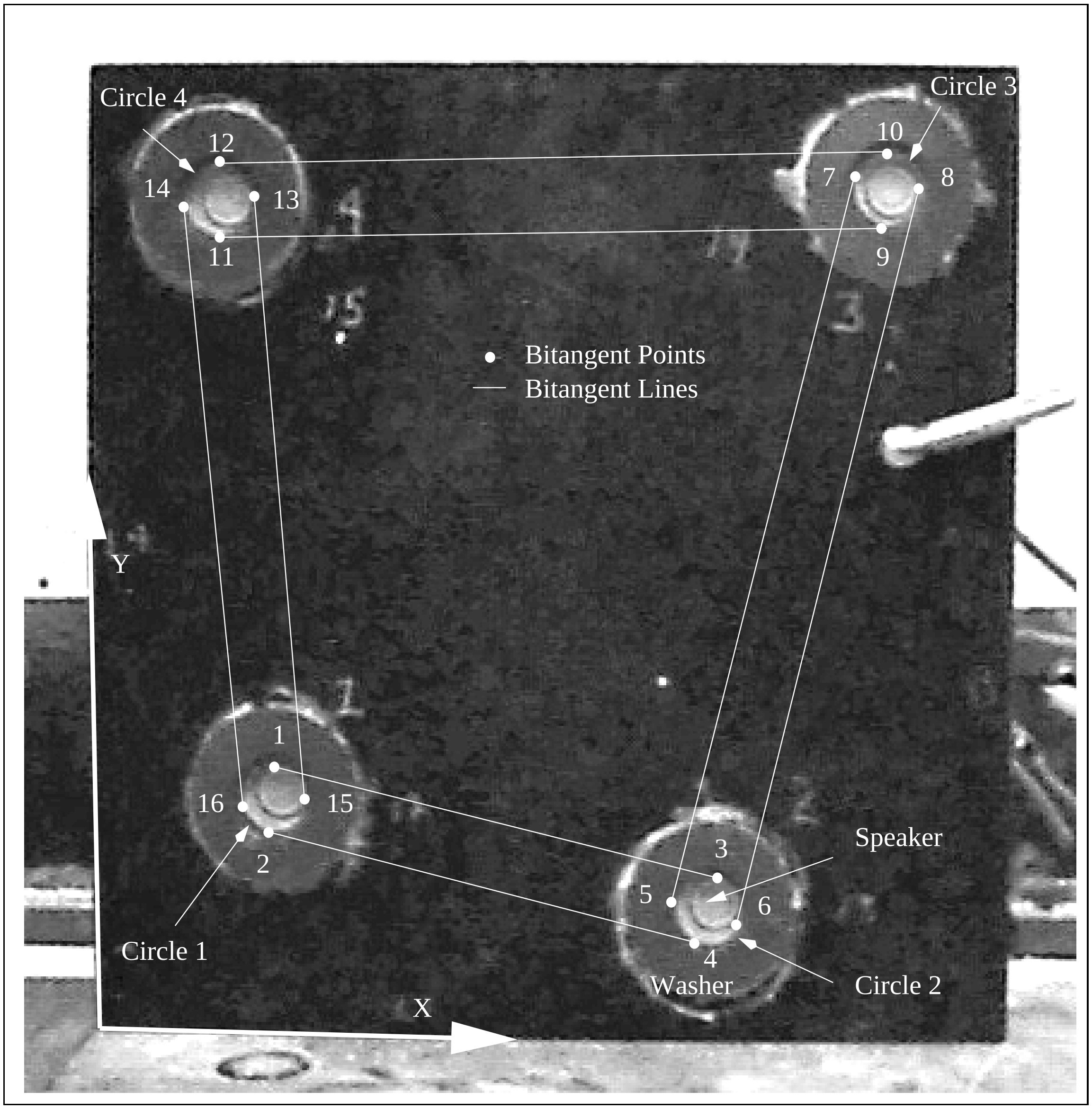

Figure 4.1: Calibration Object

**Table 4.1: Coordinates of Features and Bitangent Points**

| Circle no. | X (in) | Y (in) | DIA (in) |
|---|---|---|---|
| 1 | 2.2574 | 2.8216 | 0.8090 |
| 2 | 7.4654 | 1.6073 | 0.8161 |
| 3 | 9.4997 | 9.7075 | 0.8206 |
| 4 | 1.5810 | 9.5402 | 0.8014 |

| Point no. | X (in) | Y (in) | Z (in) |
|---|---|---|---|
| 1 | 2.3490 | 3.2156 | 0.0000 |
| 2 | 2.1653 | 2.4277 | 0.0000 |
| 3 | 7.5578 | 2.0048 | 0.0000 |
| 4 | 7.3725 | 1.2100 | 0.0000 |
| 5 | 7.0696 | 1.7066 | 0.0000 |
| 6 | 7.8611 | 1.5078 | 0.0000 |
| 7 | 9.1017 | 9.8073 | 0.0000 |
| 8 | 9.8976 | 9.6075 | 0.0000 |
| 9 | 9.4905 | 9.2973 | 0.0000 |
| 10 | 9.5079 | 10.1177 | 0.0000 |
| 11 | 1.5890 | 9.9408 | 0.0000 |
| 12 | 1.5721 | 9.1396 | 0.0000 |
| 13 | 1.9797 | 9.5806 | 0.0000 |
| 14 | 1.1823 | 9.5003 | 0.0000 |
| 15 | 2.6598 | 2.8623 | 0.0000 |
| 16 | 1.8549 | 2.7813 | 0.0000 |

### 4.4.3 SLDV Computer Vision Model

The SLDV is best modeled as a modified camera. Manufactures' of SLDV systems often refer to the acquired data set as a "velocity image"; this suggestive terminology reflects the idea that the SLDV is a "camera" with a differing modality (or spectral sensitivity) and imaging surface. The following paragraphs describe the extent to which the camera analogy applies to the SLDV so that the body of knowledge developed in the photographic and computer vision disciplines may be employed in the processing of the velocity images.

#### 4.4.3.1 Pin-Hole Camera Model

The modern electronic camera is modeled as a pin-hole camera, e.g. all light rays are in perspective from a point, Figure 4.2. The camera is placed within a world coordinate system and its position and orientation are determined by the extrinsic parameters (translation and rotation). The camera's intrinsic parameters are its focal length and image offsets. Included in the intrinsic parameters are distortion corrections so that the image coordinates combined with all the intrinsic and extrinsic parameters define the light ray whose intensity is being measured. If the focal length is combined with the image coordinates, an orthogonal axis coordinate system may be defined. In this manner the light ray is defined by the intersection of two planes, Figure 4.3. A similar two-plane intersection model can be used for the SLDV.

#### 4.4.3.2 Offset Orthogonal Axis Coordinate System

The SLDV does not have the essential feature of the camera model - the pin-hole which places the bundle of rays in perspective; the SLDV has two offset orthogonal mirrors which produce a bundle of light rays, but without a common fixed focal point. This is clearly seen when the laser beam in the SLDV is modeled as the join of two planes. That the light rays and laser beam may be modeled as two bundles of planes is the similarity between the two imaging systems. The virtual image plane (more precisely a 2-D manifold) adopted for the SLDV are these two bundles of planes whose image coordinates are mirror DAC steps or mirror angles, see Figure 4.4. This virtual image plane preserves cross-ratios. Since cross-ratios are projectively invariant and the SLDV is not a pin-hole camera (single perspective) the SLDV is a projective camera. Additionally, the projective nature of the SLDV preserves

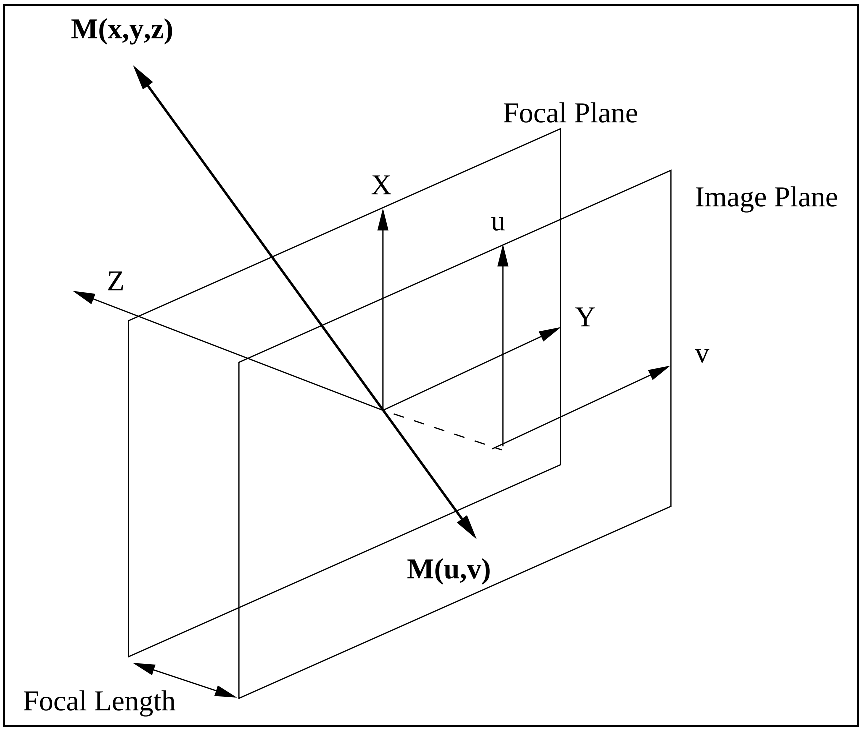

Figure 4.2: Pinhole Camera Model

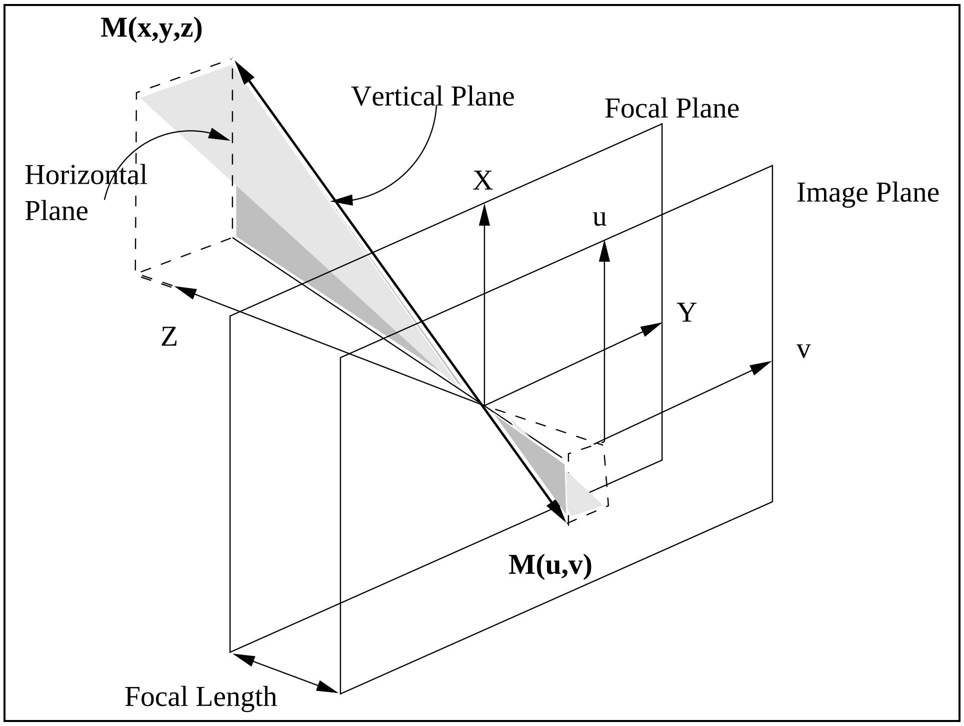

Figure 4.3: "Two Plane" Camera Model

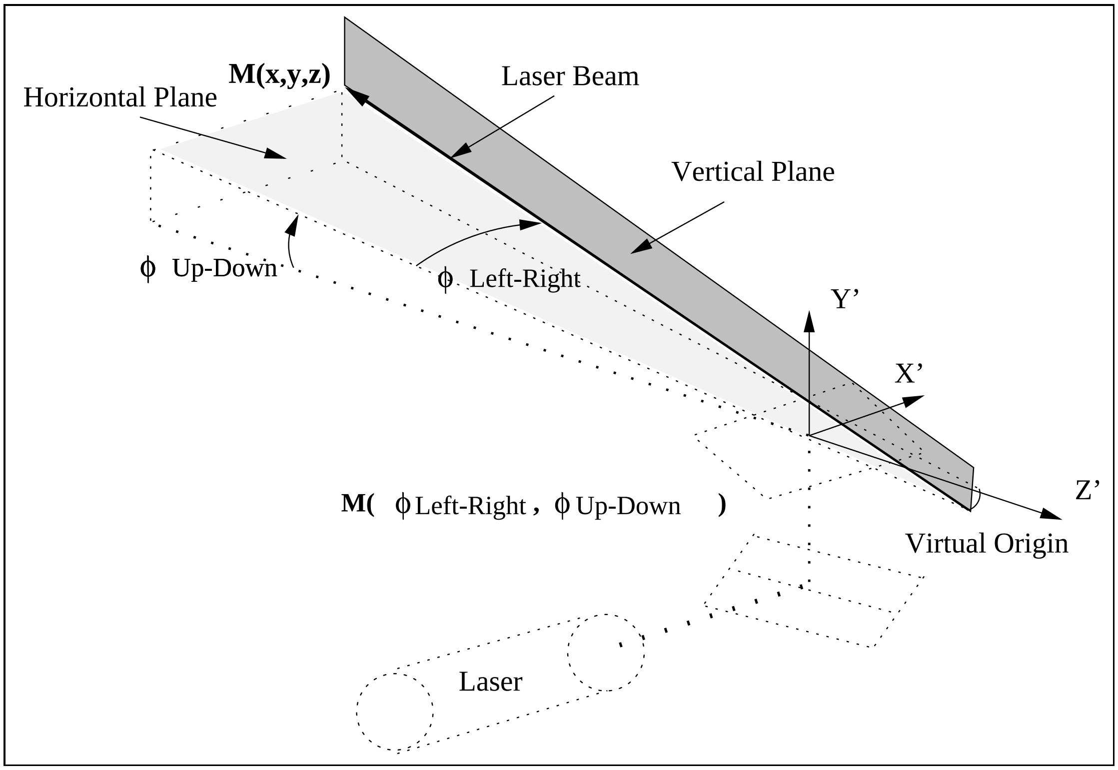

Figure 4.4: SLDV Two-Plane Camera Model

collineations which will be important to the pose automation process. Before examining the projective aspects of the SLDV, the intrinsic and extrinsic parameters of the SLDV must be defined to complete the computer vision model.

#### 4.4.3.3 Intrinsic Parameters

The SLDV and the pin-hole camera intrinsic parameters are fundamentally different. The SLDV has no focal plane and, therefore, no focal length. The intrinsic parameter in the SLDV is the mirror axis separation distance. Together with the mirror angles this parameter permits the determination of the "light" rays for the SLDV model. Placing the light rays into the world coordinate system requires knowledge of the extrinsic parameters.

#### 4.4.3.4 Extrinsic Parameters

The SLDV and the camera share the same definition of extrinsic parameters. The position and orientation of the SLDV with respect to the world coordinate system are essential to fuse the different sets of velocity data together. The question is, where is the laser's local coordinate system? The camera has a natural coordinate system determined by the focal plane and focal point. Since the SLDV has neither focal plane or point, a natural choice of coordinate system is not obvious. Yet the mirror axes provide a system to determine the orientation, but not position. Although not physically accessible, the point on the up-down mirror axis which contains the laser beam in its home position will be taken as the local origin for the laser's coordinate system. The laser coordinate system is shown in Figure 4.5 and follows Zeng's research[61]. The SLDV model is described in Zeng's dissertation [61, p.14], but is restated below:

$$\begin{aligned} \mathbf{P}_{lcs} &= \mathbf{P}_{wcs}\,[T_x]_{wcs}^{lcs}\,, && (4.1)\\ \theta_{ud} &= \tan^{-1}(P_{y,lcs}/P_{z,lcs}), && (4.2)\\ \theta_{lr} &= \tan^{-1}(P_{x,lcs}/(\sqrt{P_{y,lcs}^2+P_{z,lcs}^2}+\text{mirror offset}). && (4.3) \end{aligned}$$

Now that the SLDV intrinsic and extrinsic parameters are defined, virtual imaging surfaces are easily developed.

#### 4.4.3.5 Image Surfaces

The two imaging surfaces used in this research are a virtual imaging plane and a surface whose normals coincide with the direction of the light rays - a torus. The second surface is a convenient embedding of the virtual imaging plane. A torus may be defined[35, p.158] by

$$\mathbf{X}(\theta,\psi) = (b + a\sin\psi)\cos(\theta)\mathbf{e_1} + (b + a\sin\psi)\sin(\theta)\mathbf{e_2} + a\cos(\psi)\mathbf{e_3}, \qquad (4.4)$$

where $\theta, \psi$ are the surface coordinates, $a, b$ are the radii of the torus, and $\mathbf{e}_i$ are the standard unit vectors, Figure 4.6 .

Using Zeng's laser model[61] an object point $\mathbf{M}(x,y,z)$ in the laser coordinate system is defined

$$\mathbf{X}(\theta,\psi) = (-M_{offset} + L_p\cos\theta_y)\cos(\theta_x)\mathbf{e_3} + (-M_{offset} + L_p\cos\theta_y)\sin(\theta_x)\mathbf{e_2} + L_p\sin(\theta_y)\mathbf{e_1}. \qquad (4.5)$$

Identifying the appropriate unit vectors $\mathbf{e}_i$ with one another and letting $L_p = a$, $\psi = \theta_y + \frac{\pi}{2}$, and $M_{offset} = b$, the embedded image surface is clearly a torus. This is a helpful insight as the orthogonality of the $\theta, \psi$ parameters is easily shown[35, p.159] by taking derivatives with respect to each parameter,

$$\mathbf{X}_\theta = -(b + a\sin(\psi)\sin(\theta)\mathbf{e_1}) + (b + a\sin(\psi)\cos(\theta)\mathbf{e_2}), \qquad (4.6)$$

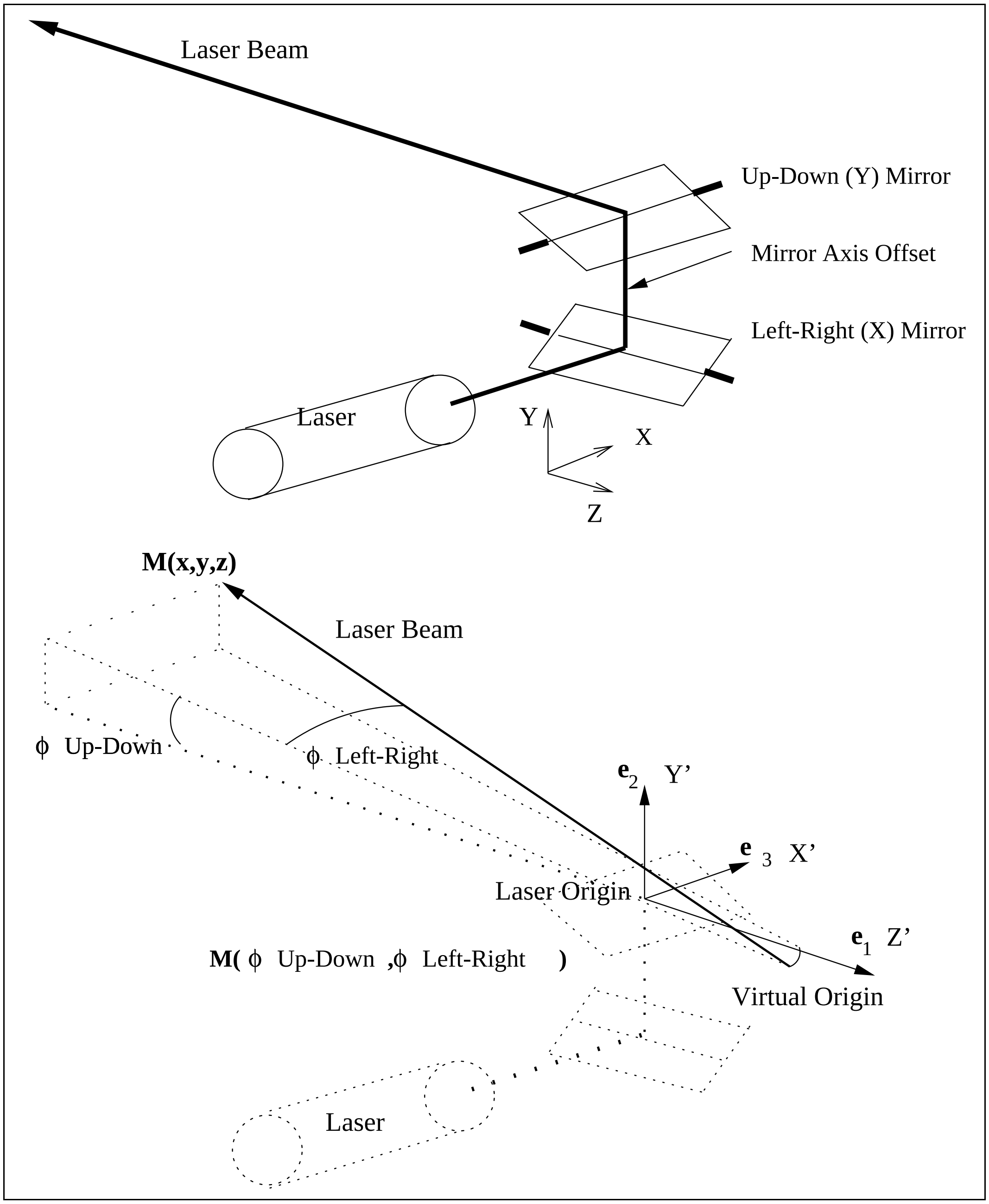

Figure 4.5: SLDV Computer Vision Model

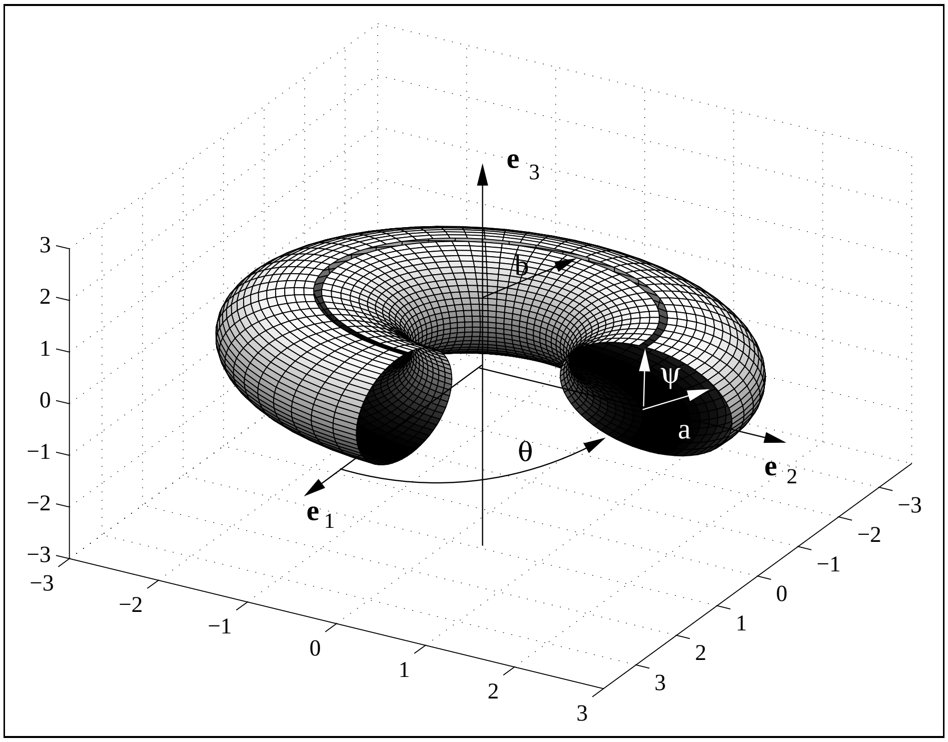

**Figure 4.6: SLDV Image Surface**

$$\mathbf{X}_{\psi} = (b + a\cos(\psi)\cos(\theta)\mathbf{e_1}) + (b + a\cos(\psi)\sin(\theta)\mathbf{e_2}) - a\sin(\psi)\mathbf{e_3}, \tag{4.7}$$

and then looking at the dot product,

$$\mathbf{X}_{\theta} \bullet \mathbf{X}_{\psi} = 0. \tag{4.8}$$

Physically this means that directing the laser beam, via the mirror input voltages, to an object point is order independent: moving the left-right mirror first and then the up-down mirror or vice versa does not affect the final position of the laser beam.

#### 4.4.3.6 Preserving Cross-Ratios

The projective nature of the SLDV computer vision model is demonstrated by examining how well the SLDV preserves cross-ratios. Since the imaging coordinates are orthogonal, the problem may be addressed one coordinate at a time. The next three sections define the cross-ratio and apply this concept to the specific cases for the up-down mirror and left-right mirror.

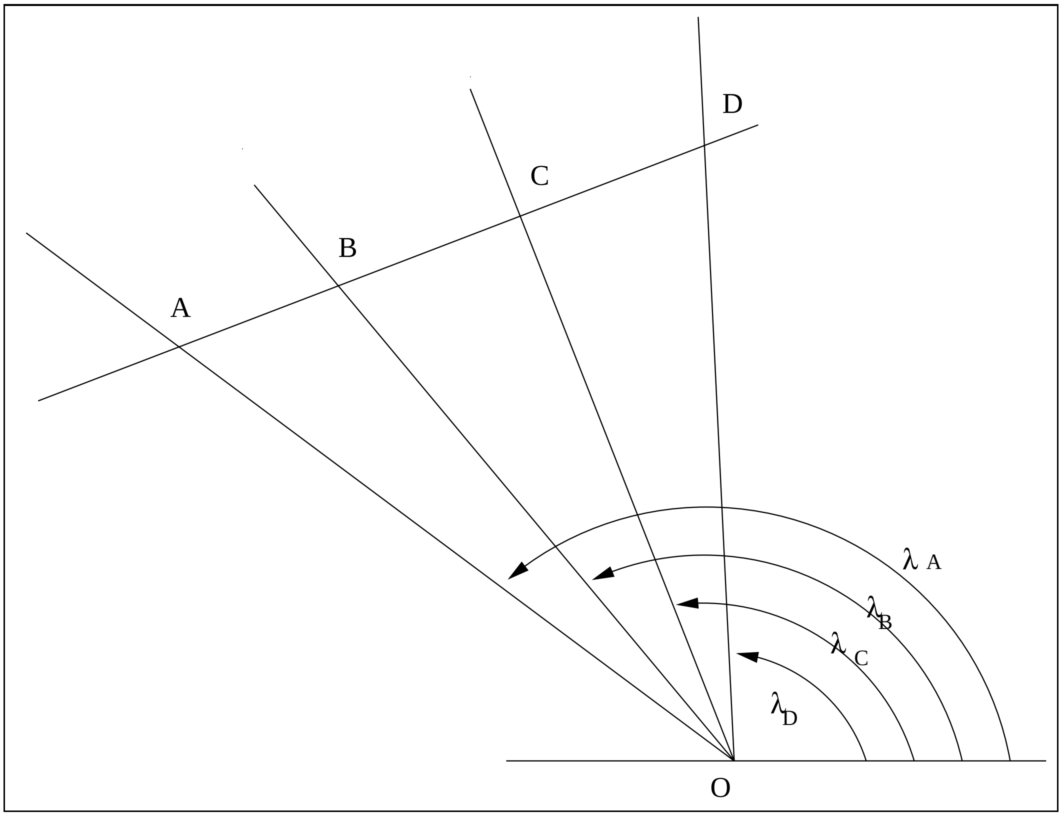

Figure 4.7: Cross-Ratio of Points, Slopes

#### 4.4.3.7 Cross-Ratios

The cross-ratio is the fundamental invariant of projective geometry [23]. If the cross-ratios of $(A, B, C, D)$ and $(A', B', C', D')$ are equal, then a projective transformation exists between the elements of the two sets [49]. One cross-ratio definition, which is convenient for N-dimensional points, is

$$cr(A, B, C, D) = \frac{\overline{ACBD}}{\overline{ADBC}}. \tag{4.9}$$

Here $A, B, C, \text{and} D$ are points and $\overline{AC}, \overline{BC}$, etc. are directed distances. For points on a line, the cross-ratio becomes

$$cr(A, B, C, D) = \frac{(x_C - x_A)(x_D - x_B)}{(x_C - x_B)(x_D - x_A)}. \tag{4.10}$$

If lines are drawn from these points, $A, B, C,$ and $D$, to another point $O$, then the cross-ratio between the points and the pencil of lines is preserved. Figure 4.7 depicts this situation. One may use either the slopes of the lines [23] or angles [3] to determine the cross-ratio.

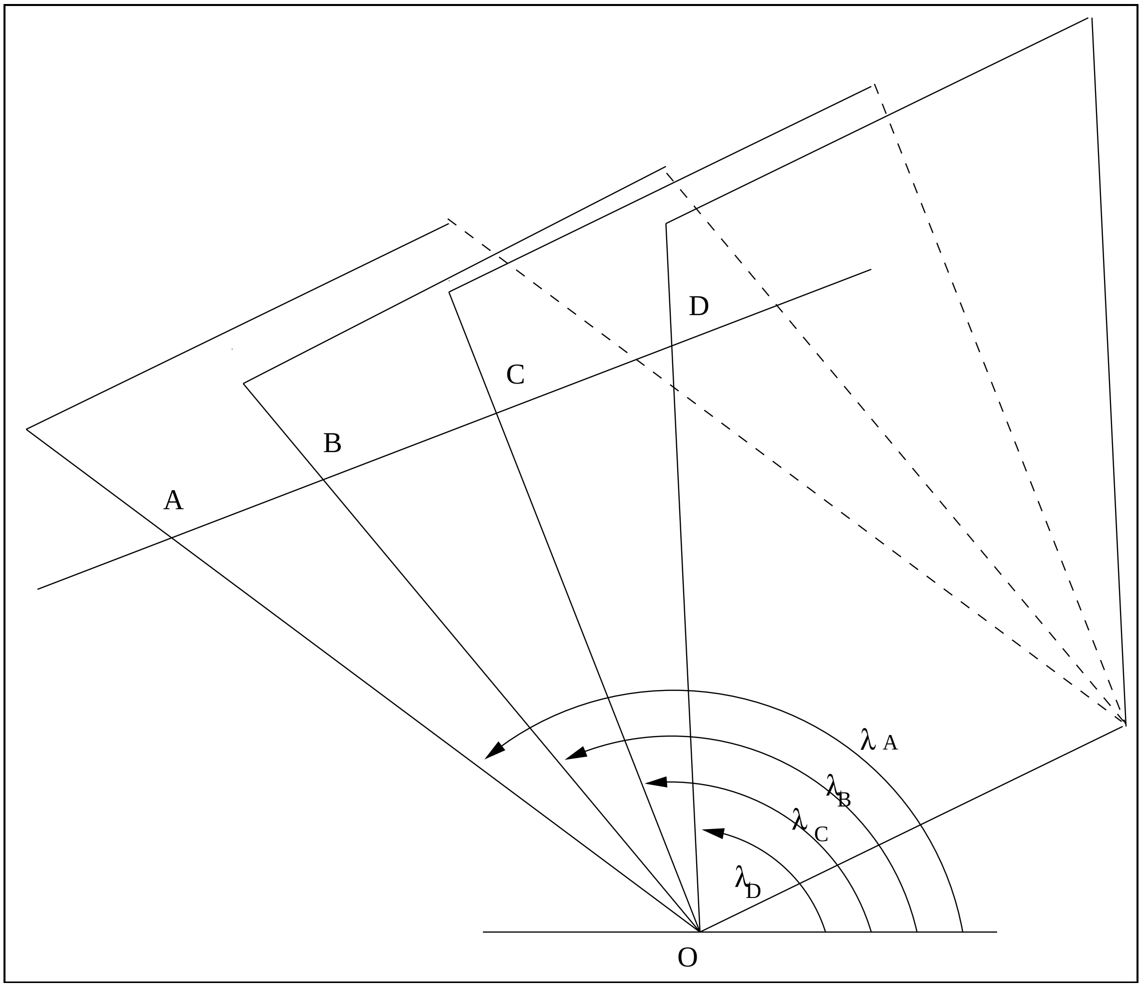

Figure 4.8: Cross-Ratio of Four Planes

The two definitions are

$$cr(A,B,C,D) = \frac{(\lambda_C - \lambda_A)(\lambda_D - \lambda_B)}{(\lambda_C - \lambda_B)(\lambda_D - \lambda_A)}, \tag{4.11}$$

$$cr(A,B,C,D) = \frac{(\sin(\angle AOC))(\sin(\angle BOD))}{(\sin(\angle BOC))(\sin(\angle AOD))}. \tag{4.12}$$

If the lines through point O in Figure 4.7 are extended to planes with a common axis through O, then the cross-ratio of the four planes remains unchanged. This is true because the angles among the planes are the same and the cross-ratio is preserved [16, 41]. Figure 4.8 shows this situation, which is analogous to the family of planes defining the SLDV's laser beam.

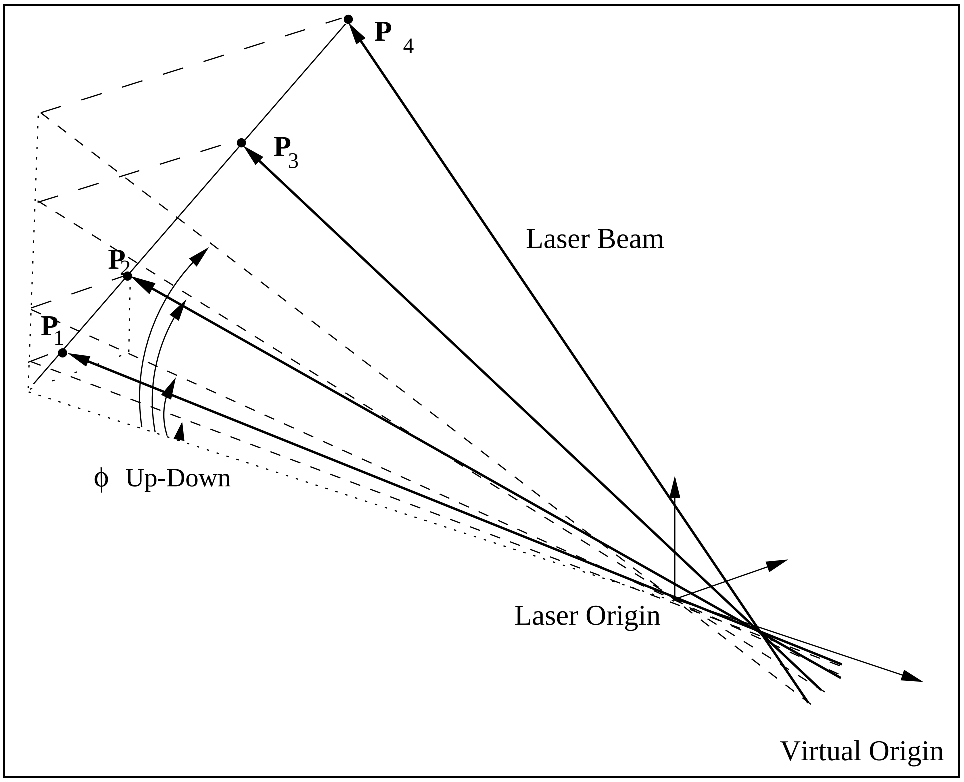

Figure 4.9: Cross-Ratio of Up-Down Mirror Angles

#### 4.4.3.8 Cross Ratio of the Up-Down Mirror

The SLDV up-down scanning mirror preserves cross-ratios. If the left-right mirror is held in a constant position (constant mirror voltage), then the cross ratio of the slopes of the up-down mirror planes, as these planes intersect specific points, are the same as the cross-ratio of the four points in the world coordinate system, Figure 4.9. Choosing $A, B, C,$ and $D$ to have world system coordinates on a line in space, the cross-ratio, $cr(A, B, C, D)$, is found using Equation 4.9. For example, let points in the world coordinate system (using homogenous coordinates or Cartesian coordinates where appropriate) be defined by

$$\mathbf{P}_{wcs} = \mathbf{P}_{lcs}\mathbf{T}_{lcs}^{wcs},$$

$$\begin{bmatrix} 0.7855 & 0.4456 & 0.4295 & 0 \\ -0.5707 & 0.7899 & 0.2243 & 0 \\ -0.2393 & -0.4213 & 0.8748 & 0 \\ 12.0000 & -7.0000 & -74.000 & 1 \end{bmatrix} = \mathbf{T}_{lcs}^{wcs},$$

$$\begin{aligned}
\mathbf{P}_{1,lcs}\mathbf{T}_{lcs}^{wcs} = [1,1,100,1]\mathbf{T}_{lcs}^{wcs} &= [-11.71,-47.89,14.13,1] = \mathbf{P}_{1,wcs}, \\
\mathbf{P}_{2,lcs}\mathbf{T}_{lcs}^{wcs} = [5,5,100,1]\mathbf{T}_{lcs}^{wcs} &= [-10.85,-42.95,16.74,1] = \mathbf{P}_{2,wcs}, \\
\mathbf{P}_{3,lcs}\mathbf{T}_{lcs}^{wcs} = [11,11,100,1]\mathbf{T}_{lcs}^{wcs} &= [-9.56,-35.53,20.67,1] = \mathbf{P}_{3,wcs}, \\
\mathbf{P}_{4,lcs}\mathbf{T}_{lcs}^{wcs} = [20,20,100,1]\mathbf{T}_{lcs}^{wcs} &= [-7.63,-24.41,26.55,1] = \mathbf{P}_{4,wcs},
\end{aligned}$$

then the cross-ratio is

$$cr(P_{1,wcs},P_{2,wcs},P_{3,wcs},P_{4,wcs}) = \quad cr(P_{1,lcs},P_{2,lcs},P_{3,lcs},P_{4,lcs}) = \quad 1.3158.$$

From Equation 4.2 the slopes of the up-down mirror planes containing the laser beam are

$$\lambda_i = \frac{P_{y_i,lcs}}{P_{z_i,lcs}}. \tag{4.13}$$

Using these slopes, the cross-ratio of the four planes is

$$cr(\lambda_1,\lambda_2,\lambda_3,\lambda_4) = cr(0.01,0.05,0.11,0.20) = 1.3158. \tag{4.14}$$

A similar calculation with Equation 4.12 results in the same cross-ratio. Two remarks must be made to complete this argument. The points $\mathbf{P}_{i,wcs}$ were arbitrarily choosen to lie in a plane at z=100 (laser coordinate system). If the points were originally not on this plane, they could easily be projected onto this plane. Secondly, holding the left-right mirror constant does not generate a straight line on the plane z=100, but these points are easily projected onto a straight line in the plane, z=100. Thus the up-down scanning mirror preserves cross-ratios.

#### 4.4.3.9 Cross Ratio of the Left-Right Mirror

The SLDV left-right scanning mirror also preserves cross-ratios. If the up-down mirror is held in a constant position (constant mirror voltage), then the cross ratio of the slopes of the left-right mirror planes, as these planes intersect specific points, are the same as the cross-ratio of the four points, Figure 4.10. Choosing $A, B, C,$ and$D$ to have coordinates on a line in laser coordinate system, then cross-ratio, $cr(A,B,C,D)$, is found using Equation 4.9. For example, let $P_1 = (1,20,100), P_2 = (5,20,100), P_3 = (11,20,100),$ and$P_4 = (20,20,100)$, then the cross-ratio cr($P_1,P_2,P_3,P_4$) is 1.3158. From Equation 4.3 the slopes of the left-right mirror planes containing the laser beam are

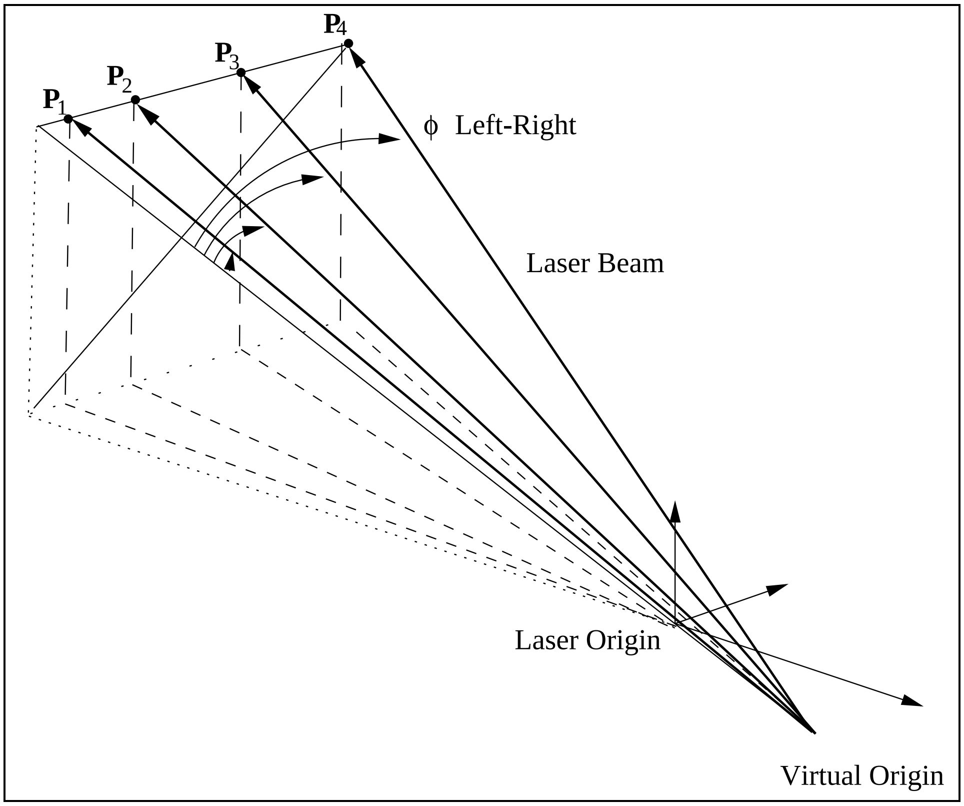

Figure 4.10: Cross-Ratio of Left-Right Mirror Angles

$$\lambda_i = \frac{P_{x_i,lcs}}{\sqrt{P^2_{y_i,lcs} + P^2_{z_i,lcs}} + \text{mirror offset}}. \tag{4.15}$$

Using these slopes, the cross-ratio of the four planes is

$$cr(\lambda_1, \lambda_2, \lambda_3, \lambda_4) = cr(0.4982, 2.4911, 5.4805, 9.9645) = 1.3158. \tag{4.16}$$

As above, Equation 4.12 may be used to calculate the same cross-ratio with appropriate angles. One remark must be made. The points $\mathbf{P}_{i,lcs}$ were arbitrarily choosen to lie in a plane at z=100. If the points were originally not on this plane, they could easily be projected onto this plane, specifically onto the line generated by holding the up-down mirror constant. Thus the left-right scanning mirror also preserves cross-ratios. The groundwork is now in place to see the velocity images of circular features in a new perspective.

### 4.4.4 SLDV Imaging of the Coordinate Calibration Model

The accurate, precise, and automatic determination of the SLDV's extrinsic parameters requires the integration of Lindholms's pose algorithm[33] and Fallon's computer vision techniques[15]. Lindholm's pose procedure requires the most accurate and precise object and image coordinates (mirror angle voltages) of corresponding points. Fallon's automated algorithm determines image points from images of known circular features. Since Fallon's procedure is crucial to improving the quality of input data for Lindholms's pose algorithm, this procedure is described in the next section.

#### 4.4.4.1 Fallon's Automated Pose Procedure

Fallon's automated pose procedure uses a calibrated CCD camera to image known, circular features and infer the camera's extrinsic parameters. This procedure consists of four steps. The first step is to image the known circular features, e.g. steam tubes. The images of circles are ellipses since the (pin-hole) camera applies a perspective transformation to the circles. The next step is to construct bitangents among the ellipses. The intersection of the joins of matched tangent points are points, which are the images of the circle centers. Thus the known coordinates of the circle centers may be paired with the corresponding image points. Knowing the camera's intrinsic parameters, the extrinsic parameters may be determined. The modifications to this procedure for the SLDV are described in the next section.

#### 4.4.4.2 SLDV Automated Pose Procedure

The SLDV automated pose procedure follows the same essential steps as Fallon's algorithm. The first step is to image known circular features with the SLDV. Small speakers mounted behind the washers on the coordinate calibration object are used so that the SLDV is able to "see" the circular features. A velocity image of the calibration object may be seen in Figure 4.11. The image of these circles are ellipses because the SLDV preserves cross-ratios; the SLDV is a projective camera. This time a projective transformation has been applied to the circles resulting in ellipses. As above, the bitangents among the image ellipses are constructed and the bitangent image points found. (Essentially this SLDV automation procedure exploits the fact that collineations are preserved under projective transformations.) This image data set is exactly what Lindholm's algorithm needs as input data. Thus the pose of the SLDV may now be determined. The practical implementation of this procedure to achieve one DAC step resolution in the image coordinates is described below.

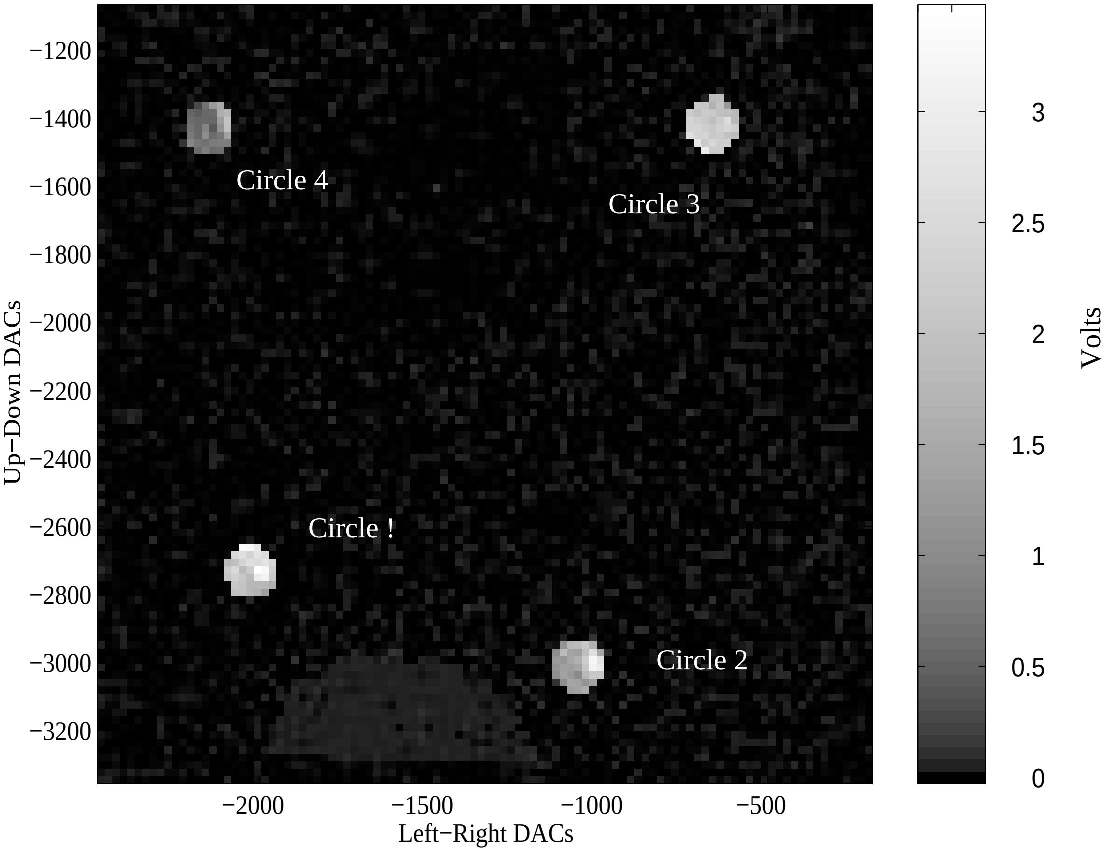

**Figure 4.11: Low Resolution Velocity Image of Calibration Object**

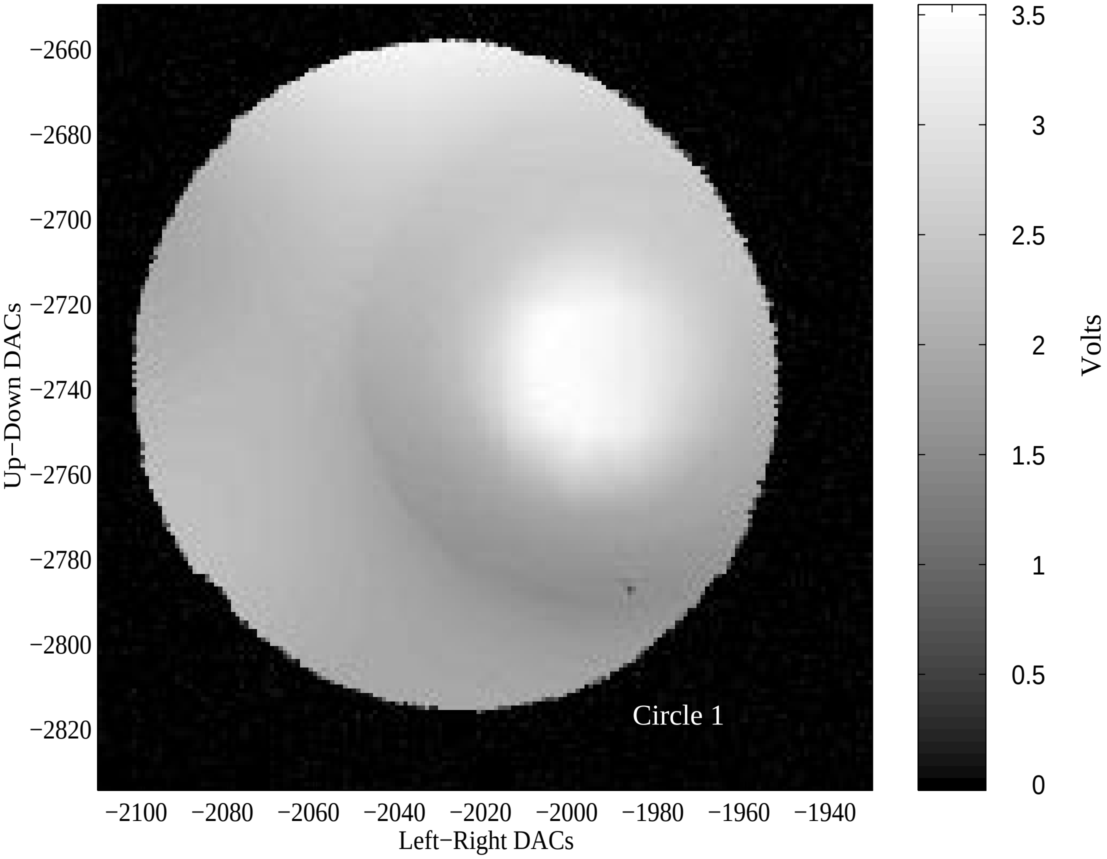

**Figure 4.12: High Resolution Velocity Image of Speaker 1**

## 4.5 Implementation

The algorithmic implementation of the automated SLDV pose procedure consists of a velocity image processing procedure and a series of experiments. The image processing procedure will generate accurate and precise image points for Lindholm's SLDV pose algorithm. The experiments will validate and quantify the experimental repeatability and accuracy of the automated SLDV pose procedure. The image processing will be described first followed by the experiments.

### 4.5.1 Velocity Image Processing

The velocity image processing is a multi-step procedure which results in image points with better than one DAC step resolution. Figure 4.11 shows a 104x104 velocity image of the coordinate calibration object with limited pixel resolution, i.e. the row, column spacing is not simple DAC steps. Figure 4.12 is a velocity image of one speaker at full pixel resolution. This 180x185 image contains 33,330 pixels and requires approximately ninety minutes to acquire. This full, two-dimensional imaging approach to detecting the four conic features would require more than four hours to complete, far too long to be practical. An alternate approach is necessary so that the one-pixel resolution is achieved in a timely manner.

### 4.5.2 Bitangent Point Feature Reconstruction

The recovery of the bitangent image points which correspond to the calibration object's bitangent points is predicated on reconstruction of the conic images of the calibration object's circular features. The implemented algorithm for recovering the calibration object's circular features in the velocity image is a coarse/fine approach.

The coarse estimation of the conic image features is a three step procedure. First the SLDV user directs the laser beam to the approximate center of each calibration object speaker and places these four DAC step coordinates into a file. This file is read into a MATLAB routine which generates a scanlist file. This scanlist file contains the DAC step coordinates to simply scan three lines, 300 contiguous pixels each, across each circular feature. The raw data from this scanlist in shown in Figure 4.13. A closer view of conic 1 is depicted in Figure 4.14. The idea here is to detect the ellipse edges and regress the coefficients of a general conic from the edge points. The noisy nature of the raw velocity

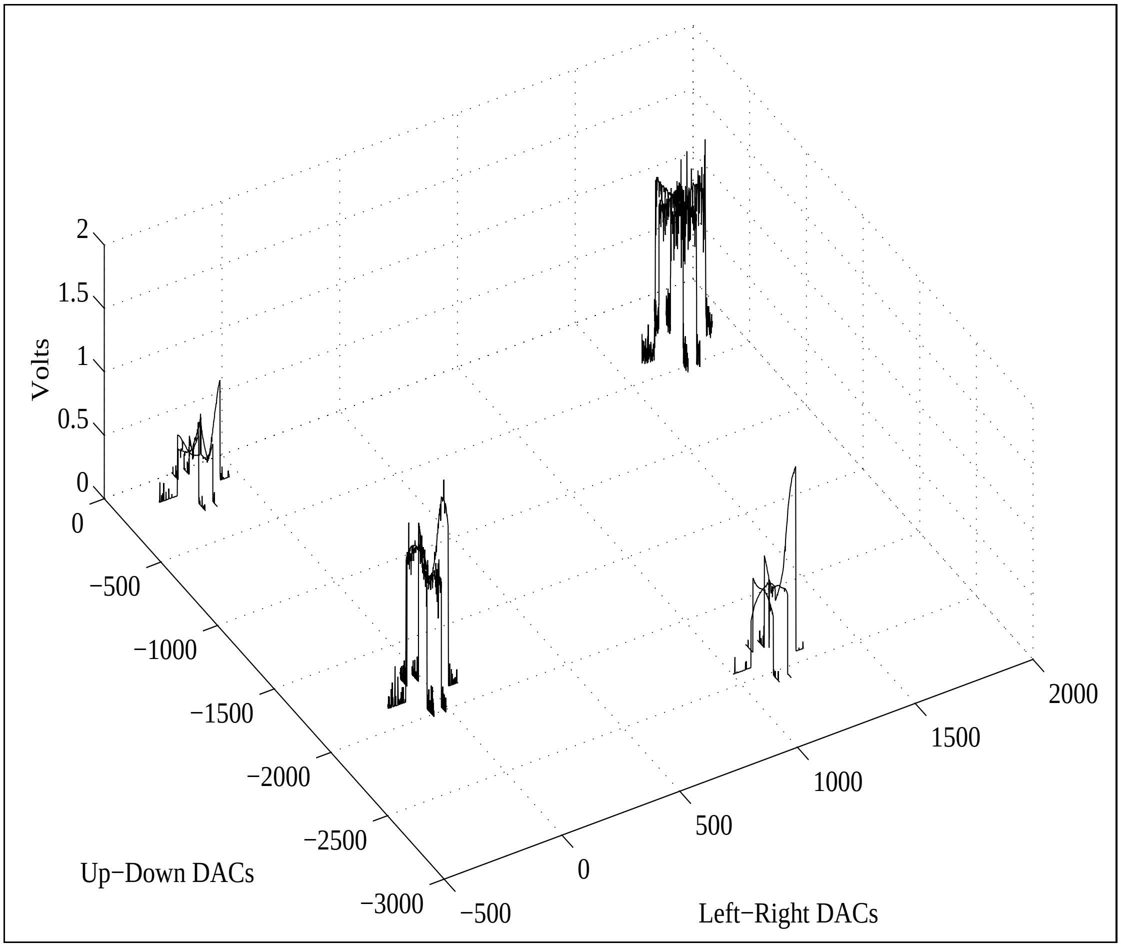

**Figure 4.13: Raw Velocity Scans : Three Lines per Conic**

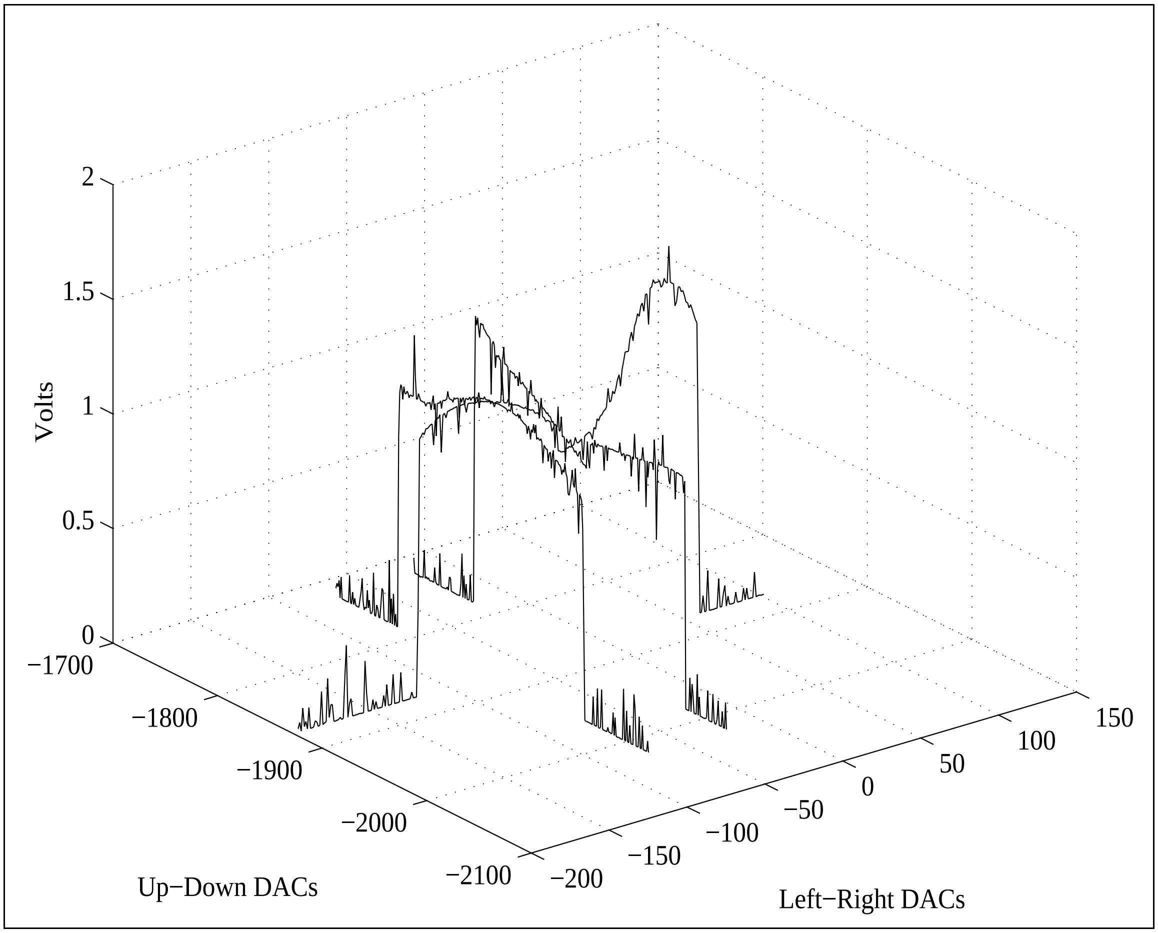

Figure 4.14: Three Velocity Lines Across Conic 1

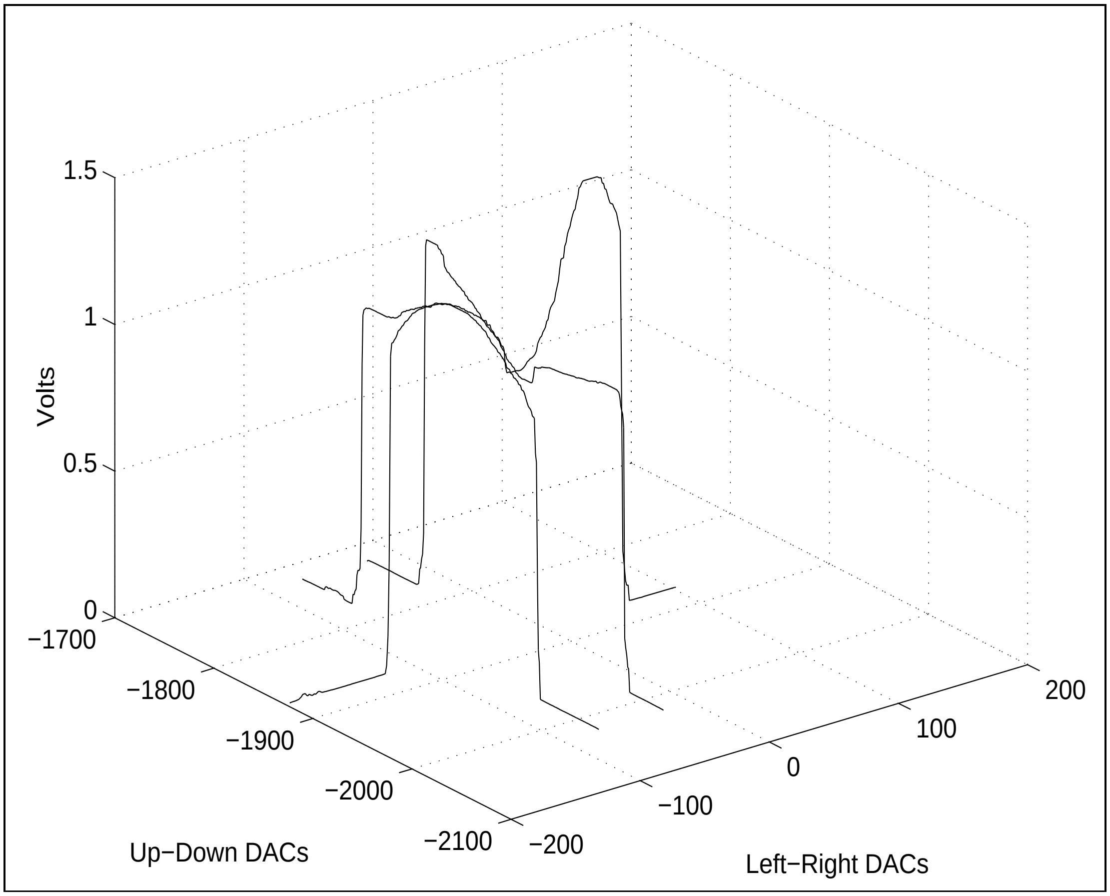

**Figure 4.15: Median Filtered Velocity Lines Across Conic 1**

data is clear and presents a problem to reliably detect the correct edge. To address the noise, the velocity data is median filtered with a 25 pixel window. The output of the procedure is shown in Figure 4.15. This filtered velocity data has clear edge features which may be recovered with a simple gradient, edge detection algorithm, see Figure 4.16. Another view of the detected points may be seen in Figure 4.17 The coordinates of the six edge points may be used to regress the conic coefficints of each ellipse. Specifically the general equation of a conic is

$$Ax^2 + By^2 + Cxy + Dx + Ey + F = 0 \tag{4.17}$$

Letting F = 1, each edge point $(x_i, y_i)$ is an estimate of the ellipse,

$$\begin{array}{llllll} -1 & = Ax_1^2 & +By_1^2 & +Cx_1y_1 & +Dx_1 & +Ey_1 \\ -1 & = Ax_2^2 & +By_2^2 & +Cx_2y_2 & +Dx_2 & +Ey_2 \\ \vdots & \vdots & \vdots & \vdots & \vdots & \vdots \\ -1 & = Ax_n^2 & +By_n^2 & +Cx_ny_n & +Dx_n & +Ey_n \end{array} . \tag{4.18}$$

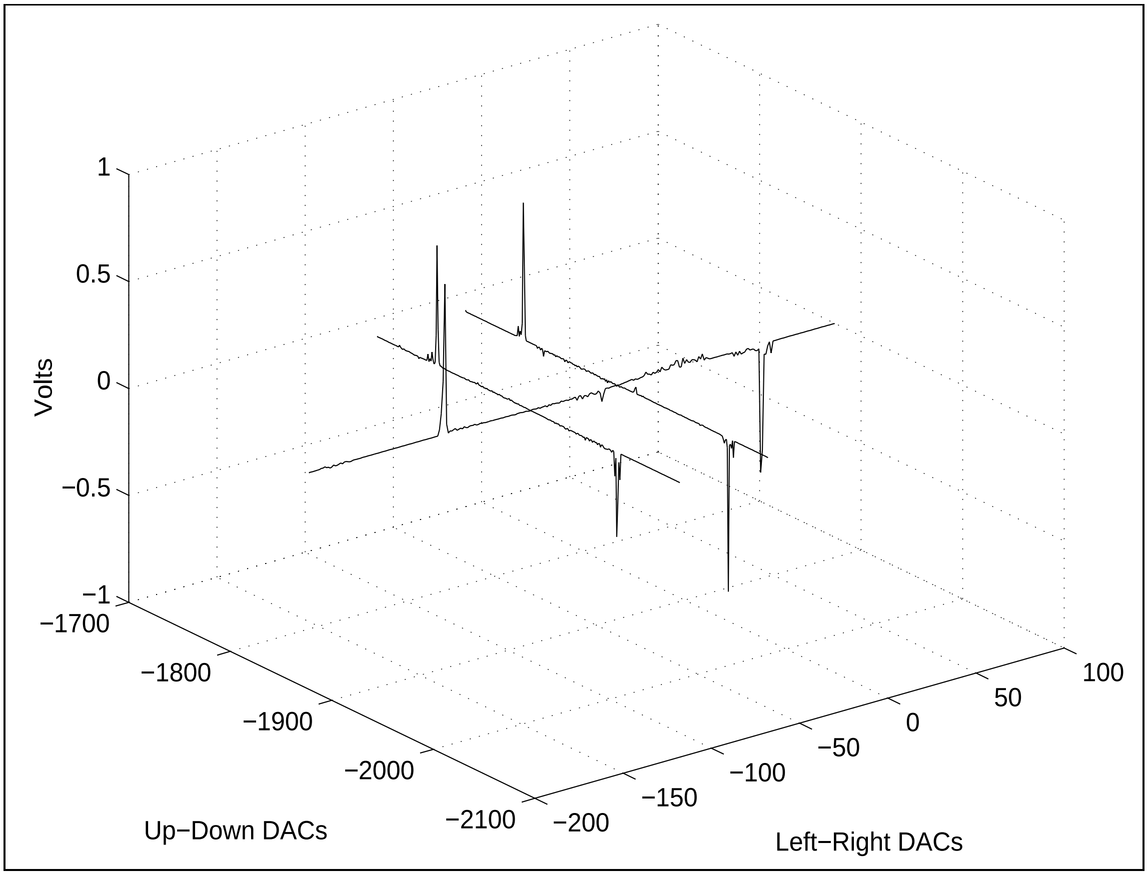

**Figure 4.16: Gradient of Filtered Velocity Data Across Conic 1**

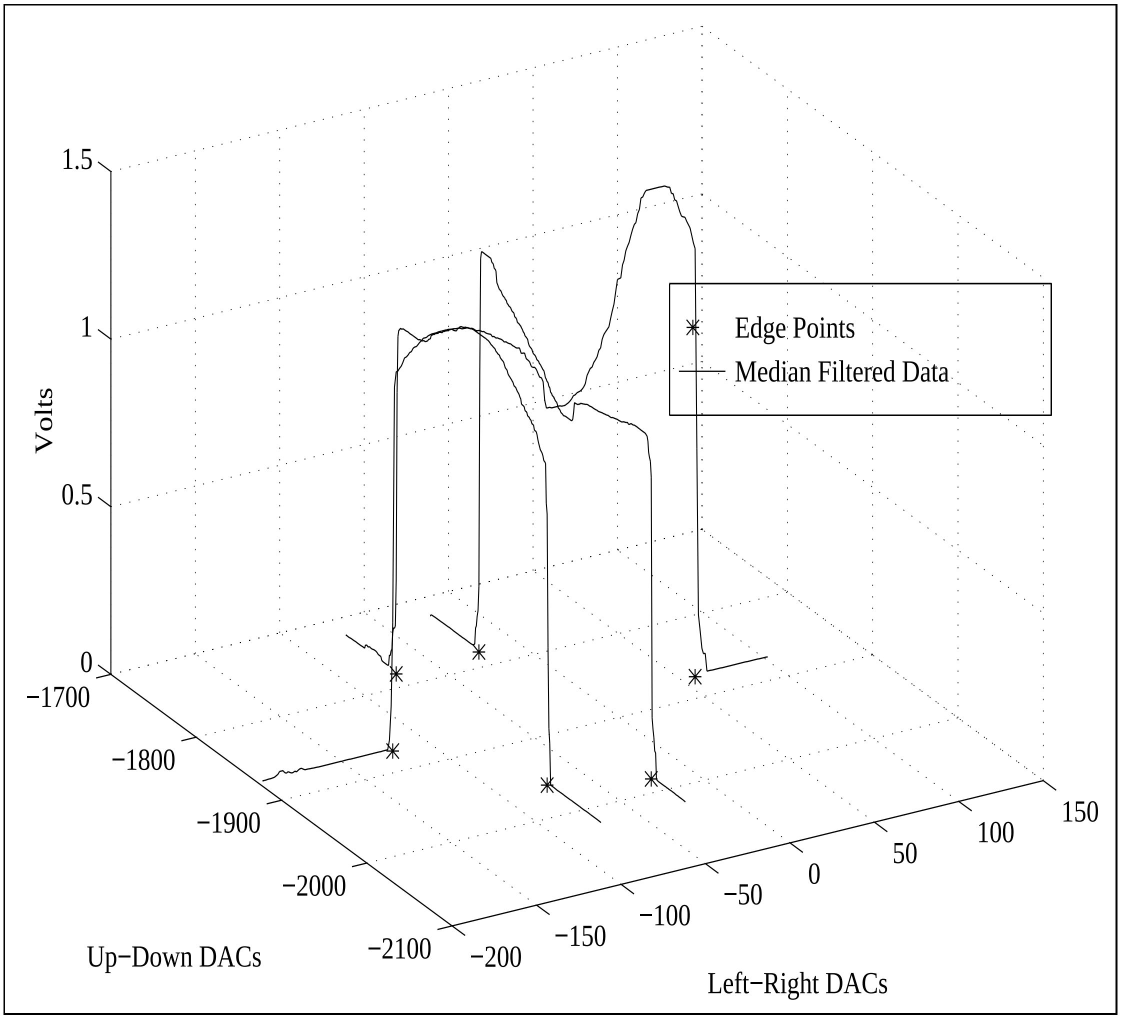

Figure 4.17: Edge Detection of Filtered Velocity Data Across Conic 1

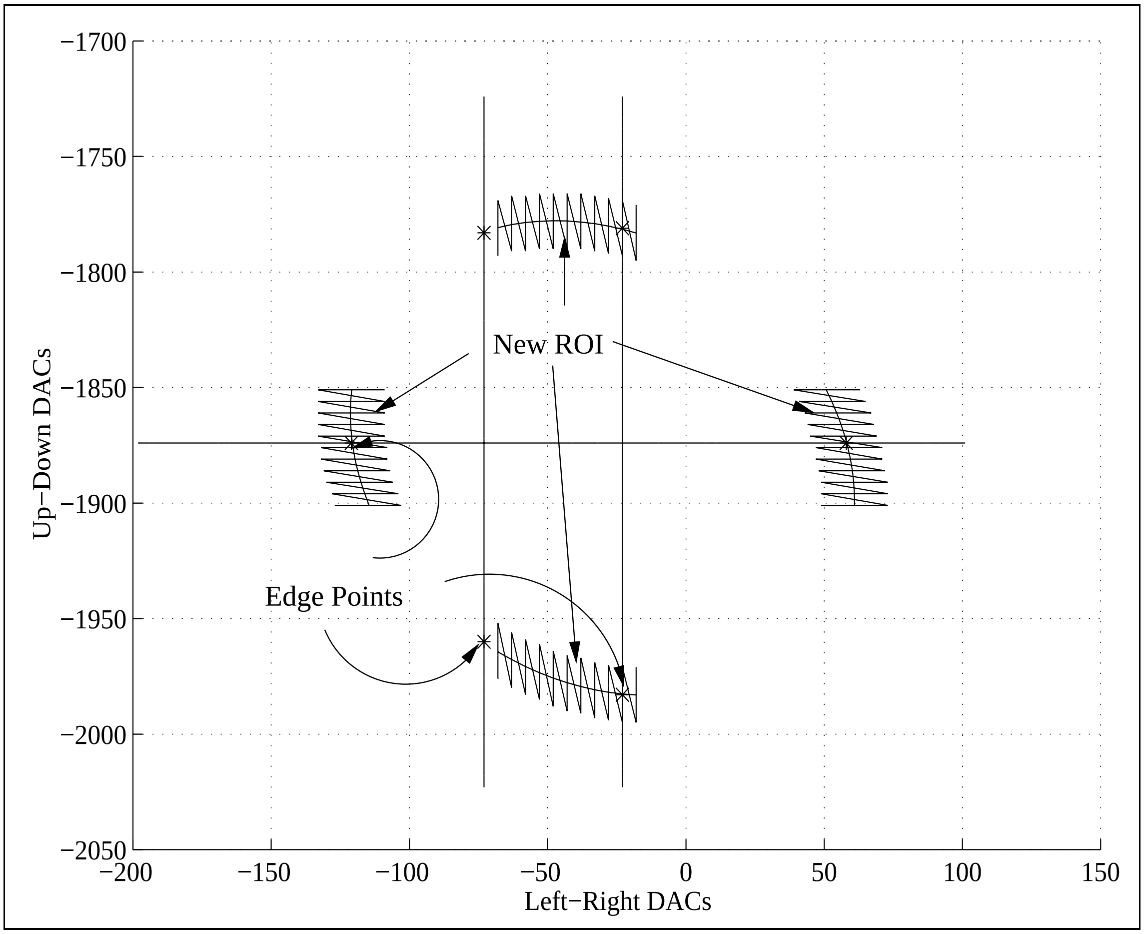

**Figure 4.18: Fine ROI Definition for Conic 1**

The conic coefficients are determined by rewriting these equation in matrix form and solving with the least square's technique, i.e.

$$\left\{\begin{array}{c} -1 \\ -1 \\ \vdots \\ -1 \end{array}\right\} = \left[\begin{array}{ccccc} x_1^2 & y_1^2 & x_1y_1 & x_1 & y_1 \\ x_2^2 & y_2^2 & x_2y_2 & x_2 & y_2 \\ \vdots & \vdots & \vdots & \vdots & \vdots \\ x_n^2 & y_n^2 & x_ny_n & x_n & y_n \end{array}\right] \left\{\begin{array}{c} A \\ B \\ C \\ D \\ E \end{array}\right\}, \tag{4.19}$$

$$\{O_{nes}\} = [D_{ata}]\{C_{oefficints}\}, \tag{4.20}$$

$$\left[[D_{ata}]^T[D_{ata}]\right]^{-1}[D_{ata}]^T\{O_{nes}\} = \{C_{oefficients}\}. \tag{4.21}$$

This intial estimate may be used to define a new ROI to scan. This concludes the coarse

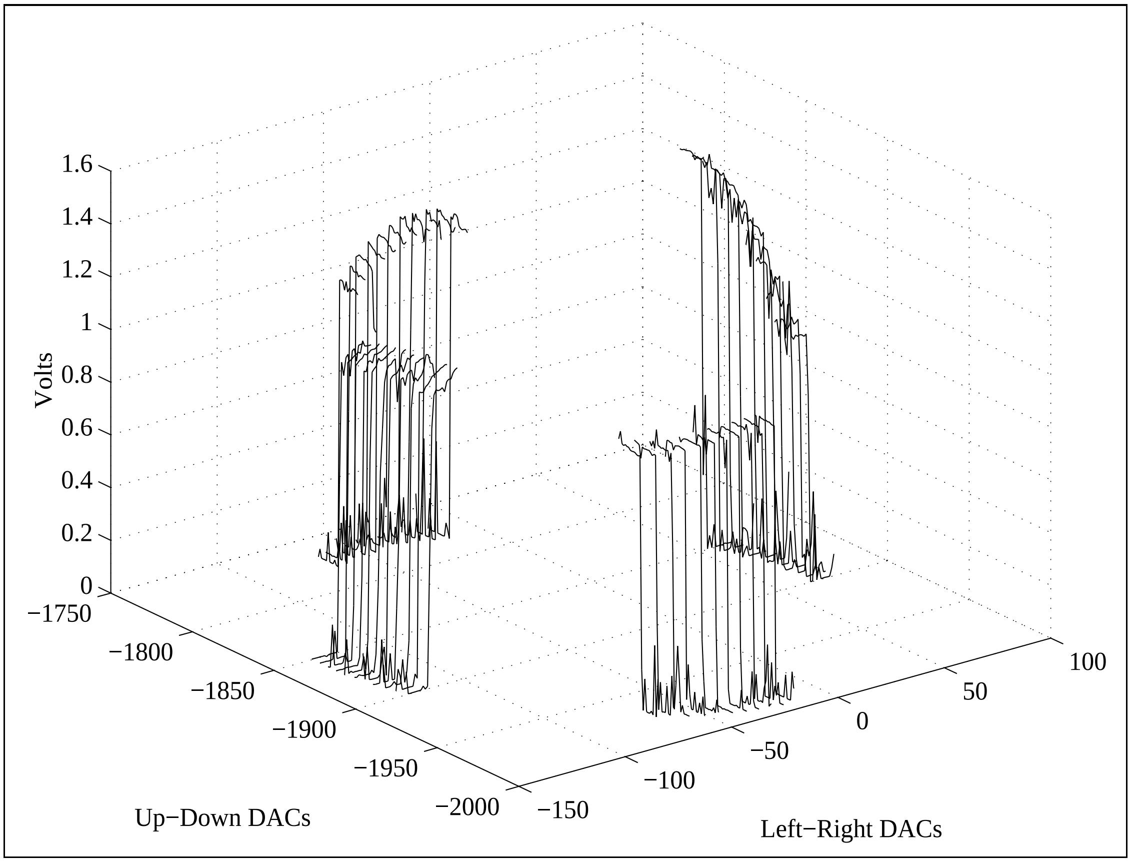

**Figure 4.19: Raw Velocity Data, Fine Procedure**

ellipse estimate.

The coarse conic coefficients are used to develop a new scanlist which will provide more data for a refined estimate of the ellipse coefficients. Figure 4.18 shows the new regions of interest which consist of 44 lines of 25 pixels length for each circular object features. The goal here is to get as many edge points as possible within a reasonable time frame. The image processing remains the same. Figure 4.19 is the raw velocity data. Figure 4.20 is the median filtered data with a five pixel window. The gradient is shown in Figure 4.21. The detected edge points are superimposed on the filtered velocity data and depicted in Figure 4.22. The fitted conic points and the original data for one ellipse are shown in Figure 4.23. The corresponding residuals of regressing the conic coefficients are shown in Figure 4.24. These figures are typical results of the fine, conic fitting procedure. The next step is the recovery of the bitangent points.

The recovery of the bitangent points between two ellipses may be done in several ways. One method is to directly solve for the intersection of the two ellipses. Two ellipses

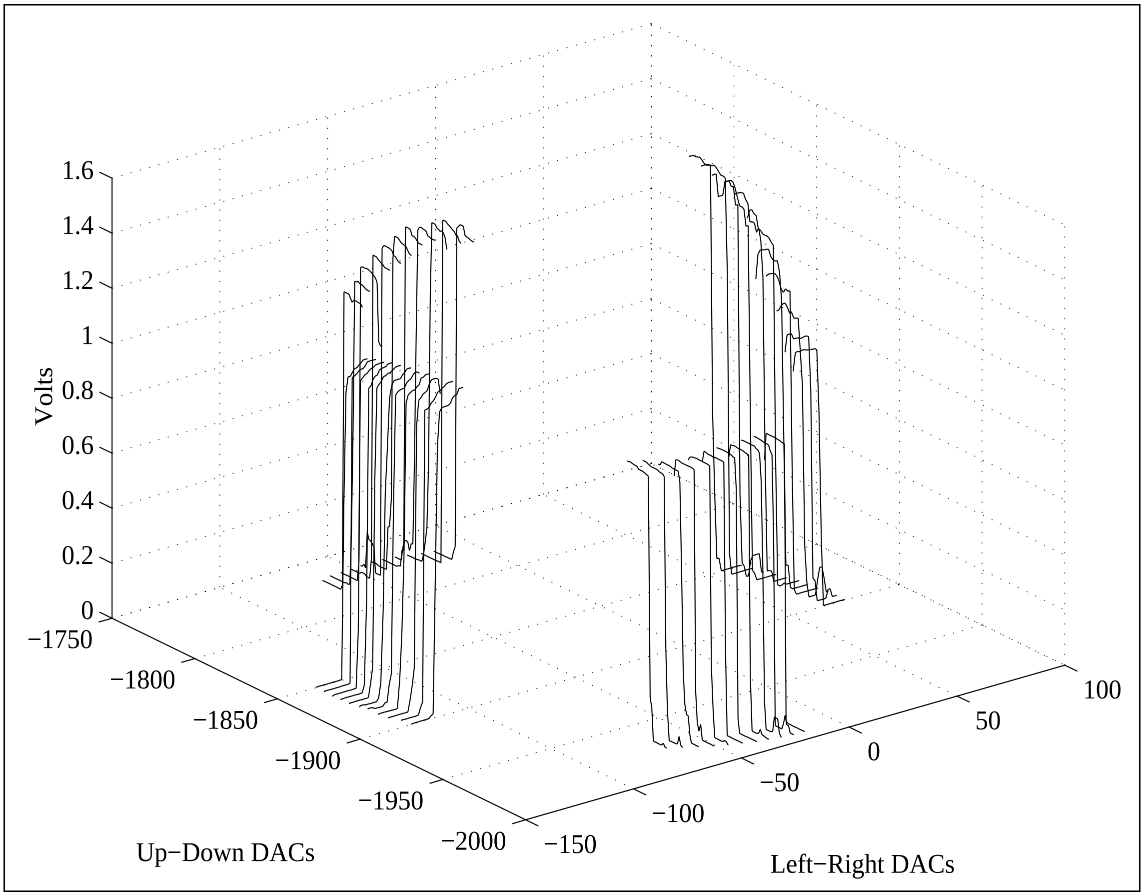

Figure 4.20: Median Filtered Velocity Data, Fine Procedure

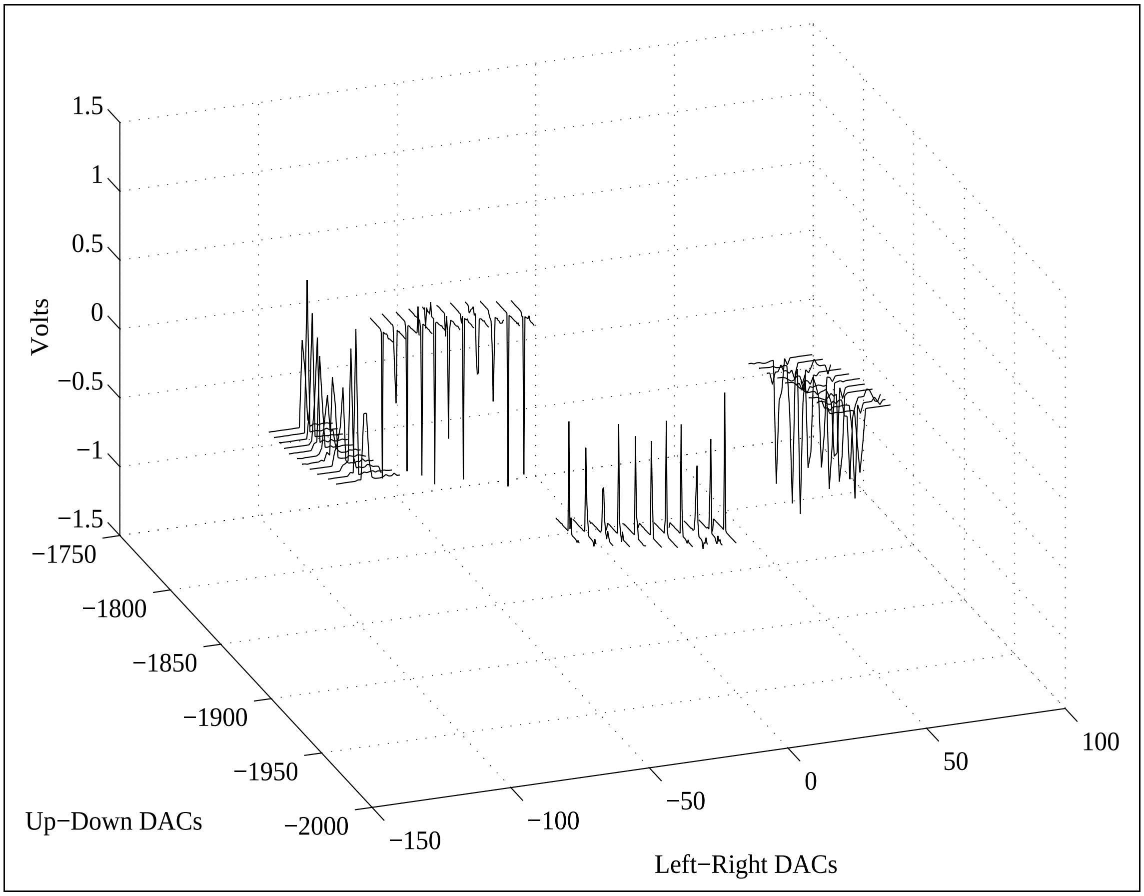

Figure 4.21: Gradient Velocity Data, Fine Procedure

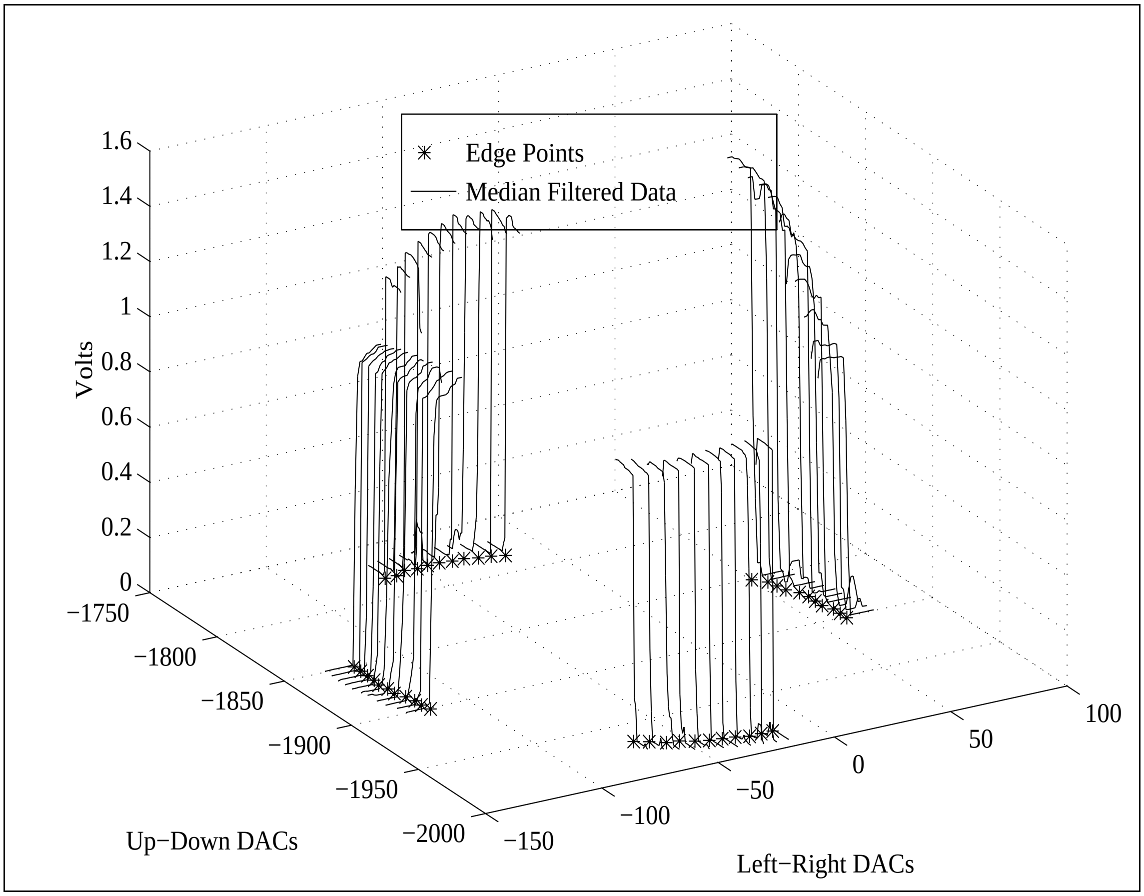

Figure 4.22: Edge Detection in Velocity Data, Fine Procedure

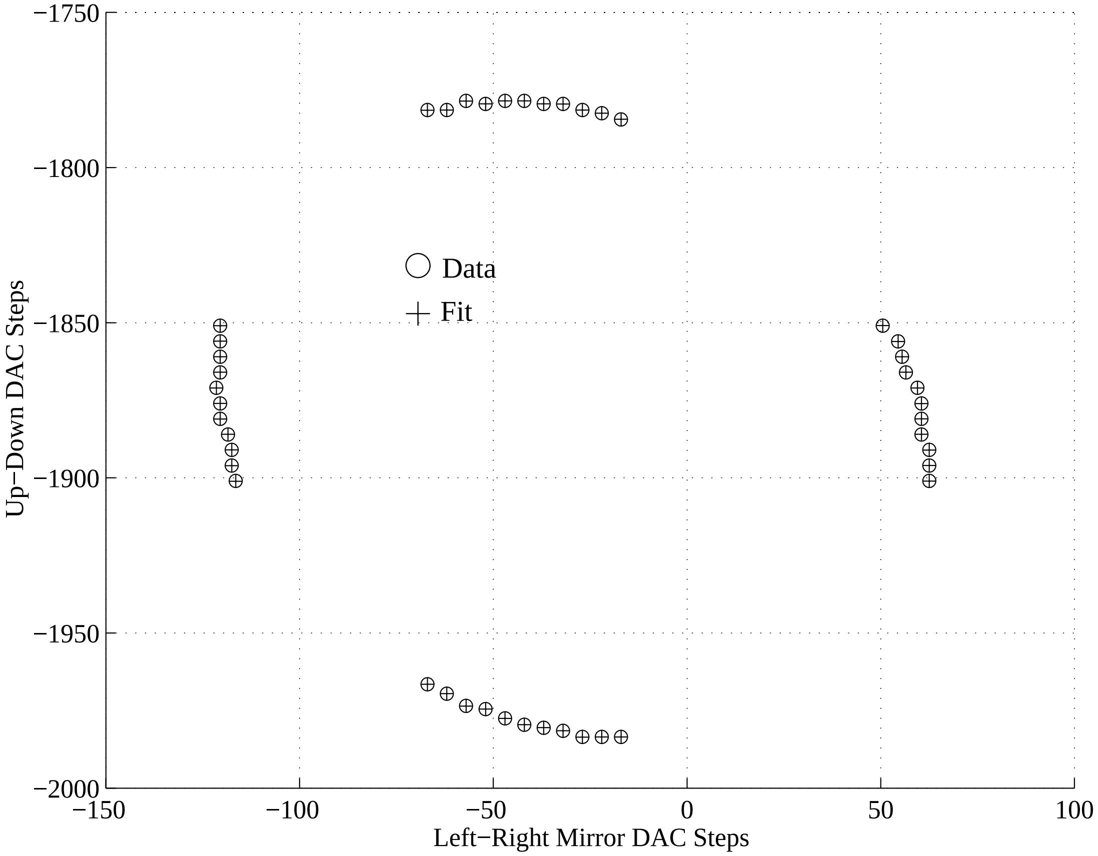

Figure 4.23: Results of Conic Regression, Fine Procedure

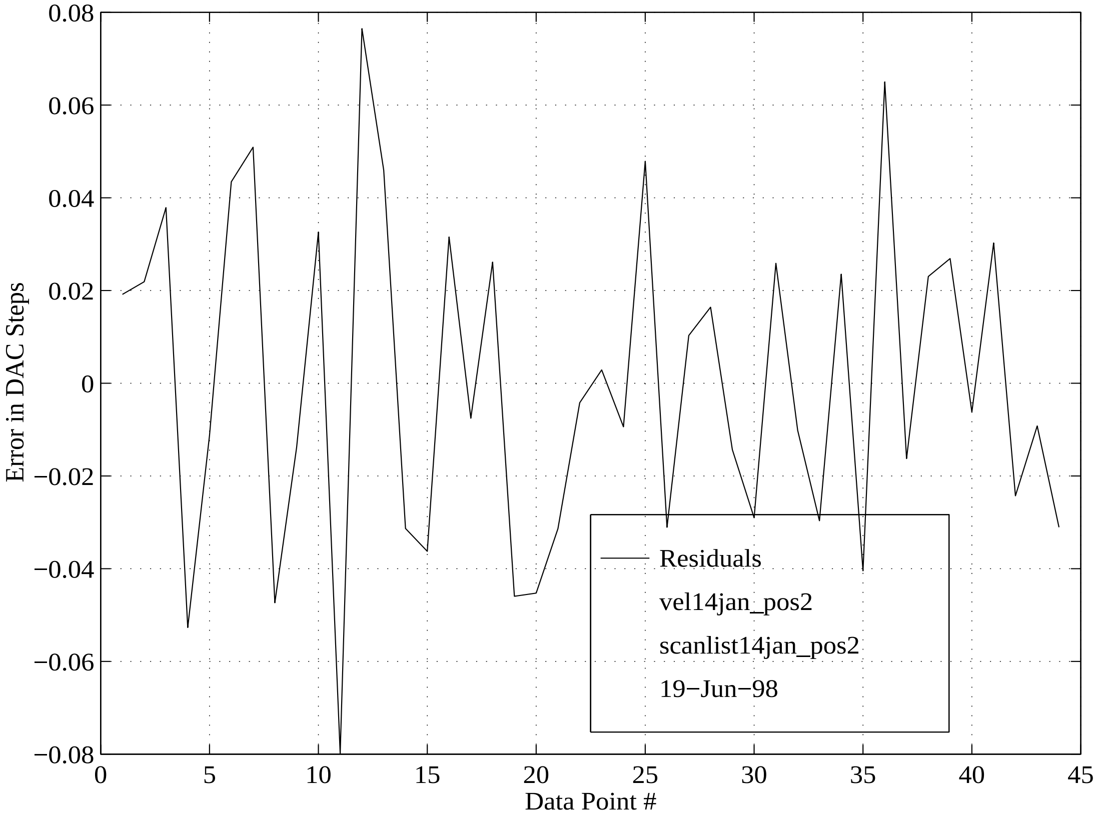

**Figure 4.24: Residuals of Conic Regression, Fine Procedure**

intersect in four points, although the points may be imaginary. If the two ellipses are viewed as line conics, then the four intersecting "points" are lines and are easier to visualize. Once the intersecting elements are in hand, the bitangent points are directly calculated[15, 48, 3]. Following this procedure, the regressed conic coefficients for the point-wise conic in matrix form is

$$x_{image}^T \begin{bmatrix} A & C/2 & D/2 \\ C/2 & B & E/2 \\ D/2 & E/2 & F \end{bmatrix} x_{image} = x^T [C] x = 0. \tag{4.22}$$

Here $x_{image}$ are homogenous points. The line-wise matrix form is

$$X_{image}^T \begin{bmatrix} A & C/2 & D/2 \\ C/2 & B & E/2 \\ D/2 & E/2 & F \end{bmatrix}^{-1} X_{image} = X^T [C]^{-1} X = 0. \tag{4.23}$$

The homogenous lines are $X_{image}$. With these line-conic coefficients, the intersection lines between pairs of conics are found using MATLAB's symbolic and root solving routines. Once the intersection lines(X) are found, the bitangent points may be calculated by

$$X_i^T [C_j]^{-1} = x_i, \tag{4.24}$$

where $X_i$ are the intersection lines between a pair of conics, $[C_j]^{-1}, j = 1, 2$ are the line-wise coefficients of the two conics, and $x_i$ are the bitangent points. This completes the recovery of the bitangent points for one conic pair. The process is repeated for each conic pair. This produces 48 bitangent points of which 16 are selected which correspond to the bitangent points back in Figure 4.1. The pose input data of object points and image points is now complete. Next, the experimental verification of repeatability, precision and accuracy of the SLDV pose must be addressed.

## 4.6 Experimental Verification

The experimental verification of the SLDV pose automation process consists of three steps: repeatability of recovering the bitangent points in the velocity image; estimation of the pose accuracy and precision; and an independent evaluation of the SLDV pose accuracy. Finally, a comparison among three different pose approaches will show the improvement that automation brings to the SLDV pose process.

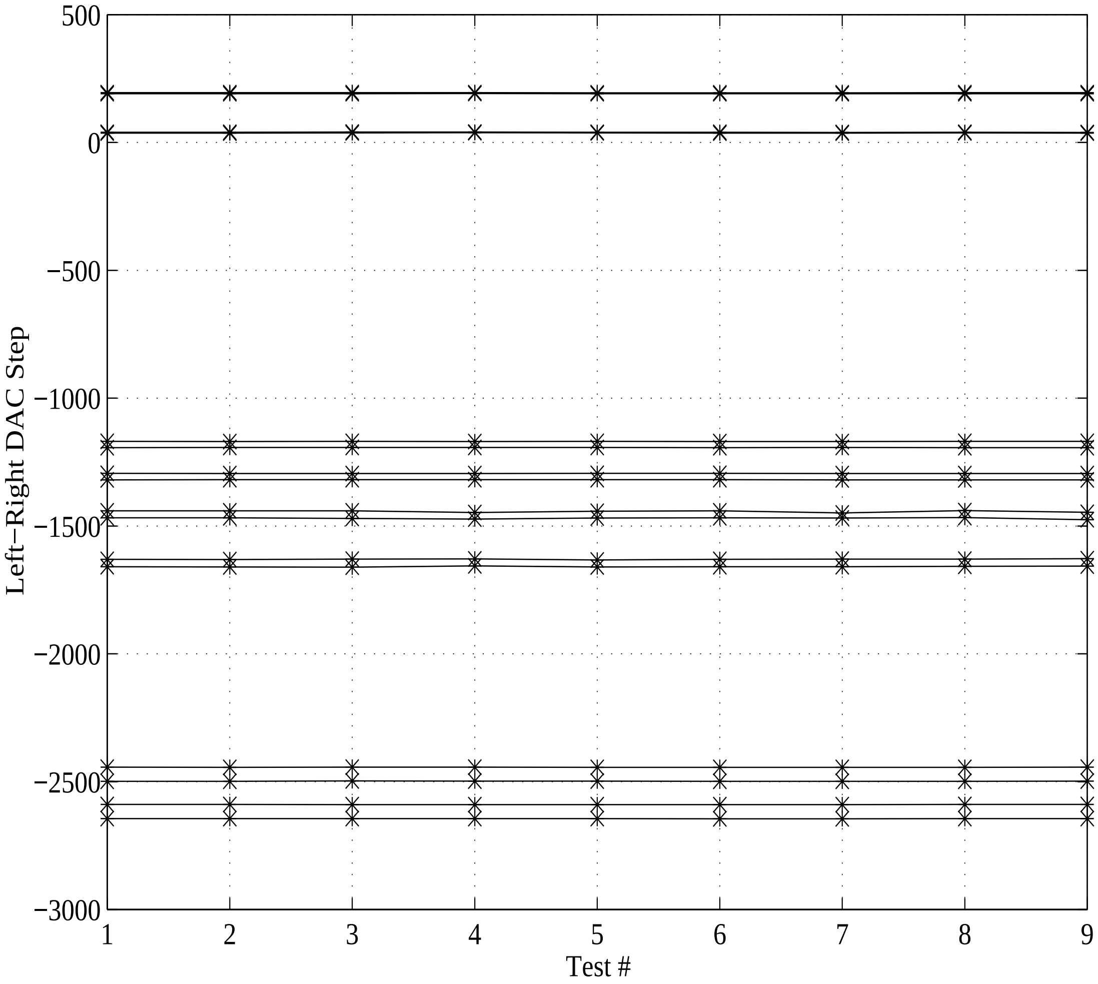

**Figure 4.25: Left-Right Bitangent Points**

### 4.6.1 SLDV Pose Repeatability

The repeatability of the SLDV pose automation process to recover the "same" bitangent points is the subject of the first experiment. The SLDV is arranged so that the calibration object is within the SLDV's viewing volume. The SLVD pose automation process is performed nine times to recover nine sets of bitangent point data. The data sets are presented in Figures 4.25 and 4.26. The standard deviation of the repeatability of each point is less than $\frac{1}{2}$ DAC step, except for points in ellipse three. These results are graphically presented in Figure 4.27. The four points with the higher standard deviation represent the ellipse which happens to be at the SLDV's "non-optimum" optical working distances [43]. Thus if care is taken when placing the SLDV, then $\frac{1}{2}$ DAC step repeatability is attainable. This repeatability is necessary to achieve precise and accurate poses.

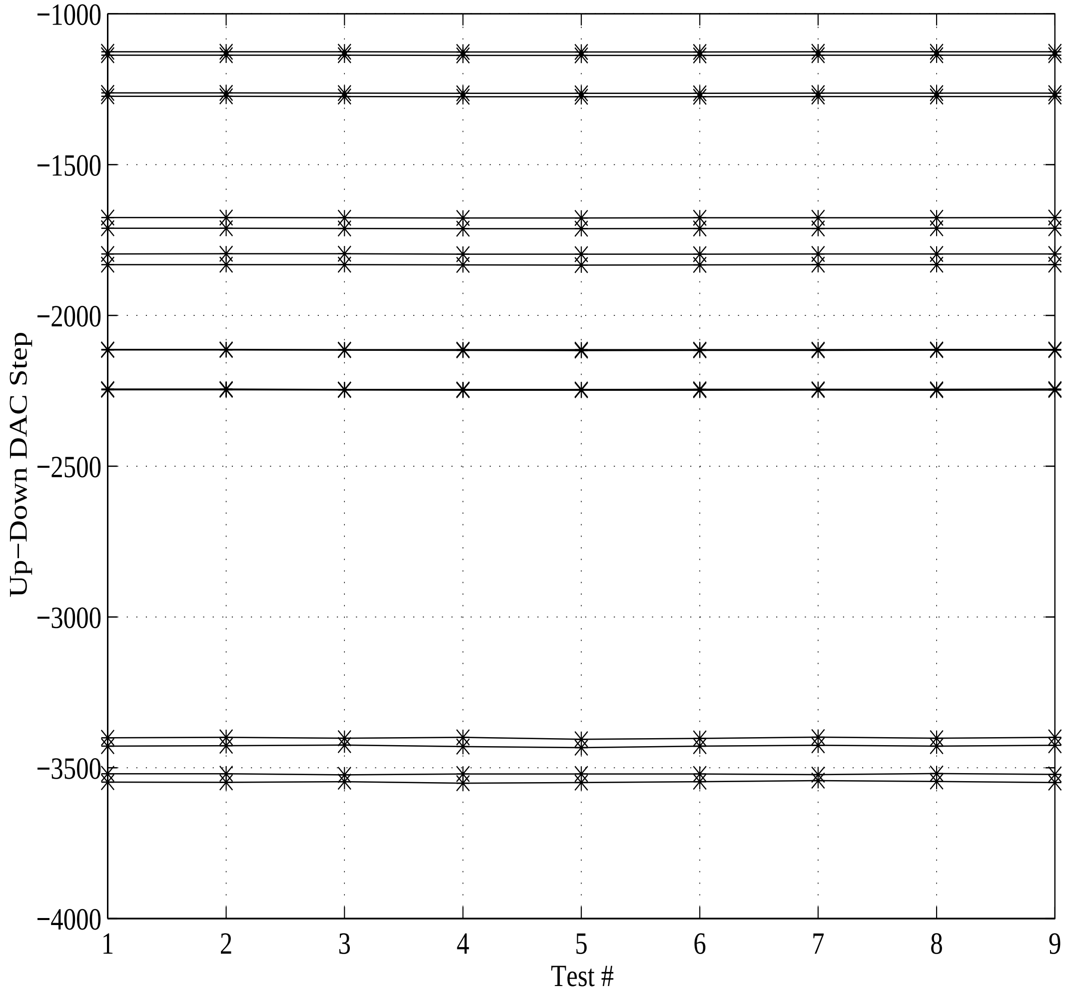

Figure 4.26: Up-Down Bitangent Points

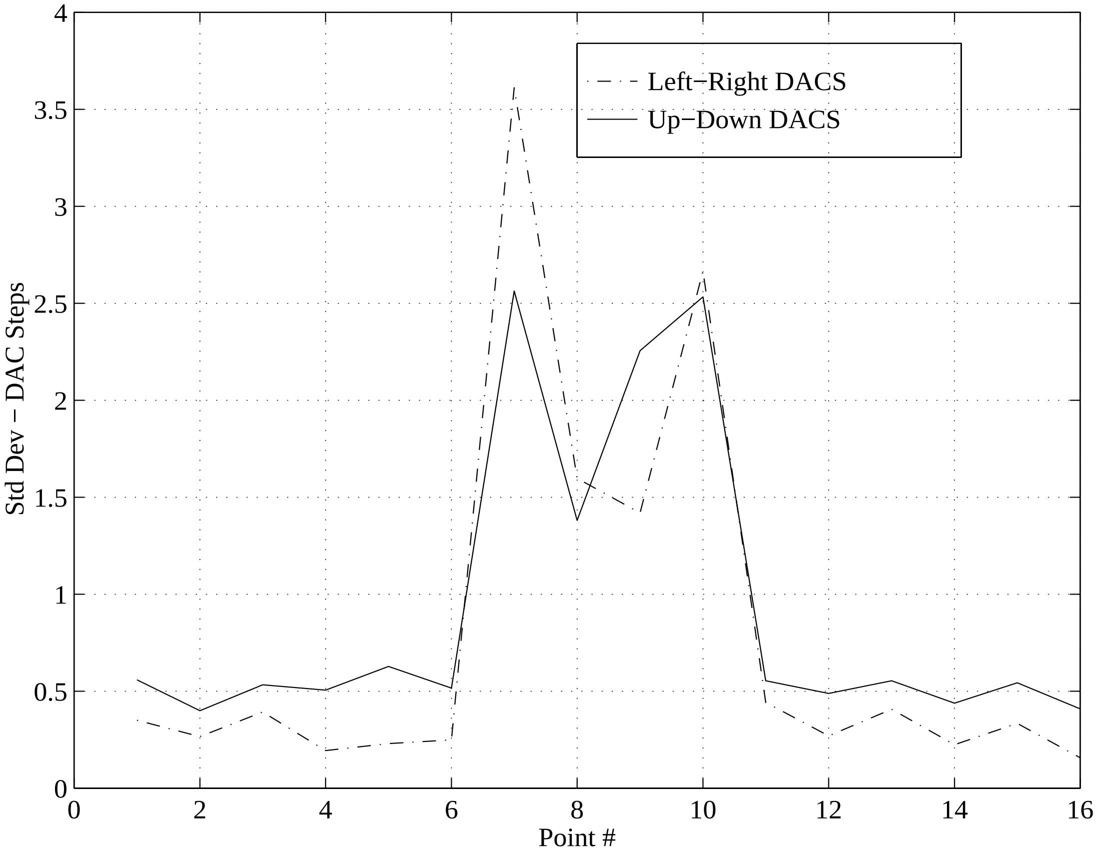

Figure 4.27: Standard Deviation of Bitangent Points

```
NUMREG 16
UNITS inch
DISTGUESS  67
REGPOINT   1   2.3490   3.2156  0.000     5.7240e+00   1.6338e-02
REGPOINT   2   2.1653   2.4277  0.000     6.3252e+00   1.5252e-01
REGPOINT   3   7.5578   2.0048  0.000     7.5321e+00  -3.68404e+00
REGPOINT   4   7.3725   1.2100  0.000     8.1404e+00  -3.5342e+00
REGPOINT   5   7.0696   1.7066  0.000     7.6883e+00  -3.32194e+00
REGPOINT   6   7.8611   1.5078  0.000     7.9869e+00  -3.8966e+00
REGPOINT   7   9.1017   9.8073  0.000     1.1459e+00  -5.0806e+00
REGPOINT   8   9.8976   9.6075  0.000     1.4373e+00  -5.7101e+00
REGPOINT   9   9.5079   9.2973  0.000     1.6583e+00  -5.3927e+00
REGPOINT   10  9.4905  10.1177  0.000     9.2188e-01  -5.3952e+00
REGPOINT   11  1.5890   9.1396  0.000     8.2673e-01   5.0844e-01
REGPOINT   12  1.5721   9.9408  0.000     1.5990e-01   5.2678e-01
REGPOINT   13  1.9797   9.5806  0.000     5.1099e-01   2.3635e-01
REGPOINT   14  1.1823   9.5003  0.000     4.7595e-01   7.9599e-01
REGPOINT   15  2.6598   2.8623  0.000     6.0526e+00  -1.9674e-01
REGPOINT   16  1.8549   2.7813  0.000     5.9968e+00   3.6480e-01
```

**Figure 4.28: Pose Input File**

### 4.6.2 Accuracy and Precision of the Automated Pose Procedure

Once the bitangent points are in hand, the input file for Lindholm's non-linear pose algorithm is complete and the SLDV pose may be determined. Lindholm's algorithm estimates six parameters- three Euler angles[2, 21] and three translation parameters. The error bounds on these six parameters are also calculated. A typical input file is shown in Figure 4.28. Typical output from Lindholm's routine for the input file in Figure 4.28 is shown in Figure 4.29. Once the SLDV pose has been determined, the accuracy of this solution needs an independent verification which is supplied by an acoustic digitizer.

### 4.6.3 Independent Estimate of SLDV Pose

The accuracy of the automated pose algorithm is verified with data from an acoustic digitizer. The acoustic digitizer may be used to digitize three points on the calibration object and three points on a specifically fabricated SLDV stand[55]. When the digitzer is used, each sample is the average of four acoustic measurements. When digitizing each point, seven samples are acquired. (The three posts are located at known distances relative to the SLDV coordinate system[55].) Once these data are available, a complete calibration ob-

```
Registration data file name:  cmm_pos2.reg
cmmpos2.reg
SSE 0.00079, s^2 0.0000, s (deg) 0.0055, s (DAC steps) 0.9039
Parameters - radians and meters
  phi1  = -1.153 +- 0.004
  phi2  =  2.547 +- 0.002
  phi3  =  1.913 +- 0.004
  x0_x  =  0.862 +- 0.003
  x0_y  =  0.508 +- 0.004
  x0_z  =  1.553 +- 0.003
```

**Figure 4.29: Pose Output File**

```
Parameters - radians and meters
  phi1  = -1.149 +- 0.068
  phi2  =  2.545 +- 0.041
  phi3  =  1.928 +- 0.072
  x0_x  =  0.871 +- 0.036
  x0_y  =  0.489 +- 0.032
  x0_z  =  1.554 +- 0.010
```

**Figure 4.30: Digitizer Output**

ject to SLDV pose determination is possible. A typical pose estimate from this procedure for the same SLDV position above is shown in Figure 4.30. With estimates for the same parameters, statistical tests may used to determine if the parameters are the same. The basic hypothesis is that the difference between corresponding parameters is zero, under the normal statistical assumptions. The alternative hypothesis is that the parameters are not the same. Ott [44] summarizes this procedure:

$$H_o : \mu_1 - \mu_2 = 0 \tag{4.25}$$

$$H_a : \mu_1 - \mu_2 \neq 0 \tag{4.26}$$

$$\text{Reject } H_o \text{ if } \|t'\| > t_{\frac{\alpha}{2}} \tag{4.27}$$

$$\text{Test Statistic: } \|t'\| = \frac{\overline{y_1} - \overline{y_2}}{\sqrt{\frac{s_1^2}{n_1} + \frac{s_2^2}{n_2}}} \tag{4.28}$$

$$\text{degrees of freedom, df} = \frac{(n_1 - 1))(n_2 - 1)}{(n_2 - 1)c^2 + (1 - c)^2(n_1 - 1)} \tag{4.29}$$

**Table 4.2: Statistical Tests on Pose Parameters**

| | $\mu_1$ | $s_1$ | $n_1$ | $\mu_2$ | $s_2$ | $n_2$ | df | $t\prime$ | $t_{\frac{\alpha}{2}}$ | Reject |
|---|---|---|---|---|---|---|---|---|---|---|
| $\phi_1$ | -1.076 | 0.0025 | 16 | -1.077 | 0.0632 | 7 | 6 | 0.0418 | 3.707 | NO |
| $\phi_2$ | 2.640 | 0.0015 | 16 | 2.639 | 0.0222 | 7 | 6 | 0.1546 | 3.707 | NO |
| $\phi_3$ | 2.003 | 0.0025 | 16 | 2.018 | 0.0586 | 7 | 6 | -0.6938 | 3.707 | NO |
| x | 0.688 | 0.0020 | 16 | 0.685 | 0.0243 | 7 | 6 | 0.3248 | 3.707 | NO |
| y | 0.510 | 0.0020 | 16 | 0.497 | 0.0214 | 7 | 6 | 1.6042 | 3.707 | NO |
| z | 1.619 | 0.0015 | 16 | 1.621 | 0.0059 | 7 | 6 | -0.8844 | 3.707 | NO |

**Table 4.3: Pose Method Comparison**

| Method | Digitizer | Experienced User | Automated |
|---|---|---|---|
| Mean Error (DACs) | 6.2935 | 0.9578 | 0.3842 |
| STD (DACs) | 3.5231 | 0.2504 | 0.0643 |

$$c = \frac{\frac{s_1^2}{n_1}}{\frac{s_1^2}{n_1} + \frac{s_2^2}{n_2}}. \tag{4.30}$$

Table 4.2 above summarizes the results of the statistical tests for one SLDV pose. Since the calculated $t$ value is less than the test statistic, the hypothesis cannot be rejected; the two pose estimates are statistically equivalent. The improvement of the automated SLDV pose procedure is clearly seen when compared with the previous SLDV pose procedures.

### 4.6.4 Comparison of SLDV Pose Procedures

The developed automated pose procedure is the superior approach of the three SLDV pose procedures that have been used to determine the SLDV's pose. The three approaches are (1) direct the SLDV laser to a point on the structure and measure object coordinates with acoustic digitizer, (2) an experienced user ”eyeballs” the hand-measured fiducial points, and (3) the automated procedure developed in this research. The three methods are compared by using the output from Lindholm's algorithm which provides an error estimate on the pose in terms of DAC steps. Table 4.3 shows the results. Clearly the automated procedure performs better than the other methods because the mean error and standard deviation are the smallest. Addtionally, the automated procedure may be directly extended to effectively utilize data from a 16 bit D/A board; the other procedures' *error* sources will remain even if 16bit data are available. With the automated procedure, the best SLDV pose estimate is attained and is available for further processing of the velocity images - velocity field reconstruction.

## 4.7 Summary

The research goals in this chapter are to automate the SLDV pose procedure, to eliminate the error from the human "eyeballing" and coordinates of the object points, to improve the precision and accuracy of the pose input data, and to attain a better SLDV pose estimate. The automation of the pose process began with the development of a projective camera model for the SLDV. This development lead to the formulation of a calibration object with features that were projectively invariant. These features can be processed in both the object and image spaces to recover a set of corresponding points which are the input data for previously developed pose algorithms. This input data set is a more precise and accurate representation of the image/object point pairs which results in better estimates of the SLDV pose. Accurate SLDV poses are necessary for processing the acquired velocity images to reconstruct the structure's velocity field.

# Chapter 5

# Velocity Reconstruction

Several field reconstruction formulations are possible with registered, velocity *images.* The key aspect of these formulations is the computer vision viewpoint which emphasizes the structure of the acquired data where one data pixel has neighboring data pixels. These reconstruction procedures have their origin in holographic interferometry of opaque bodies, but are extended in this research to the SLDV data sets. The advantages of these analytic procedures are illustrated by examining velocity reconstruction at a point on the structure's surface. If the surface geometry is known, the point domain is expanded to the structure's surface. If the experimental surface geometry is not precisely known, then the surface domain is extended to a family of surfaces in the neighborhood of the structure's surface. After a description of the mathematical structure of the velocity images, the velocity field, and the surface domains, the analytic procedures to recover the velocity field are presented. Next, experimental velocity images are used to reconstruct the velocity field to demonstrate the advantages of applying the holographic analysis techniques. Finally a discussion of the experimental results provides a new viewpoint for interpreting the regressed velocity coefficients.

## 5.1 Mathematical Structure of Velocity Images

This section describes the mathematical structure of multiple velocity images of a vibrating structure. First the structure of a single image is examined. Next, the structure of multiple velocity images is presented.

### 5.1.1 Structure of a Single Velocity Image

The SLDV images the velocity field of a harmonically excited structure. This imaging process produces several mappings which may be described by

$$\begin{tikzcd}
S_{structure}(\mathcal{R}^2) \arrow[r, "M"] \arrow[d, "T"] & V_{velocity}(\mathcal{C}^3) \arrow[d, "P"] \\
S_{SLDV}(\mathcal{R}^2) \arrow[r, "N"] & V_{measured}(\mathcal{C}^1)
\end{tikzcd} , \tag{5.1}$$

where $S_{structure}$ is the structure's surface, $S_{SLDV}$ is the SLDV's toroidal imaging surface , $V_{velocity}$ is the structure's velocity field, and $V_{measured}$ is the measured, line-of-sight velocity component. First, a one-to-one and onto mapping, $T$, exists between the structure's surface domain and the SLDV's imaging surface [50, 10]. Secondly, $S_{structure}$ is the domain for the three dimensional velocity field, $V_{velocity}$, and locally a one-to-one and onto mapping, $M$. The projection $P$ of $V_{velocity}$ is the SLDV velocity measurement, $V_{measured}$, whose domain is $S_{SLDV}$. The projection is onto but not one-to-one, i.e. there is not a unique inverse map, $P^{-1}$, from the measured velocity to the surface velocity field. This is easily seen by examining the dimensions (shown in parenthesis) of each velocity field; $V_{measured}(\mathcal{C}^1)$, dim = 2, is the projected image of $V_{velocity}(\mathcal{C}^3)$, dim = 6. In other words, a single velocity image does not contain enough information to recover the velocity field. Fortunately, multiple velocity images remedy this situation. These mappings are true for local, not global, surface patches on the structure, i.e. one may always choose a domain such that all these one-to-one and onto mappings hold.

### 5.1.2 Structure of Multiple Velocity Images

Multiple velocity images of the velocity field result in similar mapping structures for each imaging position. The structure of these imaging processes is shown below, with the map $M$ between $S_{structure}$and $V_{velocity}$ still implied,

$$\begin{tikzcd}
 & S_{SLDV_1} \arrow[r, "N_1"] & V_{meas_1} & \\
S_{structure} \arrow[ur, "T_1"] \arrow[r, "T_2"] \arrow[dr, "T_n"'] \arrow[d, phantom, "\vdots"] & S_{SLDV_2} \arrow[r, "N_2"] \arrow[d, phantom, "\vdots"] & V_{meas_2} \arrow[d, phantom, "\vdots"] & V_{velocity} \arrow[ul, "P_1"'] \arrow[l, "P_2"'] \arrow[dl, "P_n"] \arrow[d, phantom, "\vdots"] \\
\phantom{S} & S_{SLDV_n} \arrow[r, "N_n"] & V_{meas_n} & \phantom{V}
\end{tikzcd} . \tag{5.2}$$

Since multiple images of the velocity field are available, the velocity field can be reconstructed if the bases of $V_{meas_1}, V_{meas_2}, \ldots, V_{meas_n}$ span $V_{velocity}$. Physically, this means that at least three sufficiently different SLDV positions must be used to recover the velocity field. The simplest form of the velocity reconstruction process is the recovery of the velocity vector at a point on the structure's surface.

## 5.2 Velocity Reconstruction at a Surface Point

The recovery of the velocity vector at a point is dependent on multiple velocity images of the same area. Instead of trying to "hit" the same object point in space from several viewpoints, the same area is imaged. Once imaged, rays (laser beam) are cast from the object point back onto the image to obtain the measured velocity value. This raycasting is the map $T$. In this manner the image point of the surface point is located in the velocity image. Typically the image point is between sample pixels; the measured velocity values are interpolated from the surrounding pixel values. Similarly, the mirror angles are interpolated so that the direction cosines from the surface point to the SLDV image point are determined. Having found the image points and direction cosines, velocity reconstruction may proceed using several different methods, absolute, relative, or contravariant. Each method represents differing bases for recovering the velocity vector at the surface point.

### 5.2.1 Absolute Method

The "absolute" method is the simplest form of velocity reconstruction; the term "absolute" method is borrowed from holographic interferometry where the measured direction cosines form the basis vectors for the reconstruction of surface displacements[50]. Similary, the measured direction cosines, $D$, form the basis vectors for reconstruction of the velocity vector at a point. The velocity and direction cosines may be put in a matrix form

$$\begin{Bmatrix} v_1 \\ v_2 \\ v_3 \end{Bmatrix} = \begin{bmatrix} D_{11} & D_{12} & D_{13} \\ D_{21} & D_{22} & D_{23} \\ D_{31} & D_{32} & D_{33} \end{bmatrix} \begin{Bmatrix} V_x \\ V_y \\ V_z \end{Bmatrix}, \tag{5.3}$$

$$\{v_{meas}\} = [D]\{V\}, \tag{5.4}$$

$$\{V\} = [D]^{-1}\{v_{meas}\}, \tag{5.5}$$

where $v_i$ are velocity measurements, $D_{ij}$ are direction cosines from the $i^{th}$ image along the $j^{th}$ direction, and $V$ is the unknown velocity vector. This formulation for SLDV velocity data has been thoroughly investigated by Dominquez [12]. The measured values have some associated error, $\delta v_{meas}$ and $\delta D$, i.e.

$$\{v_{meas} + \delta v_{meas}\} = [D + \delta D]\{V\}. \tag{5.6}$$

The error analysis for this type of matrix formulation has been addressed by Golub [22] and Forsythe [17]. Vest[58], Kreis[32] and Matsumoto et.al. [36] provide error analysis for holgraphic displacement reconstruction ; Abel[1] investigates the error for reconstruction of the velocity vector at a point with SLDV data. In short, each researcher noted that the better the condition number of $[D + \delta D]$, the less chance for error magnification. Kreis[32, p.185] suggests that a Hadamard condition number >0.1 is desirable and notes

> The use of an overdetermined system of equations, which is solved by Gaussian least squares, yields on principle a higher accuracy due to the averaging property, but it will cause nearly the same errors if the sensitivity vectors (direction cosines) are not separated far enough.

Thus another formulation with the same data, but a better conditioning number would be the perferred procedure for recovering the velocity vector. In many cases this improved conditioning number can be achieved through the "relative" reconstruction method.

### 5.2.2 Relative Method

The "relative" method begins with at least four velocity images and forms a different basis set for solving the linear algebra problem by taking the difference between two samples. If the four original data measurements are

$$\begin{aligned} v_{m1} &= D_1 \bullet V, \\ v_{m2} &= D_2 \bullet V, \\ v_{m3} &= D_3 \bullet V, \\ v_{m4} &= D_4 \bullet V, \end{aligned} \tag{5.7}$$

then a set of relative measurements may be formed by

$$\begin{aligned} (v_{m2} - v_{m1}) &= (D_2 - D_1) \bullet V, \\ (v_{m3} - v_{m1}) &= (D_3 - D_1) \bullet V, \\ (v_{m4} - v_{m1}) &= (D_4 - D_1) \bullet V. \end{aligned} \tag{5.8}$$

Alternatively, one relative measurement may be used,

$$\begin{aligned}(v_{m2} - v_{m1}) &= (D_2 - D_1) \bullet V, \\ (v_{m3}) &= (D_3) \bullet V, \\ (v_{m4}) &= (D_4) \bullet V.\end{aligned} \tag{5.9}$$

This is a combination of the absolute and relative methods. In many cases, one of these forms has the best condition number which would minimize the error magnification and result in better estimates of the velocity components. Another approach to improving the estimates is to use a least square's solution for the reconstruction procedure as noted above by Kreis and suggested by Equation 5.7.

### 5.2.3 Least Squares

If more than three velocity images are available, then a least squares solution is another formulation to recover the velocity vector. Similar to Equation 5.5, the matrix form for n views is

$$\begin{aligned}\left\{\begin{matrix} v_1 \\ v_2 \\ \vdots \\ v_n \end{matrix}\right\} &= \begin{bmatrix} D_{11} & D_{12} & D_{13} \\ D_{21} & D_{22} & D_{23} \\ \vdots & \vdots & \vdots \\ D_{n1} & D_{n2} & D_{n3} \end{bmatrix} \left\{\begin{matrix} V_x \\ V_y \\ V_z \end{matrix}\right\}, \\ \{v_{meas}\} &= [D]\{V\}, \\ \{V\} &= \left[D^T D\right]^{-1} D^T \{v_{meas}\}.\end{aligned}$$

Yet this formulation may be inappropriate unless the full least squares model is used and the intercept constant $\beta_0$ is rejected as being statistically insignificant. In other words, the full linear least squares model is

$$y = \beta_0 + \beta_1 x_1 + \beta_2 x_2 + \beta_3 x_3, \tag{5.10}$$

or in the previous notation,

$$v_i = \beta_0 + D_{i1} V_x + D_{i2} V_y + D_{i3} V_z. \tag{5.11}$$

The matrix form is

$$\begin{Bmatrix} v_1 \\ v_2 \\ \vdots \\ v_n \end{Bmatrix} = \begin{bmatrix} 1 & D_{11} & D_{12} & D_{13} \\ 1 & D_{21} & D_{22} & D_{23} \\ \vdots & \vdots & \vdots & \vdots \\ 1 & D_{n1} & D_{n2} & D_{n3} \end{bmatrix} \begin{Bmatrix} \beta_0 \\ V_x \\ V_y \\ V_z \end{Bmatrix}. \tag{5.12}$$

This full least squares model may be statistically compared with the reduced model to determine if the constant $\beta_0$ is insignificant[44, 30]. Dominquez[12, p.150] describes the situation,

> One fundamental characteristic that differentiates the model of Equation 5.3 (Equation 5.5) from all the previous linear models is the lack of an intercept term in the model matrix $\mathbf{X}_v([D])$. The principal reason behind this difference is that the introduction of an intercept term would destroy the physical interpretation of the $\beta_v$ parameters which represent the x-, y-, and z-components of the reconstructed velocity $\mathbf{V}$. Therefore, under this light, the intercept coefficient would be expected to be insignificant.

Unfortunately, Dominquez did not test to see if the intercept coefficient was insignificant. Another view is that the SLDV's pose estimates contain sufficient error such that the calculated direction cosines do not accurately represent the laser beams' line-of-sight and the $\beta_0$ terms cannot be ignored out of hand. Alternatively, this least squares view sheds light on the interpretation of the regressed values; if $\beta_0$ is insignificant, then the regressed coefficients may be interpreted as velocity components; if $\beta_0$ is not insignificant, then the regressed coefficients simply help predict $v_{meas}$, the velocity component that the SLDV "sees", not the x, y, and z velocity components. To claim that the regressed coefficient $V_x$ is the x-direction velocity component is to imply that all the other coefficients, $\beta_0, V_z$ and $V_y$, are insignificant, which is not true. Another view of this situation is that $V_x, V_y, \text{and} V_z$ are biased estimates of the velocity field. These least squares formulations suffer from

> ...a certain mathematical irony in the fact that least-squares problems are both overdetermined , number of data points greater than number of parameters, and underdetermined, ambiguous combinations of parameters exist; but that is how it frequently is. The ambiguities can be exteremely hard to notice a priori in complicated problems [47].

These least squares formulations do not maintain the assumed independence of the surface motions, but couple the motions together via the inner (dot) product. An alternative to these formulations is the use of contravariant bases to solve the velocity reconstruction problem.

### 5.2.4 Contravariant Method

The contravariant base vectors formed from the direction cosines of *three* velocity measurements provides still another formulation to recover the surface point velocity vector. The contravariant basis is defined by Schumann[50] as

$$\mathbf{g}_i \cdot \mathbf{g}^j = \delta_i^j, \tag{5.13}$$

where $g_i \equiv D_i$, the direction cosines of laser beam from the $i^{th}$position, $\mathbf{g}^j$ are the derived contravariant bases, $\delta_i^j$ is the Kroneker delta function, and $\cdot$ is the inner product. With these vector bases the veloctiy vector may be reconstructed[51] by

$$\mathbf{V} = \sum_{j=1}^{3} v_{meas_j} \mathbf{g}^j. \tag{5.14}$$

Figure 5.1 depicts the situation for two dimensions. The advantage of this form is two-fold: the vector structure is preserved and the measured values (with error) appear on only one side of the equation (this will be important for the velocity field reconstruction). The absolute and relative methods may be used in conjunction with this procedure to achieve the best numerical solution. Additionally, the direction cosines may be defined in any convenient, local coordinate system so that the derived velocity components are meaningful. Specifically for a surface point, the direction cosines may be referred to the local surface coordinate system so that out-of-plane and in-plane velocity components may be regressed independently of one another. This approach is consistent with the assumed orthogonal, independent surface motions. The following section illustrates the absolute, relative, and contravariant methods with numerical and experimental examples.

### 5.2.5 Examples of Point Velocity Reconstruction

The purpose of this section is to numerically illustrate the point velocity reconstruction methods. Figure 5.2 depicts the experimental situation that is being modeled with this

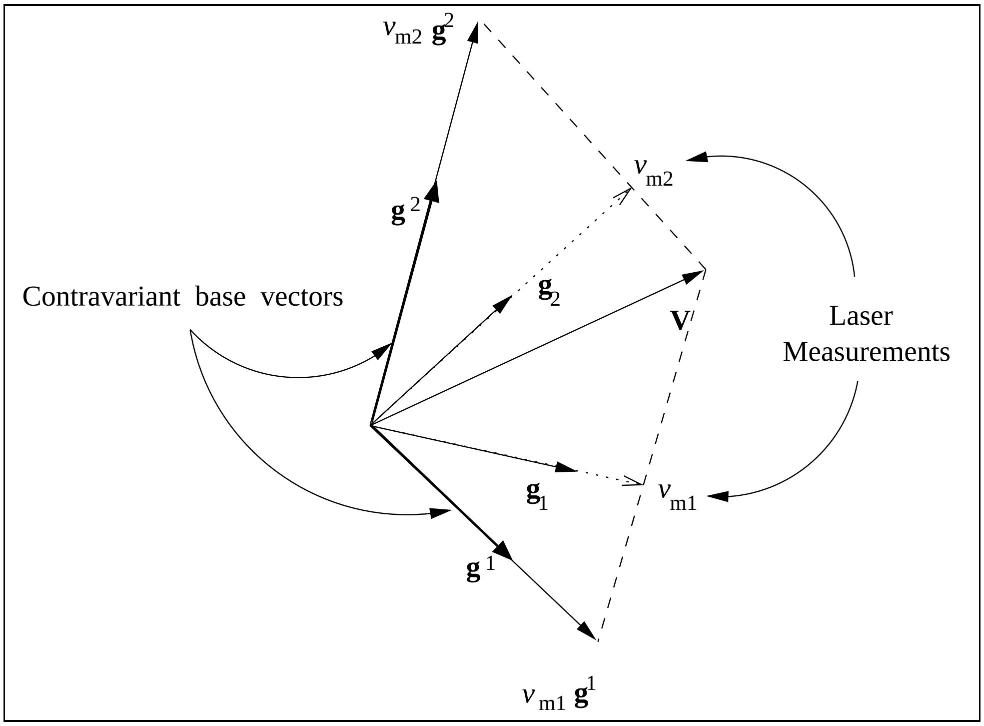

**Figure 5.1: Contravariant Vector Bases**

**Table 5.1: Laser Direction Cosines and Velocity Measurements -Simulated**

| $i^{th}$ Laser Position Dir. Cos. | $\hat{\imath}$ | $\hat{\jmath}$ | $\hat{k}$ | vel. measured |
|---|---|---|---|---|
| $\mathbf{D}_1$ | -0.0056 | +0.2293 | 0.9733 | 49.1141 |
| $\mathbf{D}_2$ | 0.3525 | +0.2493 | 0.9020 | 46.3045 |
| $\mathbf{D}_3$ | 0.1813 | +0.1362 | 0.9739 | 49.3322 |
| $\mathbf{D}_4$ | -0.1338 | -0.0738 | 0.9883 | 48.9977 |
| $\mathbf{D}_5$ | 0.3387 | -0.0610 | 0.9389 | 47.5010 |

example. The velocity at point $P_{2500}$ is

$$\mathbf{V}_p = 2\hat{\imath} + 2\hat{\jmath} + 50\hat{k}. \tag{5.15}$$

The direction cosines of the five SLDV positions and the simulated SLDV measured velocities are shown in Table 5.1. Using the absolute method, the partial least squares method, and full least squares model, the reconstructed velocity vectors and condition numbers of the $[D]^{-1}$ or $\left[D^T D\right]^{-1}$ are shown in Table 5.2. The first row in the table specifies the recontruction method employed: method 1 recovers the velocity vector with three absolute measurements; method 2 uses a least squares solution of five absolute measurements without an intercept term; and method 3 is the full least squares solution (includes the intercept term) with five absolute measurements. The second line describes which SLDV positions

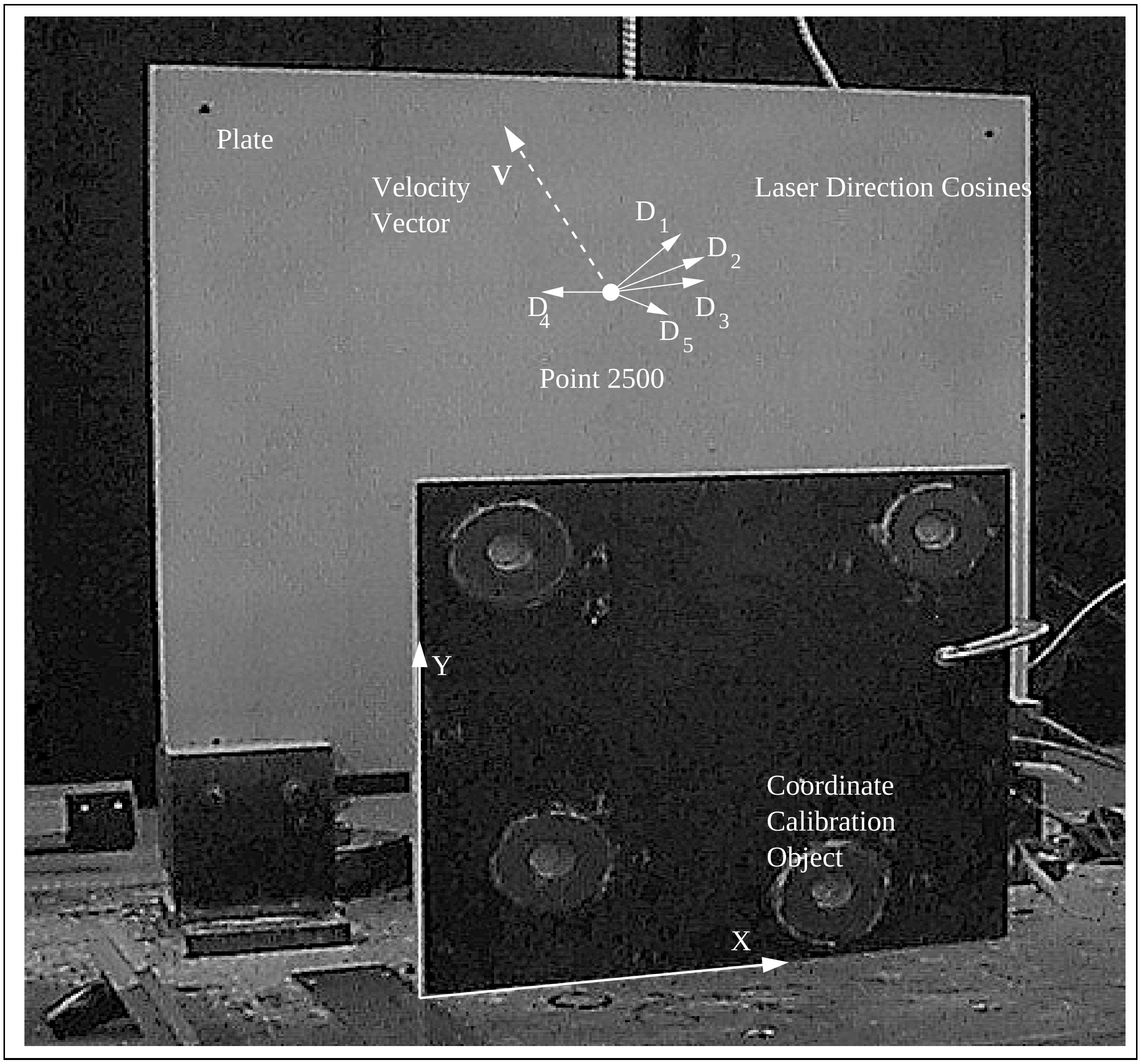

Figure 5.2: Velocity Vector Reconstruction

**Table 5.2: Velocity Vector Reconstruction - Absolute Methods**

| Method | 1 | 2 | 3 |
|---|---|---|---|
| Data Pts | 1,2,3 | 1,2,3,4,5 | 1,2,3,4,5 |
| $V_x$ | 2.0000 | 2.0000 | 2.0000 |
| $V_y$ | 2.0000 | 2.0000 | 2.0000 |
| $V_z$ | 50.0000 | 50.0000 | 50.0000 |
| $\beta_0$ | N/A | N/A | 0.0000 |
| rcond # | 0.0380 | 0.0159 | 5.2866e-05 |

**Table 5.3: Velocity Vector Reconstruction - Relative Methods**

| Method | 4 | 5 | 6 |
|---|---|---|---|
| Data Pts | 2-1,3-1,4-1 | 2-1,3-1,4-1,5-1 | 1-5,2,4 |
| $V_x$ | 2.0000 | 2.0000 | 2.0000 |
| $V_y$ | 2.0000 | 2.0000 | 2.0000 |
| $V_z$ | 50.0000 | 50.0000 | 50.0000 |
| rcond # | 0.0655 | 0.0028 | 0.2037 |

are used to compute the tabular entries. The next three lines in the table are the computed values for the reconstructed velocity vector. The final row is the condition number for the appropriate matrices. For perfect data without experimental error, the same velocity vector is recovered even though the condition numbers vary significantly.

Using the relative method, the least squares relative model, and combined least squares method, the reconstructed velocity vectors and condition numbers of the $[D]^{-1}$ or $\left[D^T D\right]^{-1}$ are shown in Table 5.3. The table's first row indicates the particular method: method 4 determines the velocity vector from three relative measurements; method 5 uses the partial least squares method (without the intercept term) and five relative measurements; and method 6 employs one relative and two absolute measurements in combination to recover the velocity vector. The second line in Table 5.3 details which SLDV data are used with the particular method to complete the table. The relative measurement $v_2 - v_1 = (D_2 - D_1) \cdot V^T$ is indicated by 2-1. The following three lines in the table are the reconstructed velocity components. The last line is the matrix condition numbers for the respective data and method. The best condition number occurs with method 6 which combines relative and absolute measurements. In fact this method meets Kreis's criteria for the matrix condition number, i.e. condition number $> 0.1$. Once again, perfect data without error results in the recovery of the same, true velocity vector.

The contravariant method also recovers the same velocity vector from a set of three

**Table 5.4: Laser Direction Cosines and Velocity Measurements -Experimental**

| $i^{th}$ Laser Position Dir. Cos. | $\hat{\imath}$ | $\hat{\jmath}$ | $\hat{k}$ | vel. measured |
|---|---|---|---|---|
| $\mathbf{D}_1$ | -0.0095 | +0.2203 | 0.9754 | $v_1$ = -0.5531 + 0.5608i |
| $\mathbf{D}_2$ | 0.3488 | +0.2398 | 0.9060 | $v_2$ = -0.5576 + 0.5000i |
| $\mathbf{D}_3$ | 0.1771 | +0.1265 | 0.9760 | $v_3$ = -0.6094 + 0.5640i |
| $\mathbf{D}_4$ | -0.1378 | -.0837 | 0.9869 | $v_4$ = -0.5462 + 0.4673i |
| $\mathbf{D}_5$ | 0.3337 | -0.0712 | 0.9400 | $v_5$ = -0.5387 + 0.4455i. |

velocity measurements. Using the first three SLDV data points from Table 5.1, the contravariant base vectors may be calculated,

$$\mathbf{g}_1 \equiv \mathbf{D}_1 \qquad \mathbf{g}_2 \equiv \mathbf{D}_2 \qquad \mathbf{g}_3 \equiv \mathbf{D}_3,$$

$$\mathbf{g}_i \cdot \mathbf{g}^j = \delta_i^j,$$

$$\mathbf{g}^1 = -3.0627\hat{\imath} + 4.5905\hat{\jmath} - 0.0717\hat{k},$$

$$\mathbf{g}^2 = 2.3190\hat{\imath} + 4.6467\hat{\jmath} - 1.0818\hat{k},$$

$$\mathbf{g}^3 = 0.9131\hat{\imath} - 8.8920\hat{\jmath} + 2.1003\hat{k}.$$

The velocity vector is determined by,

$$\mathbf{V} = v_1\mathbf{g}^1 + v_2\mathbf{g}^2 + v_3\mathbf{g}^3$$

$$\mathbf{V} = 2\hat{\imath} + 2\hat{\jmath} + 50\hat{k}.$$

In this example three absolute measurements were used, but a combination of relative and absolute measurements could be employed. This is important as the contravariant base vectors are the "inversion" of the matrix of direction cosines. With this in mind, choosing the best set of measurements, the set which has the best condition number, would be the appropriate choice when using the contravariant method. Among the entries in Tables 5.2 and 5.3, the best condition number is the method which combines relative and absolute velocity measurements. This combination will be used in velocity field reconstruction process, specifically in the "relative" and "contravariant" methods.

The same tables are now generated from experimental data. The measured velocity and direction cosines of point 2500 in plate19mar data are shown in Table 5.4.

Using the absolute method, the least squares absolute method, and full least squares absolute model, the experimental, reconstructed velocity vectors and condition numbers of

**Table 5.5: Experimental Velocity Vector Reconstruction - Absolute**

| Method | 1 | 2 | 3 |
|---|---|---|---|
| Data Pts | 1,2,3 | 1,2,3,4,5 | 1,2,3,4,5 |
| $V_x$ | -0.1515 - 0.0464i | -0.0726 - 0.0288i | -0.1519 + 0.1345i |
| $V_y$ | 0.2943 - 0.1225i | -0.0836 + 0.3010i | -0.1040 + 0.3429i |
| $V_z$ | -0.6350 + 0.6021i | -0.5681 + 0.5078i | -1.1830 + 1.7743i |
| $\beta_0$ | N/A | N/A | 0.6015 - 1.2390i |
| std | N/A | 0.0293 | 0.0171 |
| SSE | N/A | 0.0034 | 0.0012 |
| rcond # | 0.0381 | 0.0161 | 5.3002e-05 |

the $[D]^{-1}$ or $\left[D^T D\right]^{-1}$ are shown in Table 5.5. The three methods in this table are: method 1 - three absolute velocity measurements; method 2 - five absolute velocity measurements solved with least squares without an intercept term; and method 3 - full least squares with five absolute velocity measurements. This time the solution vectors are different from one another. The intercept term $\beta_0$ is not zero as in Table 5.2. The "correct" velocity is not easily discerned.

Using the relative method, the least squares relative method, and combined least squares method, the experimental, reconstructed velocity vectors and condition numbers of the $[D]^{-1}$ or $\left[D^T D\right]^{-1}$ are shown in Table 5.6. The methods are the same as in Table 5.3: method 4 - three relative velocity measurements are used to recover the velocity vector; method 5 - five relative velocity measurements are employed with least squares to reconstruct the vector; method 6 - one relative and two absolute velocity measurements yield a reconstructed velocity vector. Method 4 and 5 have significantly different out-of-plane velocities from those in Table 5.5. This is a result of the "relative" process which forms base vectors which lie principally in-plane and provide little discrimination in the out-of-plane direction. Method 6 with the largest matrix condition number is the best solution as the potential for error magnification is minimized. However, this does not mean the answer is correct.

Using the first three data points in Table 5.4, the contravariant method is used to reconstruct the velocity vector. Calculating the contravariant bases,

$$\mathbf{g}_1 \equiv \mathbf{D}_1 \qquad \mathbf{g}_2 \equiv \mathbf{D}_2 \qquad \mathbf{g}_3 \equiv \mathbf{D}_3,$$

$$\mathbf{g}_i \cdot \mathbf{g}^j = \delta_i^j,$$

$$\mathbf{g}^1 = -3.0494\hat{\imath} + 4.5969\hat{\jmath} - 0.0425\hat{k},$$

**Table 5.6: Experimental Velocity Vector Reconstruction - Relative**

| Method | 4 | 5 | 6 |
|---|---|---|---|
| Data Pts | 2-1,3-1,4-1 | 2-1,3-1,4-1,5-1 | 1-5,2,4 |
| $V_x$ | -0.2755 + 0.1650i | -0.1770 + 0.1407i | -0.0736 - 0.0416i |
| $V_y$ | 0.0427 + 0.3066i | -0.0423 + 0.3276i | -0.0668 + 0.2866i |
| $V_z$ | -1.3460 + 1.8146i | -1.0833 + 1.7496i | -0.5694 + 0.4920i |
| std | N/A | 0.0232 | N/A |
| SSE | N/A | 0.0019 | N/A |
| rcond # | 0.0657 | 0.0028 | 0.2041 |

$$\mathbf{g}^2 = 2.3392\hat{\imath} + 4.6492\hat{\jmath} - 1.0272\hat{k},$$

$$\mathbf{g}^3 = 0.8760\hat{\imath} - 8.9096\hat{\jmath} + 2.0205\hat{k},$$

the velocity vector may now be calculated,

$$\begin{aligned}\mathbf{V} &= v_1\mathbf{g}^1 + v_2\mathbf{g}^2 + v_3\mathbf{g}^3,\\ \mathbf{V} &= (-0.1515 - 0.0464i)\hat{\imath} + (0.2943 - 0.1225i)\hat{\jmath} + (-0.6350 + 0.6021i)\hat{k}.\end{aligned}$$

The contravariant bases results in the same velocity vector as method 1 of Table 5.5 because the contravariant bases are the ”inversion” of the direction cosines,

$$\left[D^T\right]^{-1} = \begin{bmatrix} -3.0494 & 4.5969 & -0.0425 \\ 2.3392 & 4.6492 & -1.0272 \\ 0.8760 & -8.9096 & 2.0205 \end{bmatrix} \tag{5.16}$$

The results of these solution methods have used the direction cosines which were defined in a world coordinate system. With the exception of the contravariant method, the choice of this coordinate system does not impact the solution as the independent surface motions are coupled together through the solution formulation, essentially a scalar form. The contravariant method is a vector form which can benefit from choosing the most convenient coordinate system, the local coordinate system with normal and tangential directions. This choice of coordinate system is advantageous as typical structures have velocity components principally in the normal direction. Additionally, thin-shell theory separates the surface motion into normal and tangential components [54, 20, 8, 59, 14, 4] for which the contravariant method is ideally suited, i.e. the velocity point solution is defined by similar normal and tangential directions.

### 5.2.6 Discussion of Results

The reconstruction of the velocity field at a point with experimental data, summarized in Tables 5.5 and 5.6, has resulted in widely varying velocity vectors which represent the structure's surface velocity. If the data has no experimental errors, then the same vector would be calculated by each method as demonstrated in Tables 5.2 and 5.3. With experimental error, different answers present themselves to the researcher for interpretation. The examples above may be classified into two groups, *least squares* solutions and *non-least squares.* The non-least squares can be ranked according to the conditioning numbers (condition numbers $\ll 1$ representing the most ill-conditioned matrices and a condition number of 1 being ideal). Using Kreis' criteria, only one solution is viable, that of the combined absolute and relative measurements, method 6 in Table 5.6. The other non-least squares approaches have condition numbers so poor, that experimental error can significantly impact the solution, i.e. the potential for propagation of error bound is too large to permit the answer to be meaningful. Between the two least squares solutions, methods 2 and 3 in Table 5.5, statistical testing may be used to see if additional degrees of freedom help model the acquired data. In this case, the solution with the $\beta_0$ constant is not statistically significant so that the best least squares solution is the simple $V_x, V_y, V_z$ model. The F statistic test[44, p.656] for this case is

$$F = \frac{SSE_{drop}}{MSE} = \frac{.0022}{0.0029} = 7.523 < F_{1,4,\alpha=0.05} = 7.71 \tag{5.17}$$

so that the hypothesis that $\beta_0$ is zero is not rejected (Here $SSE_{drop}$ is "the drop in the sum of squares error obtained form the complete model; MSE is the mean square error for the complete model."[44]) Comparing the best solutions from each group, the best non-least squares vector lies within the confidence intervals of the best least squares solution so that the two solutions may be considered "statistically equivalent." The partial, least squares regressed coefficients and the best non-least sqares solutions are

| Components | Least Squares | Non-least Squares |
|---|---|---|
| $V_x =$ | $-0.0726 \pm 0.3238 - 0.0288i \pm 0.3238i$ | $-0.0736 - 0.0416i$ |
| $V_y =$ | $-0.0836 \pm 0.6242 + 0.3010i \pm 0.6242i$ | $-0.0668 + 0.2866i$ |
| $V_z =$ | $-0.5681 \pm 0.0213 + 0.5078i \pm 0.0213i$ | $-0.5694 + 0.4920i$ |

The confidence intervals for the regressed coefficients are [44]

$$\hat{\beta}_i \pm t_{\frac{\alpha}{2}} s_{\varepsilon} \sqrt{v_{ii}}, \tag{5.18}$$

where $s_{\varepsilon}$ is the standard deviation, $t_{\frac{\alpha}{2}}$ is the t-test statistic, and $v_{ii}$ is the $i$th diagonal element of $\left[D^T D\right]^{-1}$. Once the best solutions are identified, the question of interpretation arises, i.e. do the results have physical meaning?

### 5.2.7 Interpretation of Results

The interpretation of the best least squares solution follows the standard least squares model where the regressed coefficients are used to predict the measured values, in this case laser velocity measurements. An alternative interpretation of the regressed values is that they represent the velocity components at the structure's surface. With this latter assumption, the researcher may be interested in what the laser would measure along the x-direction. Using the appropriate direction cosines (1,0,0) and the regressed coefficients, the apparent x-velocity component is predicted. Is this permissible with the least squares model? Adopting this viewpoint (along the x-direction) implies that the $V_y, V_z$ coefficients are zero, i.e. not statistically significant for the least squares model. The appropriate statistical test may be applied to determine if these coefficients are necessary. However, when this test is applied, the hypothesis that these coefficients are zero is rejected and the coefficients must be included in the model. The researcher must conclude that the regressed coefficients may not be interpreted as surface velocity components. This does not imply that the regressed coefficients may be the surface velocity components, just that the least squares model does not support this interpretation.

## 5.3 Velocity Field Reconstruction

The reconstruction of the velocity field is similar to the reconstruction of the velocity vector at a point; the major difference is the expansion of the point domain to a surface or a family of surfaces. These domains are discretized and solved with the least squares method using local finite element basis functions. Additionally, the same absolute, relative, and contravariant methods may be applied as with the velocity vector reconstruction. The following sections describe the reconstruction of the velocity field for a family of surfaces (a volume).

### 5.3.1 Reconstruction Procedure

The reconstruction of the velocity field is a four step process. First the registered velocity images are acquired, the SLDV pose is determined with the automated procedure developed in Chapter 4. Secondly the family of surfaces defining the volume for velocity recovery is specified so that this volume includes the actual surface, even if the surface is not known exactly. The third step is to define sample points within this volume and determine the corresponding image points in the registered velocity images. The interpolated velocity data at these image points serve as measurement data for the least squares reconstruction solution. This process is discussed in the following paragraphs.

### 5.3.2 Acquired Velocity Images

The velocity reconstruction process begins with the acquisition of at least four velocity images. This data acquisition is described in Chapter 3. One of these velocity images of the vibrating plate is depicted in Figure 5.3. Four velocity images are necessary for the least squares absolute method; five velocity images are necessary for the least squares relative or combined (absolute and relative measurements) methods. These data sets are the fundamental, experimental observations of the structure's surface velocity field.

### 5.3.3 Volume Definition

The family of surfaces which define the volume of interest for velocity reconstruction is based upon triangular, prismatic elements. The element nodes are located in the neighboring space of the actual surface. The nodes for one "surface" layer are shown in Figure 5.4. (The coordinate system here is the world coordinate system attached to the calibration object.) The nodal connectivity serves to discretize the volume. The discretized volume for the plate test object is shown in Figure 5.5. These prismatic elements help to define sample points in the volume.

### 5.3.4 Sample Point Definition

The sample points in the volume of interest are specified with finite element parameters for the prismatic elements. If the parameters are $\xi_1, \xi_2, \xi_3, \zeta$, then a point is defined in each prismatic element by the finite element basis functions and the nodal coordinates. For

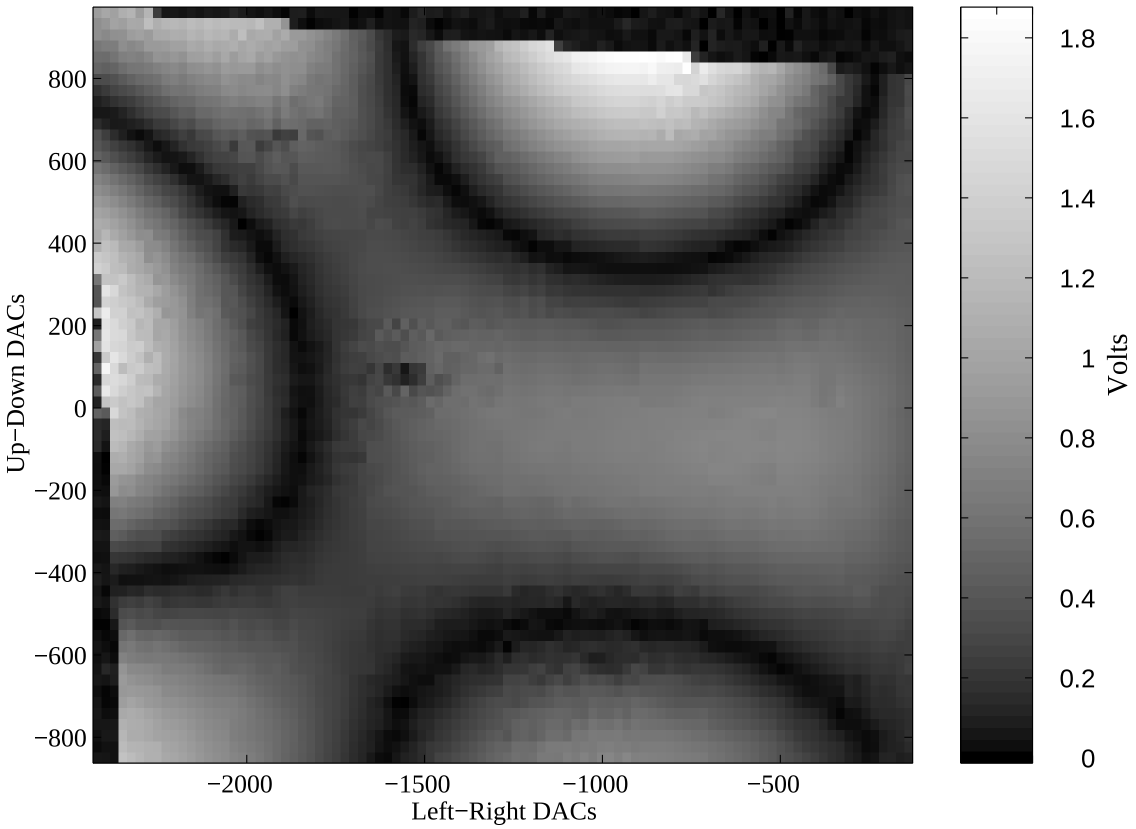

Figure 5.3: Velocity Image of Plane

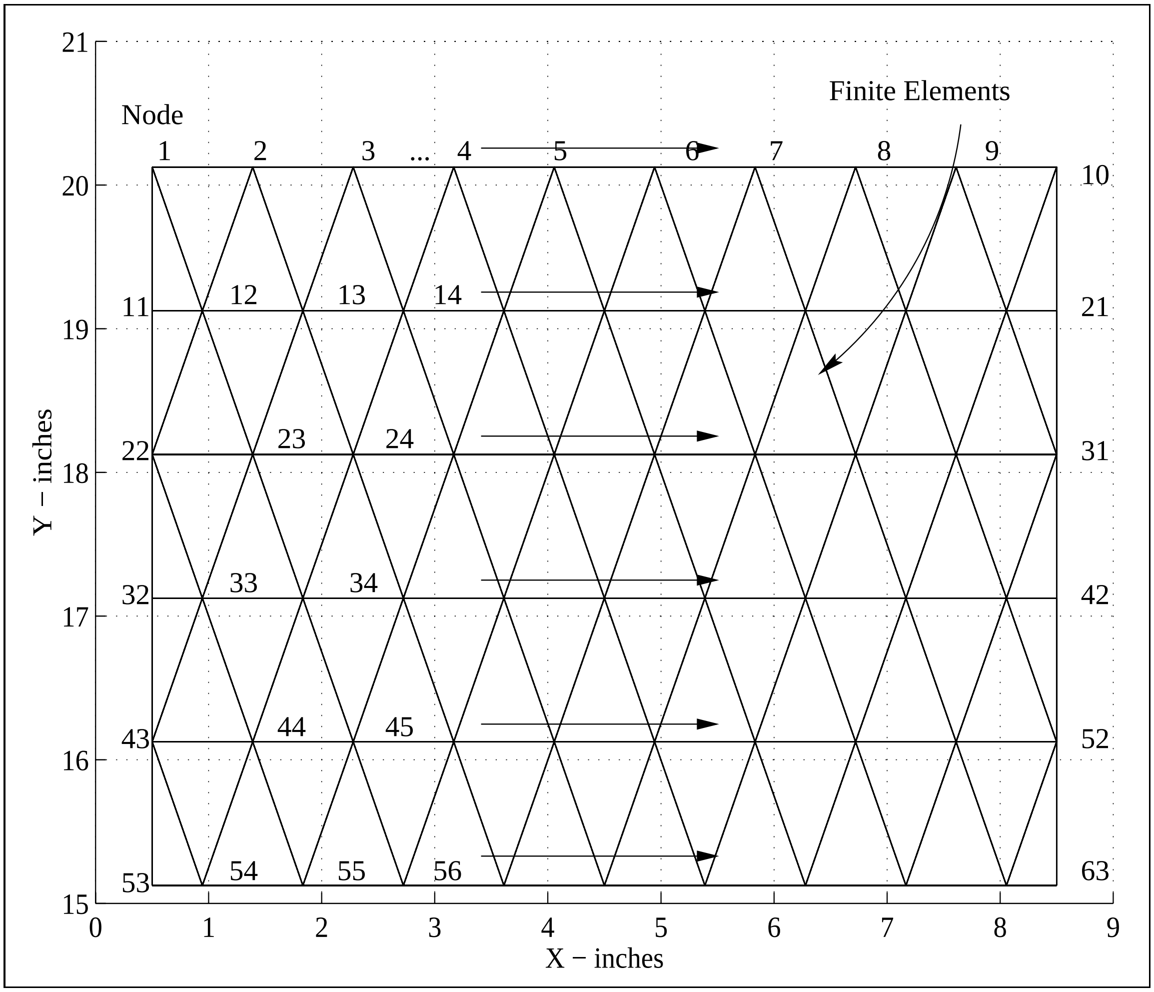

**Figure 5.4: Finite Element Grid for One Surface**

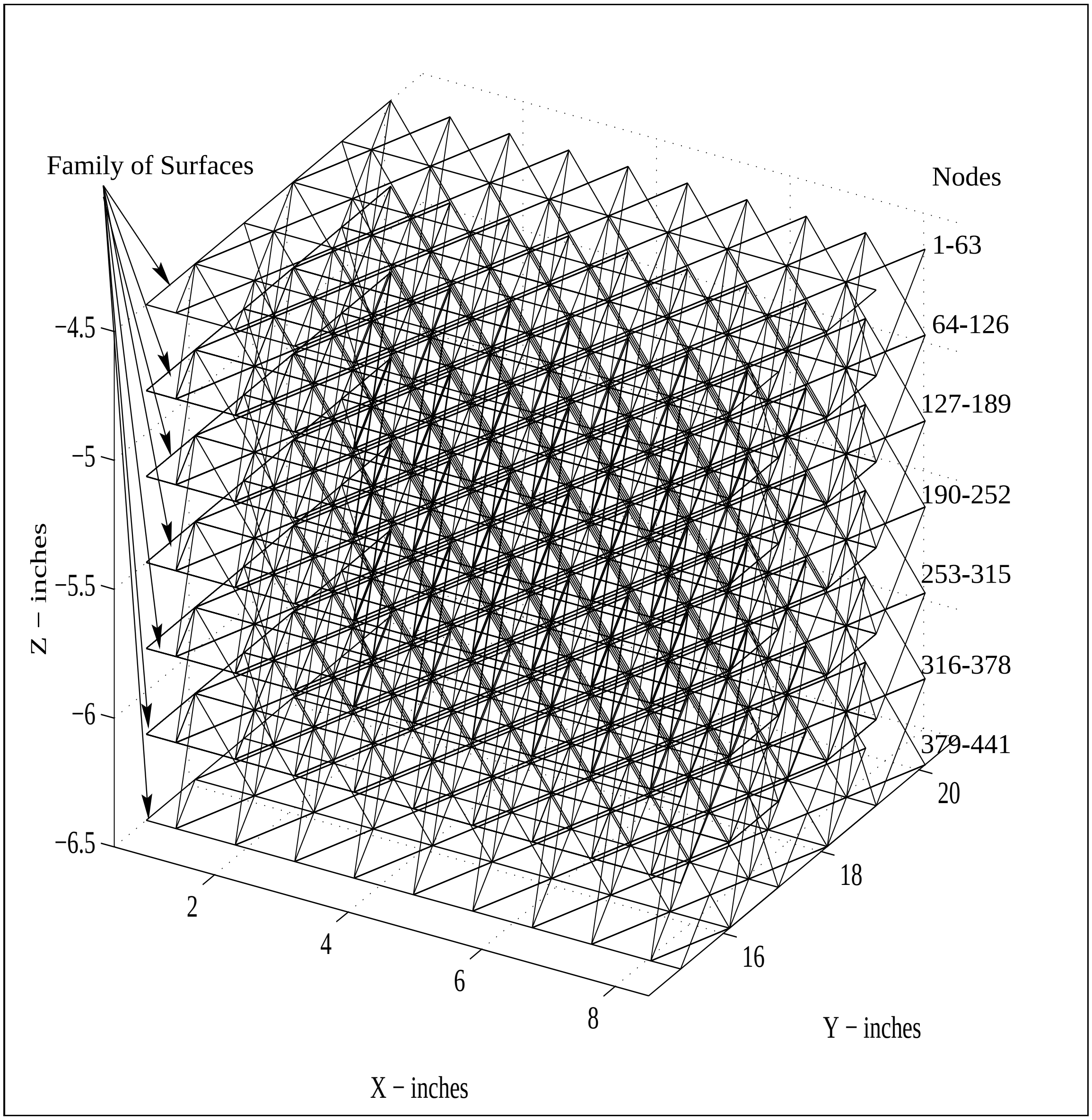

**Figure 5.5: Finite Element Volume**

example, if

$$\begin{aligned}
\xi_1 &= \tfrac{1}{3} \qquad -1 \leq \xi_1 \leq 1 \\
\xi_2 &= \tfrac{1}{3} \qquad -1 \leq \xi_2 \leq 1 \\
\xi_3 &= \tfrac{1}{3} \qquad -1 \leq \xi_3 \leq 1 \\
& \qquad \xi_1 + \xi_2 + \xi_3 = 1 \\
\zeta &= \tfrac{1}{2} \qquad -1 \leq \zeta \leq 1
\end{aligned} \tag{5.19}$$

and the triangular, prismatic basis functions are

$$\begin{aligned}
N_1 &= \xi_1 \tfrac{(1-\zeta)}{2}, \\
N_2 &= \xi_2 \tfrac{(1-\zeta)}{2}, \\
N_3 &= \xi_3 \tfrac{(1-\zeta)}{2}, \\
N_4 &= \xi_1 \tfrac{(1+\zeta)}{2}, \\
N_5 &= \xi_2 \tfrac{(1+\zeta)}{2}, \\
N_6 &= \xi_3 \tfrac{(1+\zeta)}{2},
\end{aligned} \tag{5.20}$$

then the corresponding point is found by evaluation of the appropriate basis functions at those nodal coordinates,

$$\begin{aligned}
\mathbf{P}(\xi_1, \xi_2, \xi_3, \zeta) &= \sum_{i=1}^{6} N_i \mathbf{P}_i \\
P_x(\xi_1, \xi_2, \xi_3, \zeta) &= N_1 P_{x1} + N_2 P_{x2} + \ldots N_6 P_{x6} \\
P_y(\xi_1, \xi_2, \xi_3, \zeta) &= N_1 P_{y1} + N_2 P_{y2} + \ldots N_6 P_{y6} \\
P_z(\xi_1, \xi_2, \xi_3, \zeta) &= N_1 P_{x1} + N_2 P_{x2} + \ldots N_6 P_{z6}
\end{aligned}$$

This is done for each prismatic element for each parameter quadrapule. The minimum number of points in each element which must be evaluated is dependent upon the number of degrees of freedom at each node and the number of velocity images acquired. If each node has three degrees of freedom, then at least eighteen "measurements" must be made. If five velocity images are available, then a least four points must be defined in each prismatic element by four parameter quadrapules. Once the sample/object points in the volume are defined, the image points in each velocity image must be determined.

### 5.3.5 Image Points

The true advantage of modeling the SLDV with a compter vision model is the recovery of image points which correspond to object points and thereby provide an interpolated velocity measurement for that image point. Given the coordinates of the object point in the world coordinate system (wcs) and the transformation matrix found with the SLDV pose process, the object points may be placed in the laser coordinate system (lcs) and the mirror angles (voltages) determined. The process is described in Zeng's dissertation [61, p.14], but is recalled below

$$\begin{aligned}
\mathbf{P}_{lcs} &= \mathbf{P}_{wcs}\,[T_x]_{wcs}^{lcs}\,,\\
\theta_{ud} &= \tan^{-1}(P_{y,lcs}/P_{z,lcs}),\\
\theta_{lr} &= \tan^{-1}(P_{x,lcs}/(\sqrt{P_{y,lcs}^2+P_{z,lcs}^2}+\text{mirror offset}),
\end{aligned}$$

where $\theta_{ud}$ is the up-down mirror angle, $\theta_{lr}$ is the left-right mirror angle, and $\mathbf{P}_{lcs}$ is the object point in the laser coordinate system. These image points may be used with the velocity images to determine interpolated velocity measurement values. Figure 5.6 illustrates the image points of object points generated in the finite element volume. These interpolated velocity values at the image points of the specified object points are employed in a least squares solution of the velocity field.

### 5.3.6 Least Squares Solution

The least squares solution to the velocity field reconstruction problem may be divided into the same categories as with the velocity vector reconstruction: absolute method, relative method, combined relative and absolute, and the contravariant method. The basic approach is to allow each velocity measurement derived above to be one sample of the velocity field represented by finite element basis functions over a discretized domain. The velocity field at a point may be represented by

$$\mathbf{V}(x,y,z)=\sum_{j=1}^{m}\sum_{i=1}^{n}\mathbf{V}_i N_i(\xi_1,\xi_2,\xi_3,\zeta), \tag{5.21}$$

where $V_i$ are the nodal velocities, $N_i(\xi_1,\xi_2,\xi_3,\zeta)$ are the basis functions, and the first sum is over the number of elements, m, and the second sum is over the number of nodes,n, for each element. Since the laser measures the velocity component at a point along its line of sight and realizing that the point lies in one element, the measured velocity is

$$v_m(x,y,z)=\sum_{i=1}^{n}\mathbf{V}_i N_i(\xi_1,\xi_2,\xi_3,\zeta)\cdot D(x,y,z), \tag{5.22}$$

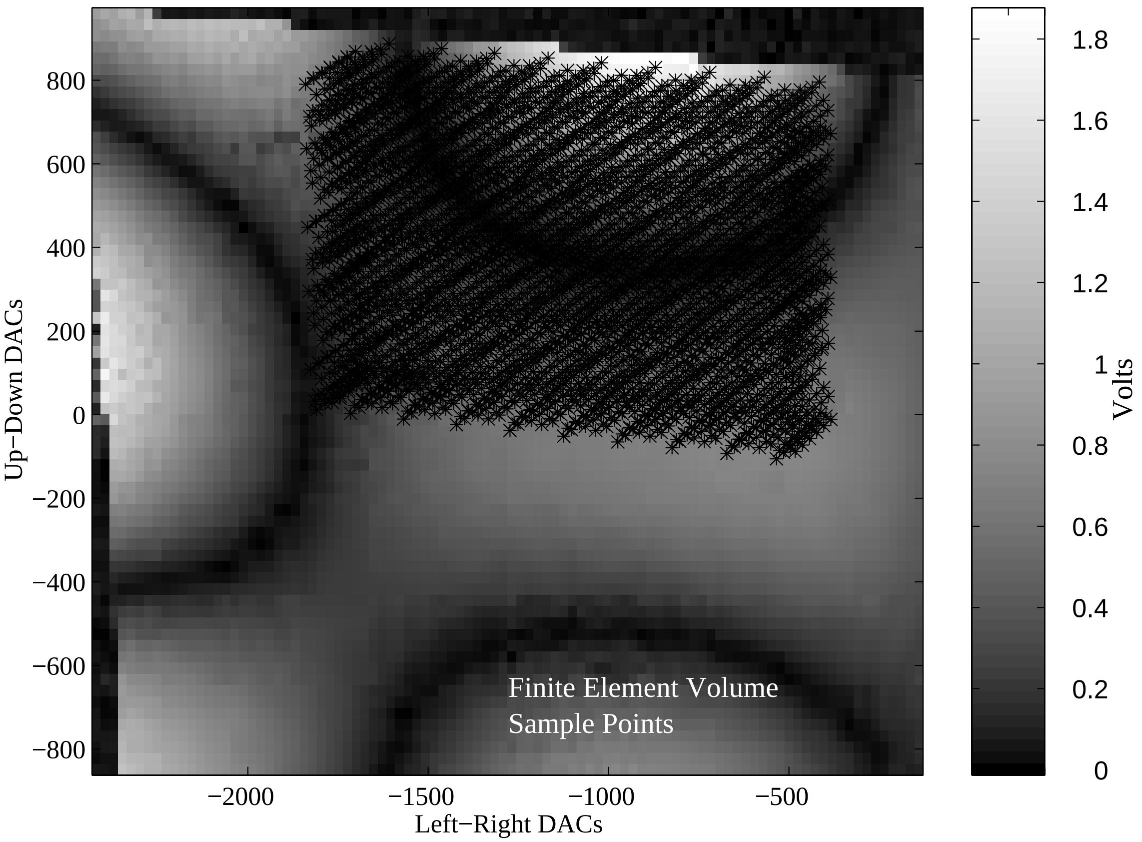

**Figure 5.6: Image Points of Finite Element Volume Object Points**

or expanding for a triangular prismatic element,

$$\begin{aligned} v_m(x,y,z) \;=\; & (V_{x1}N_1 + V_{x2}N_2 + V_{x3}N_3 + V_{x4}N_4 + V_{x5}N_5 + V_{x6}N_6)D_x(x,y,z) + \\ & (V_{y1}N_1 + V_{y2}N_2 + V_{y3}N_3 + V_{y4}N_4 + V_{y5}N_5 + V_{y6}N_6)D_y(x,y,z) + \\ & (V_{z1}N_1 + V_{z2}N_2 + V_{z3}N_3 + V_{z4}N_4 + V_{z5}N_5 + V_{z6}N_6)D_z(x,y,z). \end{aligned}$$

The left hand side is the interpolated velocity measurement from the image point. For each velocity image a measurement is taken along with the corresponding direction cosines. This process continues until all the sample points in the volume have been evaluated. These velocity measurements,

$$\begin{aligned} v_{m1} &= V_{x1}N_1^{m1}D_x^{m1} + \ldots + V_{x6}N_6^{m1}D_x^{m1} + V_{y1}N_1^{m1}D_y^{m1} + \ldots + V_{z6}N_6^{m1}D_z^{m1} \\ v_{m2} &= V_{x1}N_1^{m2}D_x^{m2} + \ldots + V_{x6}N_6^{m2}D_x^{m2} + V_{y1}N_1^{m2}D_y^{m2} + \ldots + V_{z6}N_6^{m2}D_z^{m2} \\ \vdots \; & \vdots \qquad\qquad\qquad\qquad \vdots \\ v_{mn} &= V_{x1}N_1^{mn}D_x^{mn} + \ldots + V_{x6}N_6^{mn}D_x^{mn} + V_{y1}N_1^{mn}D_y^{mn} + \ldots + V_{z6}N_6^{mn}D_z^{mn}. \end{aligned} \tag{5.23}$$

may be collected into one large matrix,

$$\left\{ \begin{array}{c} v_{m1} \\ v_{m2} \\ \vdots \\ v_{mn} \end{array} \right\} = \left[ \begin{array}{cccc} N_1^{m1}D_x^{m1} & \ldots + N_6^{m1}D_x^{m1} + N_1^{m1}D_y^{m1} & \ldots + N_6^{m1}D_z^{m1} \\ N_1^{m2}D_x^{m2} & \ldots + N_6^{m2}D_x^{m2} + N_1^{m2}D_y^{m2} & \ldots + N_6^{m2}D_z^{m2} \\ \vdots & \vdots\vdots\vdots & \vdots\vdots \\ N_1^{mn}D_x^{mn} & \ldots + N_6^{mn}D_x^{mn} + N_1^{mn}D_y^{mn} & \ldots + N_6^{mn}D_z^{mn} \end{array} \right] \left\{ \begin{array}{c} V_{x1} \\ \vdots \\ V_{x6} \\ V_{y1} \\ \vdots \\ V_{z6} \end{array} \right\},$$

or more compactly,

$$\{v_m\} = [N_D]\{V_{nodal}\}. \tag{5.24}$$

This equation may be solved using least squares,

$$\left[N_D^T N_D\right]^{-1}\left[N_D^T\right]\{V_m\} = \{V_{nodal}\}. \tag{5.25}$$

This is the basic approach to reconstructing the velocity field. When the simple velocity measurements are used (interpolated image points), the absolute method is being employed. When the difference between two interpolated image points (from different velocity images, but image points of the same object point) are used, the relative measurement (method) is the input data to the least squares solution process. Of course a combination of the two methods may give better results since the fundamental inversion process is characterized by the condition number. The condition number of $\left[N_D^T N_D\right]^{-1}$ determines how errors may be magnified.

As with the velocity reconstruction at a point, the typical least squares solution above would have offset terms, $\beta_0 s$, in the formulation and a statistical test to determine if the terms are statistically insignificant. The velocity field, over an element, would be modeled as

$$\mathbf{V}(x,y,z) = \sum_{i=1}^{n} (V_{xi} N_i + V_{yi} N_i + V_{zi} N_i + \beta_i N_i), \tag{5.26}$$

where the $\beta_i s$ are another degree of freedom at each node. Expanding this formulation for a single element results in

$$\left\{ \begin{array}{c} v_{m1} \\ v_{m2} \\ \vdots \\ v_{mn} \end{array} \right\} = \left[ \begin{array}{cccccc} N_1^{m1} D_x^{m1} & + \dots & +N_6^{m1} D_z^{m1} + N_1 + N_2 & \dots & +N_6 \\ N_1^{m2} D_x^{m2} & + \dots & +N_6^{m2} D_z^{m2} + N_1 + N_2 & \dots & +N_6 \\ \vdots & \vdots & \vdots & \vdots & \vdots \\ N_1^{mn} D_x^{mn} & + \dots & +N_6^{mn} D_z^{mn} + N_1 + N_2 & \dots & +N_6 \end{array} \right] \left\{ \begin{array}{c} V_{x1} \\ \vdots \\ V_{z6} \\ \beta_1 \\ \beta_2 \\ \vdots \\ \beta_n \end{array} \right\}, \tag{5.27}$$

which can be solved with the least squares method. As before, the absolute, relative or combined velocity measurement methods may be used in setting up the least squares matrices. The last approach to determining the velocity field is the contravariant method.

The contravariant method may be used to great advantage when formulated for the least squares technique. As noted earlier, the contravariant basis and the velocity vector reconstruction is defined by

$$\mathbf{g}_i \cdot \mathbf{g}^j = \delta_i^j,$$

$$\mathbf{V} = \sum_{j=1}^{3} v_{meas_j} \mathbf{g}^j.$$

where the three measurements are $v_{meas_j}$ and the associated direction cosines are $g_i$. This may be expanded to a field form by sampling multiple points in the discretized volume and representing the velocity field with the corresponding basis functions. The velocity field over a single element is

$$\mathbf{V}(x,y,z) = \sum_{i=1}^{n} \mathbf{V}_i N_i(\xi_1, \xi_2, \xi_3, \zeta), \tag{5.28}$$

where $V_i$ are the unknown nodal velocity values and $N_i$ are the appropriate basis functions for the elememt having $n$ basis functions. Using three velocity images for determining the interpolated velocity values at each sample point, the velocity field at the sample point may be modeled by

$$\begin{array}{rcl}
\sum_{i=1}^{n} \mathbf{V}_i N_i(\xi_{11}, \xi_{21}, \xi_{31}, \zeta_1) & = & \sum_{j=1}^{3} v_{m1_j} \mathbf{g}^j \\
\sum_{i=1}^{n} \mathbf{V}_i N_i(\xi_{12}, \xi_{22}, \xi_{32}, \zeta_2) & = & \sum_{j=1}^{3} v_{m2_j} \mathbf{g}^j \\
\sum_{i=1}^{n} \mathbf{V}_i N_i(\xi_{13}, \xi_{23}, \xi_{33}, \zeta_3) & = & \sum_{j=1}^{3} v_{m3_j} \mathbf{g}^j \\
\vdots & \vdots & \vdots \\
\sum_{i=1}^{n} \mathbf{V}_i N_i(\xi_{1N}, \xi_{2N}, \xi_{3N}, \zeta_N) & = & \sum_{j=1}^{3} v_{mN_j} \mathbf{g}^j
\end{array} \tag{5.29}$$

where $\sum_{j=1}^{3} v_{m1_j} \mathbf{g}^j$ is derived from the three velocity images (indexing on j) at sample point 1 until sample point N. Notice that this formulation preserves the vector nature of the measurement so that the least squares solution may be broken into three smaller problems, one solution for each orthogonal direction - x,y and z. Specifically the y-direction solution would be written

$$\begin{array}{rcl}
\sum_{i=1}^{n} V_{y_i} N_i(\xi_{11}, \xi_{21}, \xi_{31}, \zeta_1) & = & \sum_{j=1}^{3} v_{m1_j} g_y^j \\
\sum_{i=1}^{n} V_{y_i} N_i(\xi_{12}, \xi_{22}, \xi_{32}, \zeta_2) & = & \sum_{j=1}^{3} v_{m2_j} g_y^j \\
\sum_{i=1}^{n} V_{y_i} N_i(\xi_{13}, \xi_{23}, \xi_{33}, \zeta_3) & = & \sum_{j=1}^{3} v_{m3_j} g_y^j \\
\vdots & \vdots & \vdots \\
\sum_{i=1}^{n} V_{y_i} N_i(\xi_{1N}, \xi_{2N}, \xi_{3N}, \zeta_N) & = & \sum_{j=1}^{3} v_{mN_j} g_y^j
\end{array} \tag{5.30}$$

Expanding the notation for one element,

$$\begin{array}{cccccc}
V_{y_1} N_1 & +V_{y_2} N_2 & \dots & +V_{y_6} N_6 & = & (v_{m1_1} g_y^1 + v_{m1_2} g_y^2 + v_{m1_3} g_y^3) \\
V_{y_1} N_1 & +V_{y_2} N_2 & \dots & +V_{y_6} N_6 & = & (v_{m2_1} g_y^1 + v_{m2_2} g_y^2 + v_{m2_3} g_y^3) \\
V_{y_1} N_1 & +V_{y_2} N_2 & \dots & +V_{y_6} N_6 & = & (v_{m3_1} g_y^1 + v_{m3_2} g_y^2 + v_{m3_3} g_y^3) \\
\vdots & \vdots & \vdots & \vdots & \vdots & \vdots \\
V_{y_1} N_1 & +V_{y_2} N_2 & \dots & +V_{y_6} N_6 & = & (v_{mN_1} g_y^1 + v_{mN_2} g_y^2 + v_{mN_3} g_y^3)
\end{array} \tag{5.31}$$

and rewriting in matrix form,

$$\begin{bmatrix} N_1 & N_2 & \dots & N_6 \\ N_1 & N_2 & \dots & N_6 \\ \vdots & \vdots & \vdots & \\ N_1 & N_2 & \dots & N_6 \end{bmatrix} \begin{Bmatrix} V_{y_1} \\ V_{y_2} \\ \vdots \\ V_{y_6} \end{Bmatrix} = \begin{Bmatrix} (v_{m1_1} g_y^1 + v_{m1_2} g_y^2 + v_{m1_3} g_y^3) \\ (v_{m2_1} g_y^1 + v_{m2_2} g_y^2 + v_{m2_3} g_y^3) \\ \vdots \\ (v_{mN_1} g_y^1 + v_{mN_2} g_y^2 + v_{mN_3} g_y^3) \end{Bmatrix} \tag{5.32}$$

so that the least squares solution is

$$\begin{aligned} [N]\{V_y\} &= \{v_{m_y}\}, \\ \{V_y\} &= \left[N^T N\right]^{-1} \left[N^T\right] \{v_{m_y}\}. \end{aligned}$$

This process is repeated for the x and z directions to complete the velocity field reconstruction. There are several structural advantages to this formulation. All the experimental error is collected together on the right hand side so that instead of a linear problem of the form

$$[N + \Delta N]\{V\} = \{v_m + \Delta v_m\}$$

the form is

$$[N]\{V\} = \{v_m + \Delta v_m\}.$$

This form has better numerical properties, typically better condition numbers for $\left[N^T N\right]^{-1}$ and the errors are not squared, $N^T N$. Additionally, the variances of the surface x, y, and z velocity components are now directly available and not coupled together as in the previous formulation. Finally, the direction cosines may be defined in a convenient local coordinate system, e.g. normal and tangential surface coordinates, so that the velocity field solution and variance estimates are more meaningful.

This completes the mathematical development of the various velocity reconstruction techniques. The next section utilizes experimental data to demonstrate the advantages of the contravariant method in reconstruction of the velocity field.

## 5.4 Experimental Evaluation

The velocity field reconstruction for two sets of velocity images illustrates the application and interpretation of the above analytic methods. Two sets of five velocity images of an

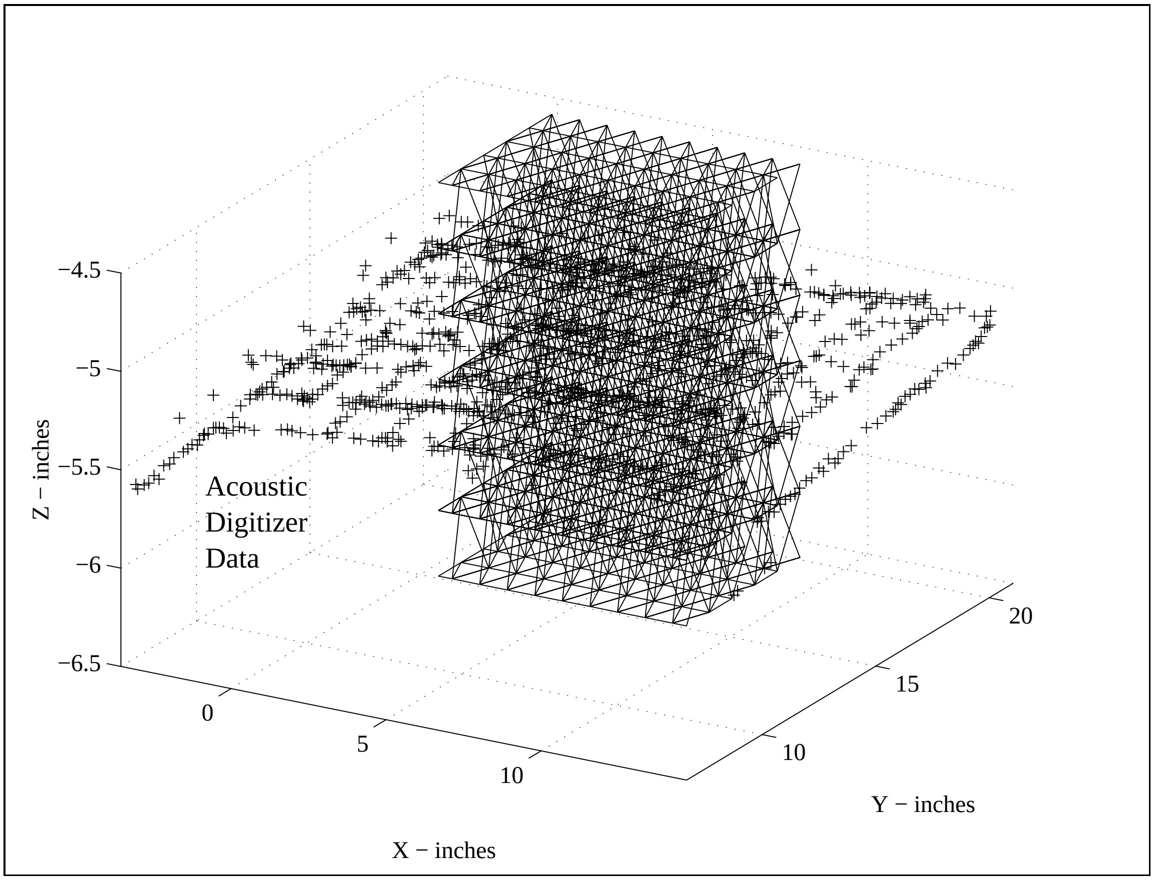

**Figure 5.7: Finite Element Volume with Digitizer Data**

excited plate are acquired. The reconstruction volume and plate digitizer data are depicted in Figure 5.7. The acoustic digitizer data of the actual surface demonstrates that the volume is located in the correct neighborhood. A view along the x-axis of Figure 5.8, shows that the plate essentially lies between the third and fourth "surface" layers (nodes 127-252). Thus the nodal solutions in this neighborhood should be of greatest interest to the researcher.

The full and partial least squares models are calculated. The full least squares model includes "intercept" nodal degrees of freedom. The partial least squares model excludes these parameters and determines the regression coefficients for the coupled, scalar model. The results of these calculations are tabulated in Table 5.7. This tables represent the results of reconstructing the velocity field from two different sets of experimental data. At first glance the partial models appear to be very reasonable solutions. When statistically tested against the full model, the hypothesis, $\beta_i = 0$, is rejected. This implies, once again, that the simple interpretation of the regressed coefficients as velocity components is not supported by the least squares solution: the regressed coefficients are biased. The least squares model

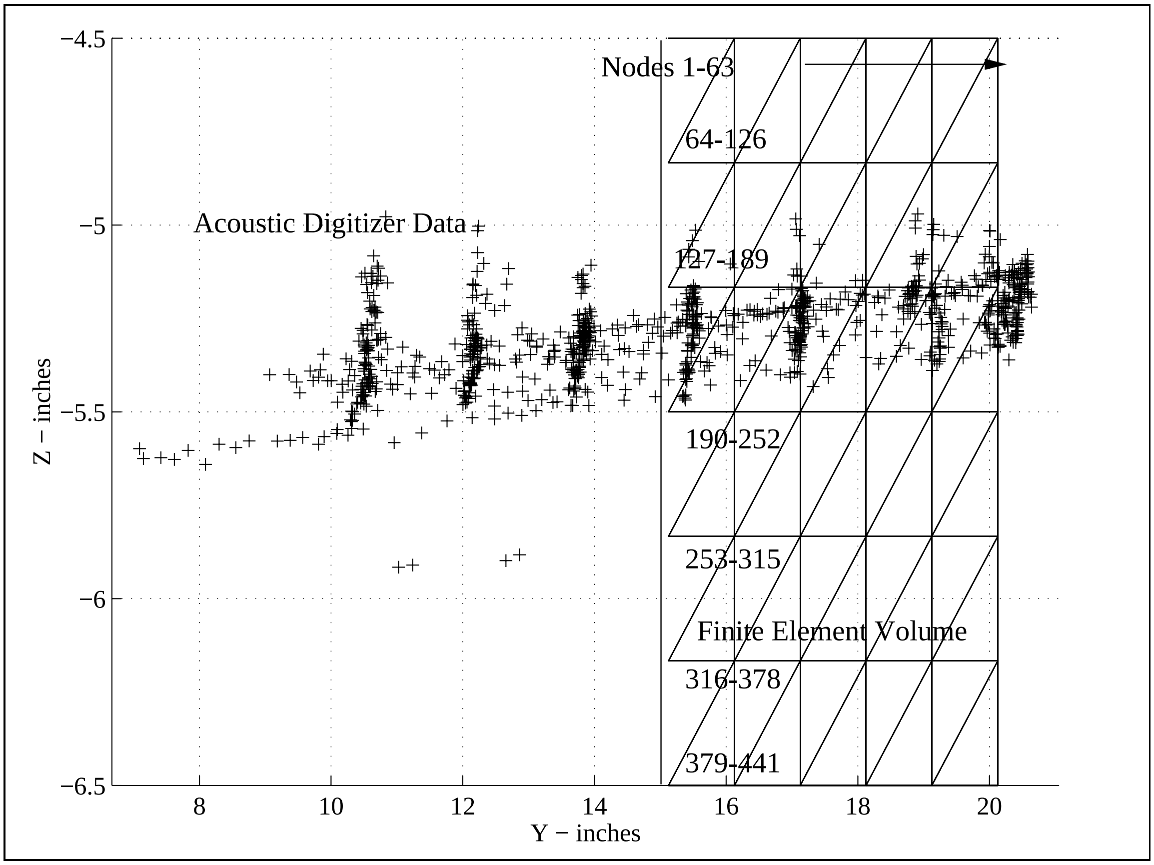

Figure 5.8: X Axis View of Experimental Finite Element Volume

Table 5.7: Experimental Velocity Reconstruction - Finite Element Volume Containing the Plate

| Plate Exp 1 | Part. L.S. | Full L.S. | Rel. L.S. | Cont. X | Cont. Y | Cont. Z |
|---|---|---|---|---|---|---|
| Nodal dof | 1323 | 1764 | 1323 | 441 | 441 | 441 |
| Sample pts | 19950 | 19950 | 15960 | 7980 | 7980 | 7980 |
| Std. Dev. | 0.0286 | 0.0250 | .0276 | 0.0518 | 0.0767 | 0.0188 |
| SSE | 16.28 | 12.48 | 12.17 | 21.42 | 46.95 | 2.82 |
| cond. no. | 7977 | 2.1326e+06 | 5504 | 245 | 245 | 245 |
| rcond. no. | 3.1483e-04 | 1.1942e-06 | 4.42e-04 | 0.0023 | 0.0023 | 0.0023 |

| Plate Exp 2 | Part. L.S. | Full L.S. | Rel. L.S. | Cont. X | Cont. Y | Cont. Z |
|---|---|---|---|---|---|---|
| Nodal dof | 1323 | 1764 | 1323 | 441 | 441 | 441 |
| Sample pts | 19950 | 19950 | 15960 | 7980 | 7980 | 7980 |
| Std. Dev. | 0.0378 | 0.0367 | 0.0331 | 0.0792 | 0.1102 | 0.0147 |
| SSE | 28.44 | 24.50 | 17.4741 | 50.03 | 98.88 | 1.72 |
| cond. no. | 1.336e+04 | 3.8586e+06 | 5107 | 245 | 245 | 245 |
| rcond. no. | 2.3900e-04 | 8.015e-07 | 6.1021e-04 | 0.0023 | 0.0023 | 0.0023 |

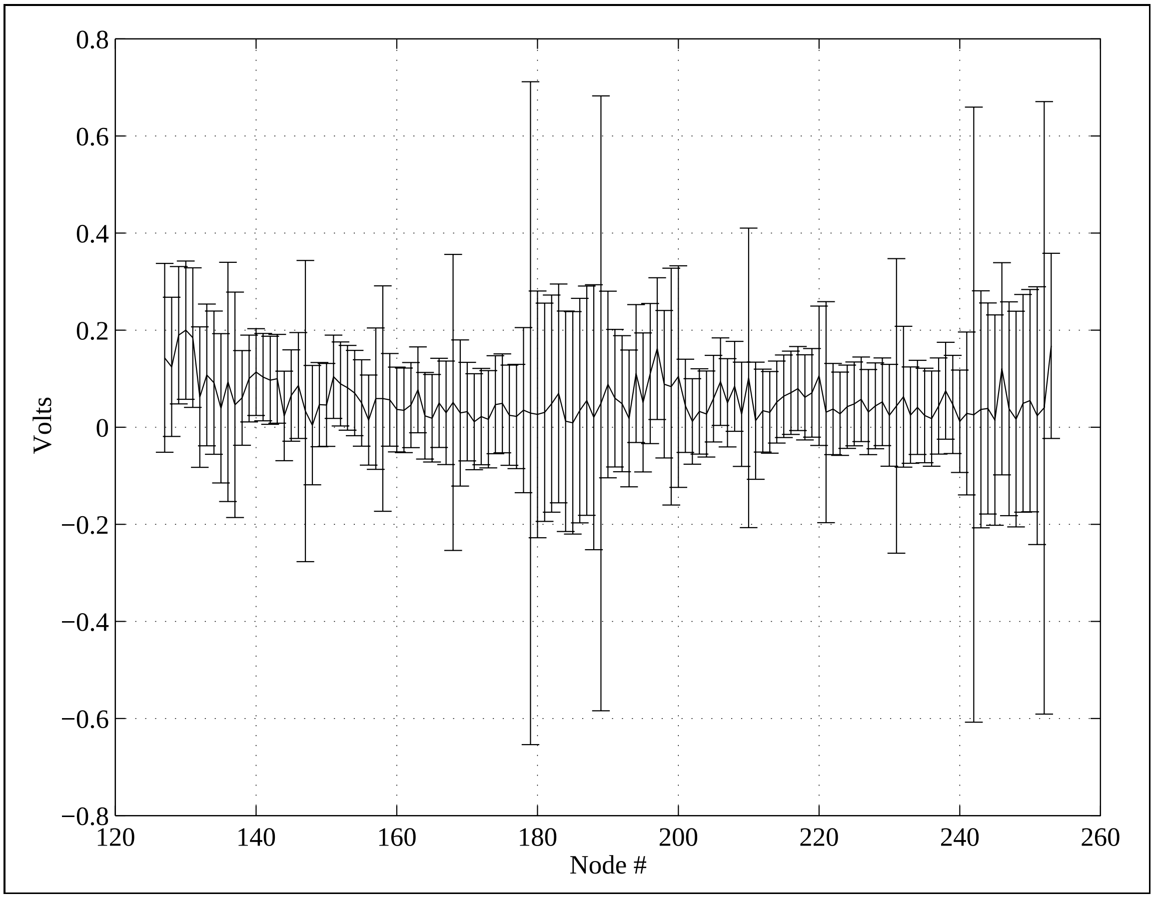

**Figure 5.9: Experiment 1 X Nodal Values**

is "scalar" in that the model predicts the laser velocity images well, but not necessarily the surface velocity. Figures 5.9, 5.10, 5.11 depict the regressed velocity coefficients with error bounds for nodes 127-252, the "surface" nodes where the plate is expected to be. These figures demonstrate the superior quality of the "out-of-plane" solution when compared with the "in-plane" solution. The confidence bounds of the in-plane nodal variables are too large to be useful in an engineering sense, i.e. calculating forces, strains, and stresses. Similar results are found in each experimental case and method. A quick glance at the residual plots for these regressions, Figure 5.12, illustrate the lower residuals for the full least squares model and the variation of the residual magnitudes by image. The standard deviation of the image by image is shown in Table 5.4. This variation of the standard deviation among images is clearly a sign that the best set of SLDV pose estimates for the velocity images as a whole has not been found, only the best estimate for each viewpoint.

Since the original intention of the reconstruction process was to determine the struc-

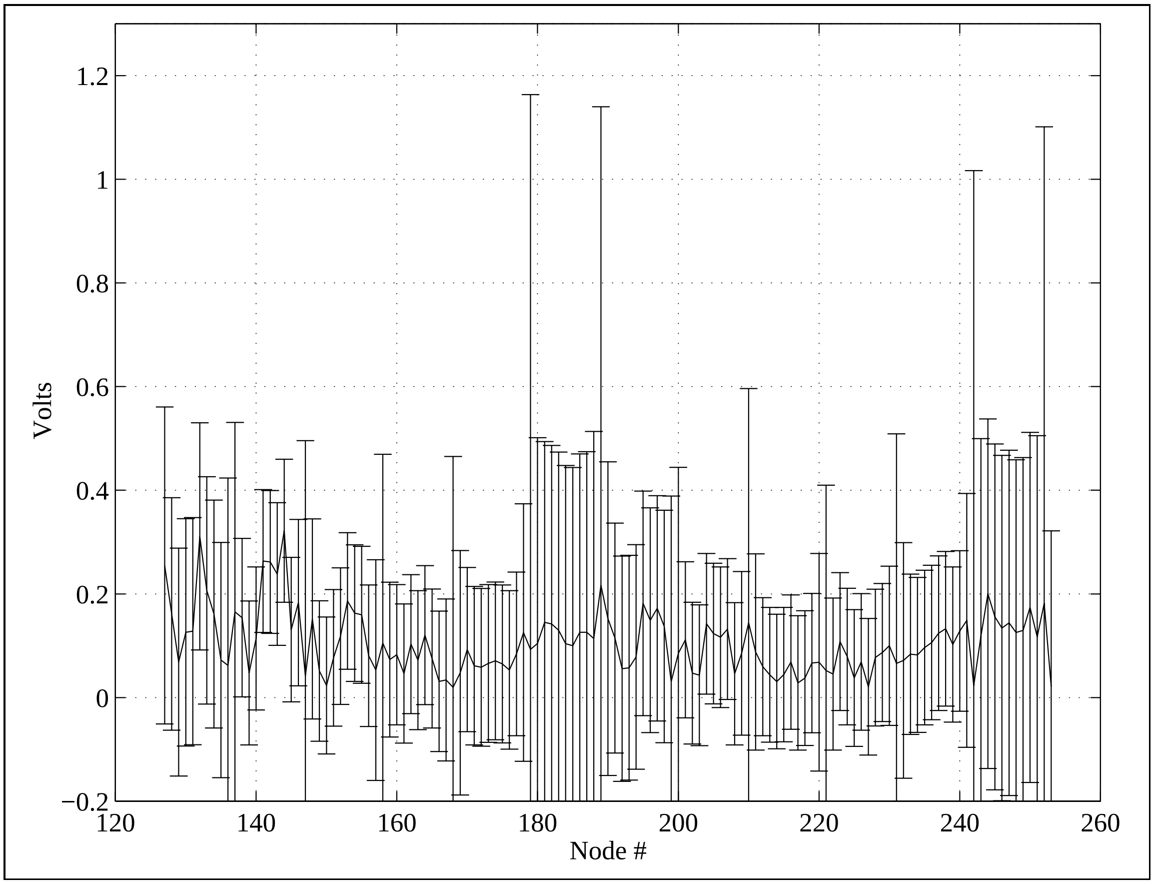

Figure 5.10: Experiment 1 Y Nodal Values

| Exp 1 Images | 1 | 2 | 3 | 4 | 5 |
|---|---|---|---|---|---|
| STD -Full L.S. | 0.0196 | 0.2460 | 0.0322 | 0.0214 | 0.0243 |
| STD -Partial L.S. | 0.0235 | 0.0261 | 0.0310 | 0.0276 | 0.0299 |
| STD -Rel. L.S. | 0.0241 | 0.0303 | 0.0212 | 0.0327 | NA |
| Exp 2 Images | 1 | 2 | 3 | 4 | 5 |
| STD -Full L.S. | 0.0572 | 0.0241 | 0.0325 | 0.0201 | 0.0286 |
| STD -Partial L.S. | 0.0568 | 0.0261 | 0.0433 | 0.0199 | 0.0281 |
| STD -Rel. L.S. | 0.0241 | 0.0303 | 0.0212 | 0.0327 | NA |

Table 5.8: Variation of Residuals by Image

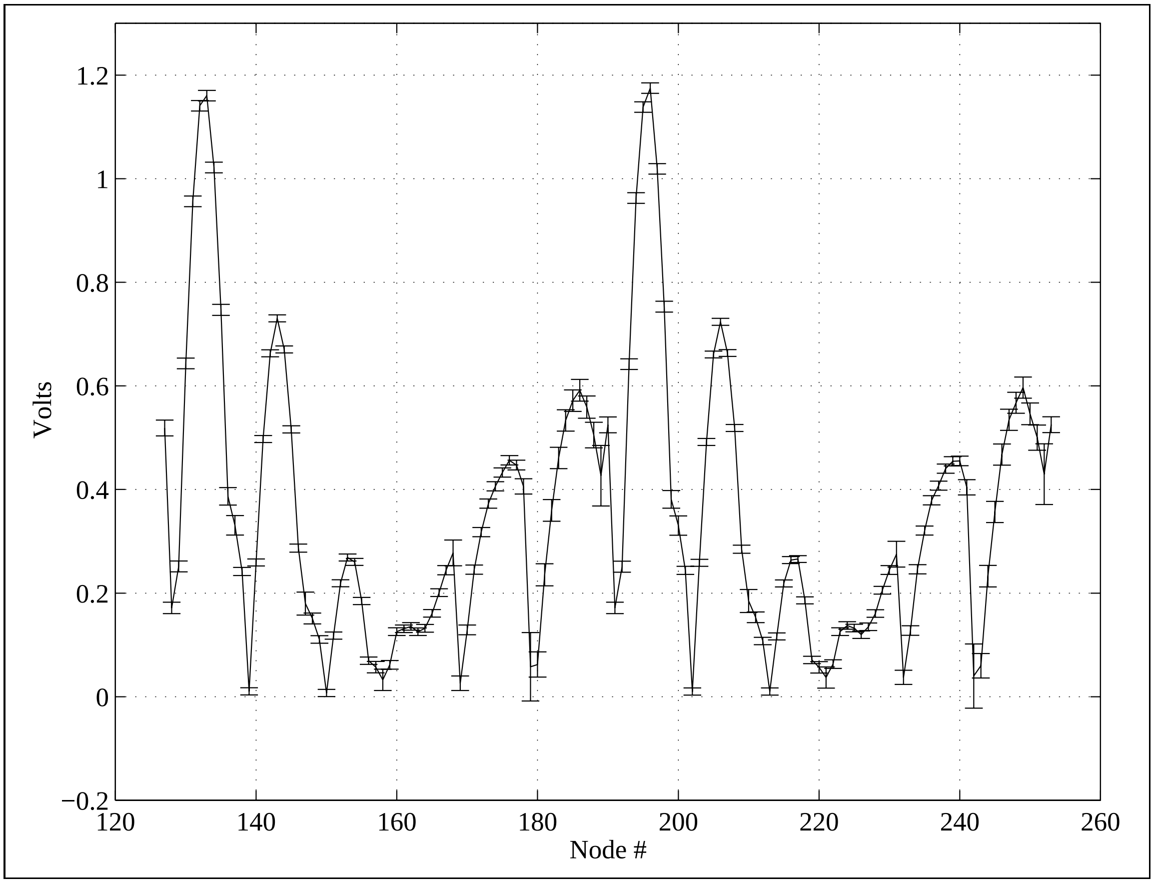

Figure 5.11: Experiment 1 Z Nodal Values

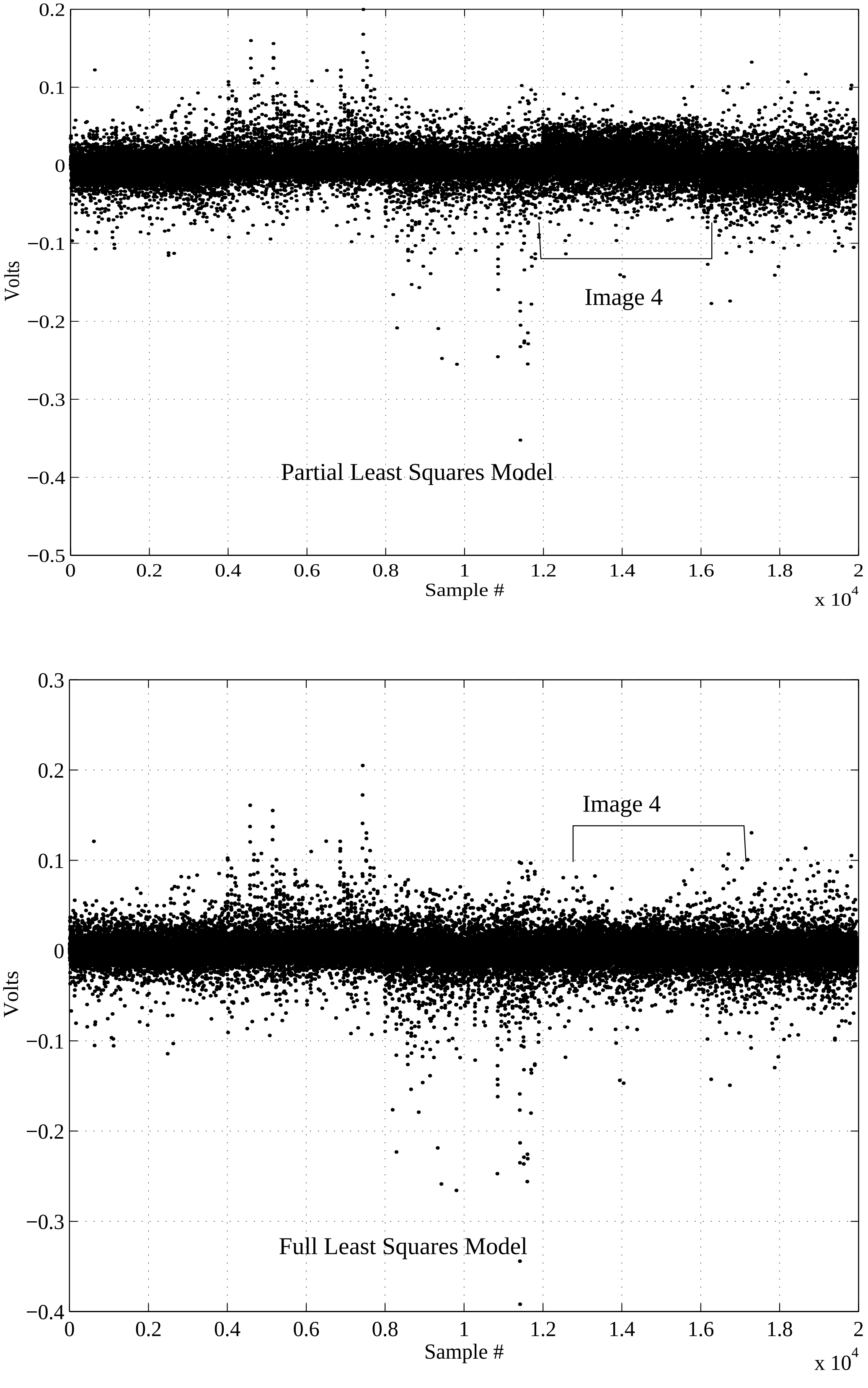

**Figure 5.12: Experiment 1 Residuals**

ture's surface velocity, the model should reflect this intention. The contravariant method solves the velocity field in three independent, orthogonal directions, preserving the "vector" structure of the velocity field consistent with the surface motion assumptions. The contravariant method essentially is a two step process where the velocity vectors at the sample points in the finite element volume are recovered and then used as vector "measurements" for the velocity field reconstruction. This method is a synthesis and extension of Dominquez's and Montgomery's SLDV research([12, 40] with the research in holographic interferometry, specifically Schumann's work[50]. The results of the contravariant method, the last three columns of Table 5.7, show an excellent fit for the "Z" direction solution and significantly higher standard deviations for the "in-plane" motions. When compared with the other least squares models, the effect of the coupled solution is clear: the out-of-plane estimates have greater variance so that the in-plane variance estimates are lower. The regressed z-velocity nodal values, computed with the contravariant method, are shown in Figure 5.13 with errorbars. These nodal values represent the velocity field solution in the neighborhood of the actual surface. The out-of-plane velocity solution does not vary through the thickness of the plate which is constistent with Love's thin-shell theory. Figure 5.14 shows the out-of-plane velocity solution for the plate. In short, the contravariant method provides a way to distinguish the accuracy of the structure's surface velocity components. The relevant matrix condition numbers, 0.0023 vs. 4.4e-04, suggest that the contravariant method is numerically less susceptible to error magnification. The contravariant method is significantly better than the "scalar" approach. There is now supporting analysis for "discarding" the in-plane solutions and just using the out-of-plane velocity field estimate. This approach is consistent with Blotter's research[5] which used only an out-of-plane solution coupled plate theory to evaluate structural energy and powerflow. The combination of the contravariant method out-of-plane solution with thin-shell theory is the path for future research with SLDV velocity images.

## 5.5 Summary

The research goal in this chapter is to reconstruct the velocity field on a family of surfaces in the neighborhood of the actual surface. First, methods adopted from holographic interferometry were combined with SLDV computer vision velocity images to reconstruct the

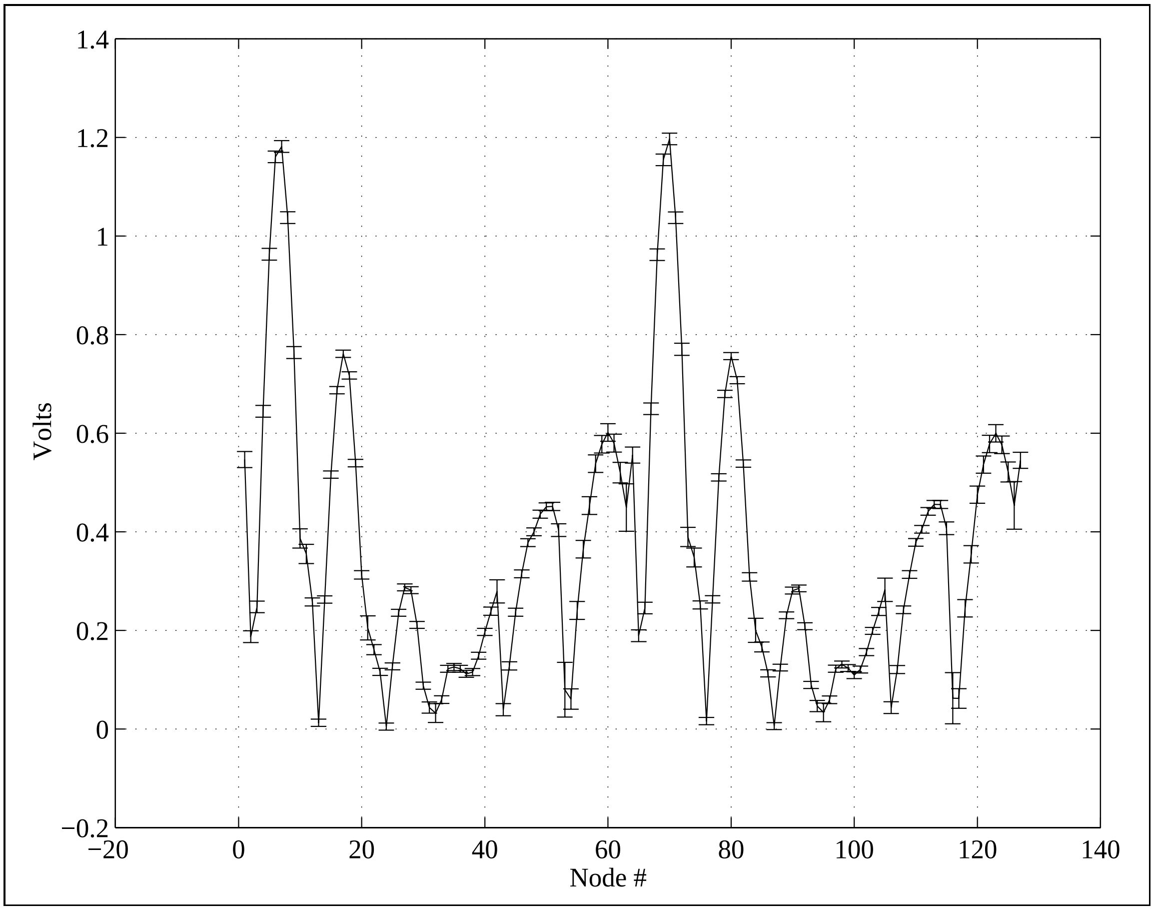

**Figure 5.13: Experiment 1 Z Nodal Velocities, Contravariant Method**

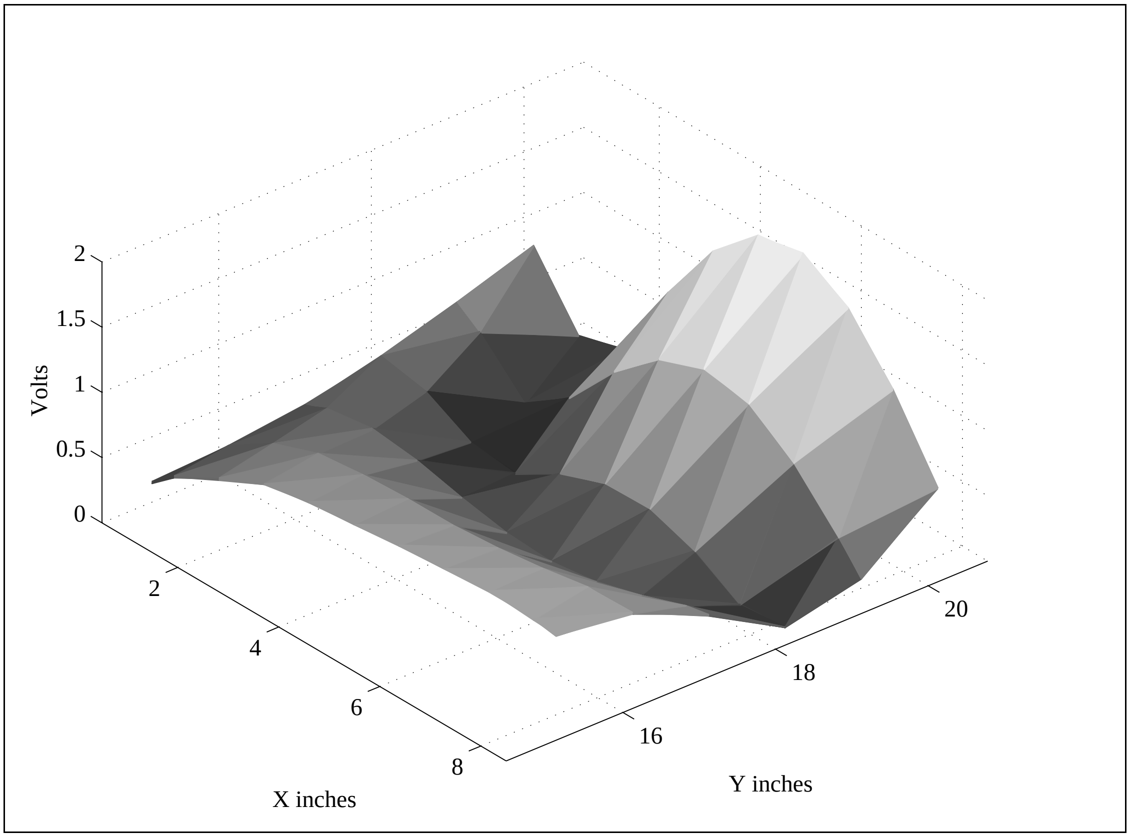

Figure 5.14: Experiment 2 - Z Nodal Velocities, Contravariant Method

velocity at a point. In this investigation the effect of the matrix condition number played an important role in determining which method would result in the best reconstructed velocity vector. For the experiments performed, a combination of relative and absolute velocity measurements generated from the SLDV velocity images had the best condition number. This fact was employed when the reconstruction procedure was expanded to recovery of the velocity field over the family of surfaces. Each reconstruction method was revisited and examined. The result of this analysis showed the contravariant method to be the superior approach because the contravariant method permitted a decoupled, orthogonal solution to the velocity reconstruction problem. Additionally, the contravariant method had the best condition number (for the relevant matrices) which minimizes the potential error magnification. In short, these procedures improve the velocity reconstruction process.

# Chapter 6

# Conclusions and Recommendations

The goal of this research is to improve the velocity reconstruction process with computer vision. This goal has been achieved through the development and use of a computer vision model for the SLDV and the treatment of SLDV data as *images*. The SLDV computer vision model - a projective camera - paved the way for the automation of the SLDV pose procedure and the extension of analytic techniques, developed for laser holographic interferometry, to reconstruction of velocity fields from SLDV velocity images. These new procedures offer significant improvements to the velocity reconstruction process by providing better SLDV pose estimates and an orthogonally decomposed velocity field reconstruction procedure which is decoupled from the surface geometry.

## 6.1 Conclusions

The automated SLDV pose calculation is the first, improved step in the velocity reconstruction procedure. The foundation of the SLDV pose automation is the development of the SLDV projective camera model. This model demonstrated that the SLDV preserves projective invariants, e.g. cross-ratios. Next a calibration object was developed with SLDV detectable, projectively invariant features - planar conics. The recovery of bitangent points among these features in both the object and image spaces leads to more precise and accurate input data for previously developed SLDV pose algorithms. This automated pose procedure was shown to be repeatable and the estimated pose was independently verified with acoustic digitizer data. When the automated procedure was compared with previous pose procedures, the new process was superior, less that $\frac{1}{2}$ DAC step standard deviation, and was only limited by the operational parameters of the equipment. Specifically, the precision of the IOtech 12bit digital to analog conversion board is the limiting factor in the pose estimates. This new capability ensures consistent, accurate and precise pose estimates for post-processing of SLDV velocity images.

The fusion of multiple velocity images by using concepts and techniques borrowed from laser holgraphic analysis and the developed SLDV computer vision model is a significant enhancement to the last step in the velocity field reconstruction process. First the SLDV computer vision model permitted the precise determination of velocity image points which correspond to object points on the structure's surface (or family of surfaces). With velocity image points of an object point, absolute and relative velocity measurements, borrowed from the holographic interferometry, were developed and investigated to determine the best way to reconstruct the velocity vector at a point. The best velocity vector is recovered with the set of velocity measurements which have the best matrix condition number. Once found, this set of velocity measurements point the way for combining the velocity images through a least squares field solution over the discretized domain - the triangular, prismatic finite elements in the neighborhood of the structure's surface. This field solution may be decomposed into three, smaller orthogonal least squares solutions by formulation of the least squares problem with contravariant base vectors at each sample point. This contravariant method also depends upon the object/image point correspondences from the computer vision model to determine interpolated velocity measurements for the least squares velocity reconstruction. Not only does this contravariant method provide a decoupled solution whose matrices have better condition numbers than previous formulations, the method is adaptable to the local surface coordinate system which is the appropriate choice for comparisons with thin shell finite element models. In short the foundation has been developed for the future research with SLDV based velocity fields.

## 6.2 Recommendations

The experience gained during this research has produced not only results, but also issues which should be addressed in future research. These issues are improving the data acquisition, augmenting the pose automation, and velocity field reconstruction validation. The following paragraphs detail specific recommendations for future research.

The velocity data acquisition has several outstanding topics which should be addressed: statistical testing of the sinusoidal data fitting, multiple frequency data fitting, and phase error. The current approach to fitting the sinusoidal data is to use a full least squares model with an intercept term and then discard the intercept term as insignificant. This process should be modified to fit the data with and without the intercept term and statistically test the hypothesis that the intercept term is insignificant. If the intercept term is insignificant, then the regression coefficients from the partial model, not the full model, should be used in the downstream data processing. The difference in magnitude may not be great, but the phase is likely to change. This is the second, related issue, phase error. How does the phase error propogate throught the velocity reconstruction process? Has the phase error been attributed to the "registration error"? This is an important consideration and could be mitigated by fitting the excitation frequency and higher harmonics. This more complete frequency model could be incrementally examined to see if the harmonic terms are statistically significant. Investigating these issues will result in even more confidence in the reconstructed velocity field.

The SLDV pose automation should be extended in three ways. First the calibration object should be expanded with another plane of circular features. The added plane would enhance the pose process by adding more constraints for the non-linear pose optimization routines. Experience has shown that these non-linear pose routines need good starting points in order to find an accurate solution. In this research the starting points were provided by the acoustic digitizer data, but an additional plane of features should help eliminate the necessity of acoutic digitizer data. Secondly, a 16bit D/A board should be used to direct the SLDV mirrors. The additional precision will directly improve the pose estimates. Finally, the projective invariance of the bitangent points should be exploited so that the SLDV pose estimate at one position includes the observations from all the other viewpoints. This approach will result in the best overall pose estimate and will improve velocity field reconstruction process, specifically, the residuals among the differing images should be negligible.

Finally, new innovative techniques must be developed to verifiy the reconstructed velocity field. Methods from computational fluid dynamics - conservation of mass and momentum - represent basic approaches which should be applied to the reconstructed velocity field. Additionally the reconstructed velocity field (over a volume) may be examined for features like minimum kinetic energy surfaces to see if these features correspond to the actual surface. Successful demonstration of this idea would further validate the reconstructed velocity field. Experimental paths in the holographic interferometry of opaque bodies should be followed to reconfirm the experimental results with SLDV data. For example, thin-shell theory, e.g. Love's theory, should be exploited to provide an independent verification of the reconstructed velocity field. For example, strain gage data could be directly compared with the derivative of a single, registered velocity image; this would exploit the differential structure that exists between two surfaces, in this case the thin-shell surface and the image surface. These improvements could lead to an everyday, experimental tool for validating finite element models and determining experimental, dynamic strains.

# Bibliography

[1] Jeffry J. Abel. Three-dimensional velocity extraction using laser doppler vibrometry. Master's thesis, Virginia Polytechnic Institute and State University, Blacksburg, Virginia, February 1993.

[2] Simon L. Altmann. *Rotations, Quaternions, and Double Groups.* Clarendon Press, Oxford, 1986.

[3] Frank Ayers. *Schaum's Outline of Theory and Problems of Projective Geometry.* McGraw-Hill, New York, 1986.

[4] Michel Bernadou. *Finite Element Mehtods for Thin Shell Problems.* John Eiley and Sons, Chichester, New York, 1996.

[5] Jonathan D. Blotter. *Structural Energy and Powerflow Using a Scanning Laser Doppler Vibrometer.* PhD thesis, Virginia Polytechnic Institute and State University, Blacksburg, Virginia, July 1996.

[6] Boubakeur Boufama, Roger Mohr, and Luce Morin. Automatic and accurate object positioning using targets. In *Proceedings of Europe-China Workshop on Geometrical Modeling and Invariants for Computer Vision*, pages 222–229, 1995.

[7] Jack Chou and M. Kamel. Finding the position and orientation of a sensor on a robotic manipulator using quaternions. *The International Journal of Robotics Research*, 10(3):240–254, June 1991.

[8] M. Dikmen. *Theory of Thin Elastic Shells.* Pitman Advanced Publishing Program, Marshfield Massachusetts, 1982.

[9] Jean-Pierre Djamdji, Albert Bijaoui, and Roger Maniere. Geometrical registration of images: the multiresolution approach. *Photogrammetric Engineering and Remote Sensing*, 59(5):645–653, May 1993.

[10] C T J Dodson and T Poston. *Tensor Geometry.* Pitman Publishing Limited, 39 Parker St, London, 1977.

[11] Christopher A. Doktor. Developement of a statistical method for validating esdm strain-field output. Master's thesis, Virginia Polytechnic Institute and State University, Blacksburg, Virginia, December 1995.

[12] Jose Carlos Lopez Dominquez. *Reconstruction of 3-D Structural Dynamic Response Fields: An Experimental, Laser-Based Approach with Statistical Emphasis.* PhD thesis, Virginia Polytechnic Institute and State University, Blacksburg, Virginia, August 1994.

[13] L.E. Drain. *The Laser Doppler Technique.* John Wiley and Sons, Ltd., Chichester, United Kingdom, 1980.

[14] Clive L. Dym. *Introduction to the Theory of Shells.* Hemisphere Publishing Corporation, New York, 1990.

[15] J. Barry Fallon. *Improving the Kinematic Control of Robots with Computer Vision.* Phd, Virginia Polytechnic Institute and State University, Blacksburg, Virginia, July 1995.

[16] Olivier Faugeras. *Three-Dimensional Computer Vision.* The MIT Press, Cambridge, Massachusetts, 1995.

[17] George Forsythe and Cleve B. Moler. *Computer Solution of Linear Algebraic Systems.* Prentice Hall, Englewood Cliffs, New Jersey, 1967.

[18] P. Fua and Y.G. Leclerc. Registration without correspondences. *IEEE*, 19(94):121–128, December 1994.

[19] Sanjib K. Ghosh. *Analytic Photogrammetry.* Pergamon Press, New York, 1988.

[20] A. L. Gol'denveizer. *Theory of Elastic Thin Shells.* Pergamon Press, New York, 1961.

[21] Herbert Goldstein. *Classical Mechanics.* Addison-Wesley Publishing Company, Reding, Massachusetts, 1950.

[22] Gene H. Golub and Charles F Van Loan. *Matix Computations.* The John Hopkins University Press, Baltimore and London, 1989.

[23] William C. Graustein. *Introduction to Higher Geometry.* MacMillian Company, New York, 1930.

[24] Patrick Gros. How to use the cross-ratio to compute projective invariants from two images. In Joseph L. Mundy and Andrew Zisserman, editors, *Applications of Invariance in Computer Vision*, pages 107–143. Springer-Verlag, 1994.

[25] R. M. Haralick, H Joo, C. Lee, X Zhuang, V.G. Vaidya, and M. B. Kim. Pose estimation from corresponding point data. *IEEE Transactions on Systems, Man and Cybernetics*, 19(6):1426–1446, December 1989.

[26] R.M. Haralick and H. Joo. 2d-3d pose estimation. In *Proceedings of the Ninth International Conference on Pattern Recognition*, pages 385–391, 1988.

[27] IOtech Inc., Cleveland, Ohio. *Instruction Manual for DAC488/2*, revision 2.0 edition, November 1989.

[28] IOtech Inc., Cleveland, Ohio. *ADC488 Instruction Manual*, revision 1.1 edition, January 1990.

[29] Walter Jaunzemis. *Continuum Mechanics.* MacMillan Series in Applied Mechanics. MacMillan Co., New York, 1967.

[30] Richard A. Johnson and Dean W. Wichern. *Applied Multivariate Statistical Analysis.* Prentice Hall, Englewood Cliffs, New Jersey, 1996.

[31] Jan J. Koenderink. *Solid Shape.* The MIT Press, Cambridge, Massachusetts, 1990.

[32] Thomas Kreis. *Holographic Interferometry*, volume 1 of *Optical Metrology.* Akademie Verlag, Berlin New York, 1996.

[33] Brian Lindholm. Three dimensional position registration of a laser doppler vibrometer. In *Proceedings of the 14th International Modal Analysis Conference,IMAC XIV*, pages 830–836, 1996.

[34] Brian E. Lindholm. *A Bayesian Statistics Approach to Updating Finite Element Models with Frequency Response Data*. PhD thesis, Virginia Polytechnic Institute and State University, Blacksburg, Virginia, August 1996.

[35] Martin Lipschutz. *Schaum's Outline of Theory and Problems of Differential Geometry*. McGraw-Hill, New York, 1969.

[36] T. MAtsumoto, K. Iwata, and R. Nagata. Measuring accuracy of three dimensional displacements in holographic interferometry. *Applied Optics*, 12(5):961–967, May 1973.

[37] Leonard Meirovitch. *Elements of Vibration Analysis*. McGraw-Hill Publishing Company, New York, 1986.

[38] Leonard Meirovitch. *Principles and Techniques of Vibrations*, chapter 1, page 14. Prentice-Hall, Inc., Upper Saddle River, New Jersey, 1997.

[39] David Montgomery and Robert L. West. Position registration of scanning lasers for experimental spatial dynamics modeling. In *Proceedings of the 20th ASME Design Automation Conference*, pages 830–836, 1994.

[40] David E. Montgomery. *Modeling and Visualization of Laser-Based Three-Dimensional Experimental Spatial Dynamic Response*. PhD thesis, Virginia Polytechnic Institute and State University, Blacksburg, Virginia, November 1994.

[41] Joseph L. Mundy and Andrew Zisserman. Appendix - projective geometry for machine vision. In Joseph L. Mundy and Andrew Zisserman, editors, *Geometric Invariance in Computer Vision*, chapter 23, pages 463–519. MIT Press, 1992.

[42] Joseph L. Mundy and Andrew Zisserman. Introduction - towards a new framework for vision. In Joseph L. Mundy and Andrew Zisserman, editors, *Geometric Invariance in Computer Vision*, chapter 1, pages 1–39. MIT Press, 1992.

[43] Ometron, London, England. *VPI Sensor Operator's Manual*, 1987.

[44] R.Lyman Ott. *An Introduction to Statistical Methods and Data Analysis*. Duxbury Press, Belmont, California, 1993.

[45] Michael A. Penna and Richard R. Patterson. *Projective Geometry and Its Applications to Computer Graphics*. Prentice-Hall, Englewood Cliffs, New Jersey, 1986.

[46] X. Pennec and J. P. Thirion. Validation of 3-d registration methods based on points and frames. In *Proceedings of the Fifth International Conference on Computer Vision*, volume 1003, pages 59–62. IEEE Computer Society Press, 1995.

[47] William H. Press, Brian P. Flannery, Saul A. Teukolsky, and William T. Vettering. *Numerical Recipies The Art of Scientific Computing.* Cambridge University Press, Cambridge, Massachusetts, 1986.

[48] C. A. Rothwell, A. Zisserman, C. I. Marinos, D. A. Forsyth, and J. L. Mundy. Relative motion and pose from arbitrary plane curves. *Image and Vision Computing*, pages 250–262, 1992.

[49] Pierre Samuel. *Projective Geometry.* Undergraduate Text in Mathematics. Springer Verlag, New York, 1988.

[50] W. Schumann and M. Dubas. *Holographic Interferometry*, volume 16 of *Springer Seris in Optical Sciences.* Springer-Verlag, Berlin, Heidelberg, New York, Tokyo, 1979.

[51] W. Schumann, J.-P. Zuercher, and D. Cuche. *Holography and Deformation Anaylysis*, volume 46 of *Springer Seris in Optical Sciences.* Springer-Verlag, Berlin, Heidelberg, New York, Tokyo, 1985.

[52] Joseph E. Shigley and Larry D. Mitchell. *Mechanical Engineering Design.* McGraw-Hill Series in Mechanical Engineering. McGraw-Hill Book Co., New York, fourth edition, 1983.

[53] Chester C. Slama. *Manual of Photogrammetry.* American Society of Photogrammetry, Falls Church, Virginia, fourth edition, 1980.

[54] Werner Soedel. *Vibrations of Shells and Plates.* Marcel Dekker, Inc, New York, New York, second edition, 1982.

[55] Michael Allan Stafne. An experimental evaluation of the experimental spatial dynamics modeling technique. Master's thesis, Virginia Polytechnic Institute and State University, Blacksburg, Virginia, May 1998.

[56] Renzo Tonin and David A. Bies. Analysis of 3-d vibrations from time averaged holograms. *Applied Optics*, 17(23):3713–3721, December 1978.

[57] Renzo Tonin and David A. Bies. General theroy of time averaged holography for the study of three dimensional vibrations at a single frequency. *Journal of the Optical Society of America*, 68(7):924–931, July 1978.

[58] Charles M. Vest. *Holographic Interferometry.* John Wiley and Sons, New York, 1979.

[59] V.V. Vovozhilov. *The Theory of Thin Shells.* P. Noordhoff Ltd., Groningen, Netherlands, 1959.

[60] H. Weyl. *The Classical Groups and their Invariants.* Princeton University Press, Princeton, New Jersey, second edition, 1946.

[61] Xiandi Zeng. *The Esitmation and Statistical Inferences of the Position and Orientation of a Scanning Laser Doppler Vibrometer.* Phd, Virginia Polytechnic Institute and State University, Blacksburg, Virginia, November 1994.

# Appendix A

# Research Code and Data Files

This appendix describes the location of data files and the procedure for using the files to recreate the results in this research. The sections follow the same order as the dissertation, pose automation followed by velocity field reconstruction.

## A.1 Pose Automation

The pose automation process consists of three steps: SLDV scanning, bitangent point recovery, and pose estimation. For each step, the location of input files, output files and Matlab m-files are listed. The procedures for using the commmands are described.

### A.1.1 SLDV Scanning

SLDV pose automation begins with scanning the calibration object. To generate a scanlist ( a list of left-right, up-down DAC pairs), the SLDV laser beam must be directed to the center of each calibration object's circular features and the DAC step values recorded in a file. Moving the SLDV laser beam is initiated with the command *ESDM*. A graphical user interface with two slider bars appears on the screen. The two slider bars are used to direct the laser beam toward each circular center. The DAC coordinates of the circular feature centers are place in a file, Scan6pt.default. The command *scan6pt* reads this file and generates ScanList.default, a file which contains the DAC coordinate pairs to be scanned by the SLDV. The data acquisition software command *goscan* reads the ScanList.default file and and acquires velocity data across the four circular features.

### A.1.2 Bitangent Point Recovery

Once the coasre SDLV scanning is complete, the Matlab command *fourellipse* is executed. This command prompts for the velocity data file and the scanlist file. These two files are *goscan*'s output files, vel.default and Scanlist.default renamed without extensions. The *fourellipse* Matlab command calculates the coarse conic approximations and generates a new refined scanlist for the fine conic fitting procedure. The output file generated is ScanList.default. Again *goscan* is executed and another set of velocity data is acquired. The output file is vel.default which contains the velocity data. The vel.default and ScanList.defalt files are renamed and serve as input files to the Matlab command *ellipsereg*, the fine conic fitting procedure. The output of *ellipsereg* is a file ABCDEF containing the coefficients for the four ellipses which are images of the circular features. The command *tangentpts* reads ABCDEF and produces an ouput file BITANGE48PT which lists the recovered bitangent points. The *tangentpts* command also produces plots to assist in matching bitangent image points with the corresponding object points and generating the 16 bitangent points needed for registration.

### A.1.3 Pose Estimation

The pose estimation algorithm requires an input registration file containing corresponding object and image points. The image points are the 16 bitangent points selected from the *tangentpts*' output file. The output file units are DAC steps and must be converted to angles by the command *dac2reg* which reads a SLDV parameter file "ometron2" and returns the converted DAC coordinates in a form suitable for pasting into the registration files. The XYZ object coordinates are listed in Table 4.1. Using the column paste function, the converted DAC coordinates may be placed into the registration file and the command *regkey1i* used to determine the SLDV pose. To assist the pose algorithm and help independently verify the SLDV pose estimate, the acoustic digitizer is used to collect point data. Three points on the SLDV [55] are digitized ( order - low med high ) and the four corners on the calibration object ( order lower left corner, then counter clock-wise ). Each point is digitized seven times before moving onto the next point. The resulting file contains 49 points. The Matlab command *seven* is used to determine the structure to laser transformation which may be place in the registration file to provide a good starting point for the non-linear pose estimation routine.

### A.1.4 Data Files

The location of the data files for each research section are listed below.

#### A.1.4.1 Bitangent Point Repeatability

The data files for Section 4.6.1 are listed below.

| Velocity File | ScanList File |
|---|---|
| vel48pt_23jan_pos1AA | scanlist48pt_23jan_pos1AA |
| vel48pt_23jan_pos1BB | scanlist48pt_23jan_pos1BB |
| vel48pt_23jan_pos1CC | scanlist48pt_23jan_pos1CC |
| vel48pt_23jan_pos1DD | scanlist48pt_23jan_pos1DD |
| vel48pt_23jan_pos1EE | scanlist48pt_23jan_pos1EE |
| vel48pt_23jan_pos1FF | scanlist48pt_23jan_pos1FF |
| vel48pt_23jan_pos1GG | scanlist48pt_23jan_pos1GG |
| vel48pt_23jan_pos1HH | scanlist48pt_23jan_pos1HH |
| vel48pt_23jan_pos1II | scanlist48pt_23jan_pos1II |

`PATH=/usr/people/coedah/RESEARCH/TASK_II/LASER_DATA/NOT_MOVED`

#### A.1.4.2 Independent Verification

The data files for Section 4.6.3 are listed below.

| Velocity File | ScanList File | Acoustic File |
|---|---|---|
| vel14jan_pos0 | scanlist14jan_pos0 | pos0.sev |
| vel14jan_pos1 | scanlist14jan_pos1 | pos1.sev |
| vel14jan_pos2 | scanlist14jan_pos2 | pos2.sev |
| vel14jan_pos3 | scanlist14jan_pos3 | pos3.sev |
| vel14jan_pos4 | scanlist14jan_pos4 | pos4.sev |
| vel14jan_pos5 | scanlist14jan_pos5 | pos5.sev |
| vel14jan_pos6 | scanlist14jan_pos6 | pos6.sev |
| vel14jan_pos7 | scanlist14jan_pos7 | pos7.sev |
| vel14jan_pos8 | scanlist14jan_pos8 | pos8.sev |

`PATH=/usr/people/coedah/RESEARCH/TASK_I/LASER_DATA/POS_MOVED`

PATH=/usr/people/coedah/RESEARCH/TASK_I/ACOUSTIC_DATA/jan14

#### A.1.4.3 Comparison of Pose Methods

The data files for Section 4.6.4 are listed below.

| Registration File | Method | Note |
|---|---|---|
| LDVp1_data_dhc.reg | 1 | regkey1i |
| LDVp2_data_dhc.reg | 1 | regkey1i |
| LDVp3_data_dhc.reg | 1 | regkey1i |
| LDVp4_data_dhc.reg | 1 | regkey1i |
| reg1.79HZ3.cal | 2 | regkey1m |
| reg2.79HZ3.cal | 2 | regkey1m |
| reg3.79HZ3.cal | 2 | regkey1m |
| reg4.79HZ3.cal | 2 | regkey1m |
| reg5.79HZ3.cal | 2 | regkey1m |
| reg6.79HZ3.cal | 2 | regkey1m |
| reg7.79HZ3.cal | 2 | regkey1m |
| reg9.79HZ3.cal | 2 | regkey1m |
| reg10.79HZ3.cal | 2 | regkey1m |
| reg12.79HZ3.cal | 2 | regkey1m |
| cmm_pos1.reg | 3 | regkey1i |
| cmm_pos2.reg | 3 | regkey1i |
| cmm_pos3.reg | 3 | regkey1i |
| cmm_pos4.reg | 3 | regkey1i |
| cmm_pos5.reg | 3 | regkey1i |

|  | Method |
|---|---|
| PATH=/usr/people/coedah/RESEARCH/TASK_I/LASER_DATA/POS_MOVED/MIKE_STAFNE | 1 |
| PATH=/usr/people/coedah/RESEARCH/TASK_I/LASER_DATA/POS_MOVED/JON_BLOTTER | 2 |
| PATH=/usr/people/coedah/RESEARCH/TASK_II/LASER_DATA/POS_MOVED/MAR19 | 3 |

### A.1.5 Commands

The commands in the preceding sections are listed below along with the location and default input/output files.

HOME=/usr/people/coedah

| Command | Location | Input Default | Output Default |
|---|---|---|---|
| ESDM | $HOME/SANDIA/GPIB/ADDA | N/A | N/A |
| scan6pt | $HOME/LSDM/source/Scan6pt | Scan6pt.default | ScanList.default |
| goscan | $HOME/RESEARCH/DEC97 | ScanList.default | vel.default |
| fourellipse.m | $HOME/RESEARCH/ELLIPSE | N/A | ScanList.default |
| goscan | $HOME/RESEARCH/DEC97 | ScanList.default | vel.default |
| ellipsereg.m | $HOME/RESEARCH/ELLIPSE | N/A | ABCDEF |
| tangenpts.m | $HOME/RESEARCH/ELLIPSE | ABCDEF | BITANGENT48PT |
| dac2reg.m | $HOME/MATLAB/FUNCTIONS | ometron2 | N/A |
| regkey1i | /disk2/matlab/toolbox/register | N/A | N/A |
| regkey1m | /disk2/matlab/toolbox/register | N/A | N/A |
| seven.m | $HOME/RESEARCH/TASK_II/ACOUSTIC_DATA/JAN22/pos1 | N/A | N/A |

## A.2 Velocity Reconstruction

The velocity reconstruction process consists of three steps: SLDV pose estimation, SLDV scanning, and velocity reconstruction. The SLDV pose process is described above. The SLDV scanning and velocity reconstruction procedures are described below.

### A.2.1 SLDV Structure Scanning

Velocity field reconstruction begins with scanning the vibrating structure. To generate a scanlist ( a list of left-right, up-down DAC pairs), the SLDV laser beam must be directed to the four corners which define the region of interest (ROI) and the DAC step values recorded in a file. Moving the SLDV laser beam is initiated with the command *ESDM*. A graphical user interface with two slider bars appears on the screen. The two slider bars are used to direct the laser beam toward each ROI corner. The DAC coordinates of the four corners are place in a file, ScanRect.default. The first line in the ScanRect.default file define the approximate number of rows and colums that the velocity image will have. The command *scanrect* reads this file and generates ScanList.default, a file which contains the DAC coordinate pairs to be scanned by the SLDV. This command also prints the actual number of rows and columns generated to the screen, record these numbers. The data acquisition software command *surf* reads the ScanList.default file and and acquires velocity image data. The *surf* command has a command line argument for defining the fitted excitation frequency. Thus, *surf* -F450 expects the structure excitation frequency to be 450Hz. Of course the SLDV pose process must be completed either before or after scanning the structure so that the position and orientation of the SLDV is known when the velocity image is acquired. Once SLDV velocity images and poses are avaliable, velocity reconstruction may begin.

### A.2.2 Velocity Reconstruction

The velocity field reconstruction procedure described in Chapter 5 is implemented with a Matlab m-file. For example, the Matlab command *plate-19mar-g* uses the contravariant method to reconstruct the velocity field over the finite element volume. The structure of the m-file is similar for each reconstruction method and is described by the psuedo-code below.

```
1. Set data file and function paths
2. Define reconstruction volume
   A. Define Nodes
   B. Define Connectivity (Element Definition)
3. Apply Transformation to nodes ( put volumn in correct position in space)
4. Calculate velocity sample points (object points)
   A. Define sample point parameters
   B. Evaluate basis functions at parameters
   C. Loop over all elements to define sample point coordinates
5. For each SLDV imaging position
   A. Load velocity file
   B. Load reference signal file
   C. Load scanlist file
   D. Process reference and velocity files to determine velocity image
   E. Load SLDV pose
   F. Apply SLDV pose transformation to object points
   G. Calculate mirror angles (image points) and virtual origins
   H. Calculate direction cosines
   I. Calculate interpolated velocity measurement values at image points
   F. Save sparse matrix containing interpolated velocity measurements
      an associated basis function values
6. Form least squares matrices from saved sparse matrices
7. Solve least squares problem
8. Calculate confidence bounds on regressed variable
```

The Matlab commands for velocity reconstruction in this dissertation are listed below.

| Command | Location | Note |
|---|---|---|
| plate_19mar_g | /usr/people/coedah/RESEARCH/JULY98 | Experiment 2, contravariant |

|  |  |  |
|---|---|---|
| `plate_cut_g` | `/usr/people/coedah/RESEARCH/JULY98` | `Experiment 1, contravariant` |
| `plate_19mar_cut` | `/usr/people/coedah/RESEARCH/PLATE` | `Experiment 2, partial L.S.` |
| `plate_cut` | `/usr/people/coedah/RESEARCH/PLATE` | `Experiment 1, partial L.S.` |
| `plat_19mar_xyz1` | `/usr/people/coedah/RESEARCH/PLATE` | `Experiment 2, full L.S.` |
| `plat_19mar_xyz1b` | `/usr/people/coedah/RESEARCH/PLATE` | `Experiment 1, full L.S.` |

The data files read by these m-files are located at

`/usr/people/coedah/RESEARCH/TASK_II/LASER_DATA/POS_MOVED/MAR1` and
`/usr/people/coedah/RESEARCH/TASK_II/LASER_DATA/POS_MOVED/MAR19`.

# Vita

I was born in Texas, the son of mechanical engineer, Frank S. Coe III, the grandson of a mechanical engineer, Frank S. Coe Jr.. This heritage provided an instinctive drive toward the mechanical engineering field. In my mid-teens, this drive was influenced by exposure to the qualitative science and research of J.W. Goethe and Rudolf Steiner. Specifically, an interest in projective geometry arose. My studies continued at the University of Texas at Austin where I earned a B.S.M.E and a B.A. German. I studied engineering to solve practical problems and German to read untranslated research. Following my university studies, I performed six years of military service, stationed in the Washington D.C. area. Lead by the beliefs, thoughts, and feelings of what my wife and I hold to be true, we choose to return to the academic environment to pursue my interest in projective geometry. This interest has guided the research from the beginning and finds a practical application in this research. I hope to continue these studies and develop further applications of projective geometry.

Permanent Address: Eggleston, Virginia

This dissertation was typeset with LaTeX $2_\varepsilon$[1] by the author.

---

[1] LaTeX $2_\varepsilon$ is an extension of LaTeX. LaTeX is a collection of macros for TeX. TeX is a trademark of the American Mathematical Society. The macros used in formatting this dissertation were written by Dinesh Das, Department of Computer Sciences, The University of Texas at Austin.